RICE UNIVERSITY

Development and Application of Methods to Study Nanoparticle Diffusion Using Intensity Correlation Spectroscopy

by

Alexei Tcherniak

A THESIS SUBMITTED
IN PARTIAL FULFILMENT OF THE
REQUIREMENTS FOR THE DEGREE

Doctor of Philosophy

APPROVED, THESIS COMMITTEE:

Stephan Link,
Assistant Professor of Chemistry and
Assistant Professor of Electrical and
Computer Engineering

R. Bruce Weisman,
Professor of Chemistry

Matteo Pasquali,
Professor of Chemical and Biomolecular
Engineering and Chemistry

HOUSTON, TEXAS

March 2011

ABSTRACT

Development and Application of Methods to Study Nanoparticle Diffusion Using Intensity Correlation Spectroscopy

by

Alexei Tcherniak

The practical application of nanoparticles requires transitioning from well controlled experimental settings to highly variable "real-life" conditions. Understanding the resulting changes in the behavior and stability of nanoparticles is therefore of paramount importance. This thesis discusses the development and practical applications of tools to monitor the behavior of nanoparticles in real-time using intensity correlation spectroscopy techniques. I show how correlation spectroscopy can be adapted to nanoparticle systems; and provide particular parameters and settings especially vital for heterogeneous systems. Oftentimes nanoparticles have to be labeled to be detected, which can complicate the system of study and can introduce systematic errors into the analysis. Intensity correlation spectroscopy was tested on dye-labeled magnetite nanocrystals. The fluorescence correlation spectroscopy results were surprisingly biased towards a low concentration of aggregates. Scattering and absorption cross-sections of gold nanoparticles are greatly enhanced near the plasmon resonance wavelength, providing strong intrinsic signals for directly visualizing nanoparticles. I show here how scattering and absorption scale with nanoparticle size; and how size heterogeneity within nanoparticle samples translates into the detected signals. One-photon luminescence of gold nanoparticles, an often neglected signal, was also considered. A comparison

between one-photon luminescence and scattering correlation spectroscopy revealed that the former has a much smaller bias towards aggregates and therefore is advantageous in systems prone to aggregation. Overall, the work presented here describes the tools and methods that were developed towards better understanding of nanoparticle behavior in a liquid medium where they are to be employed for environmental and biological applications.

ACKNOWLEDGEMENTS

I would like to thank my advisor, Professor Stephan Link, for his mentorship and support throughout the Ph.D. His guidance and leadership have been the corner stone for professional development.

I am privileged to have studied at Rice University and I would like to extend my gratitude to the school and the members of the staff who provide the backbone that keeps Rice standing and running and who always lent a hand in the times of need. Particularly, I would like to thank Yvonne Kambourelis of Applied Physics program, Rose Gray-Dye and Dr. Linda Hamaker of Chemistry department and Susan Cudnik of the Chemistry Stockroom.

The list of projects completed and papers published would have been many times shorter if it had not been for the wonderful, bright, and super helpful collaborators and lab mates. Particularly, Carmen Reznik, Liane Slaughter, David Solis, Sergio Dominguez-Medina and Saumyakanti Khatua, who shared the frustration of trying to make something work and the joy of accomplishments. Professor Christy Landes with her cut-to-the-chase reasoning has been an invaluable second advisor. Many thanks to Professor Anatoly Kolomeisky's for his professional and personal guidance.

Most importantly I am very thankful to my wife, Ekaterina Pronina, and my daughters without whom none of it would be possible or have any meaning; my family and friends whose continuous support gave me strength and encouragement: Natalia and Gregory Tcherniak, Irina and Lidia Pronina, Polina Nezvankina, Artur Yagudaev, Artur Izmaylov and Maria Kolesnikova, Yulia Ivanova, Olga Bochareva and Sergei Ermilov. I have said it to you before and I will say it here again: "Thank you!"

TABLE OF CONTENTS

LIST OF FIGURES

CHAPTER 1

INTRODUCTION

1.1 Motivation and background

From everyday products like sunscreens to novel biomedical procedures, nanoparticles (NPs) are quickly capturing the scene. As suggested by the name, a NP is a particle for which one of its dimensions is in the nanoscale: 1-100 nm.[3] At this size scale, the properties of materials are strongly influenced by shape and size, and can be very different from either the bulk or the individual atoms the particles consist of.[4] A most stunning visual example of the properties of NPs is the use of gold nanoparticles (AuNPs) for making stained glass that possesses the astonishing property of changing color depending on the illumination mode: transmission of light vs. reflection of light. A famous example, the Lycurgus Cup, created circa 4th century AD fascinated minds for ages. It was not until modern times that its properties were attributed to the minute concentrations of gold and silver NPs embedded in the glass;[5] the cup appears red due to absorption by the NPs and green due to scattering by the NPs when the cup is illuminated at different angles relative to the observer. As particles shrink to sizes comparable to the wavelengths of light, the resonances of the collective oscillations of electrons in AuNPs, known as plasmons, depend on the shape and size of the NP,[6] leading to highly tunable optical properties.[7-9]

Magnetite NPs, known as 'nanorust', provide a great example of how the functionality of the material scales sensitively with its size.[10] It is known that the surface of magnetite is a good adsorber of arsenic in contaminated water. The use of bulk

magnetite is not preferred for water decontamination, however, because of the large amounts of magnetite required and it needs to be utilized afterwards. Reducing particle sizes to the nanometer scale greatly increases the available surface area and thus greatly improves the effectiveness of purification. There is concern, however, with extracting the magnetite NPs from purified water after treatment. The NPs do not sediment out of solution on their own. Applying an external magnetic field has been found to remove the particles from solution, and the optimal field strength depends on the NP size.[10]

Currently, NPs are composed of a very broad range of materials: from inorganic quantum dots,[11] to DNA cages,[12] to gold nanostars.[13] They all share a common requirement: in order to utilize their unique properties, which are programmed by their tunable size and shape, NPs have to be soluble and environmentally safe in the media in which they are to be used. The particles should not unintentionally aggregate, precipitate, adsorb or be adsorbed, interfere with biological processes, etc.[14,15] To this end, NPs are produced with chemically designed coatings which enable selective interactions with their environment. A great deal of research is focused on developing these coatings so that the NPs themselves are protected and their properties are preserved.

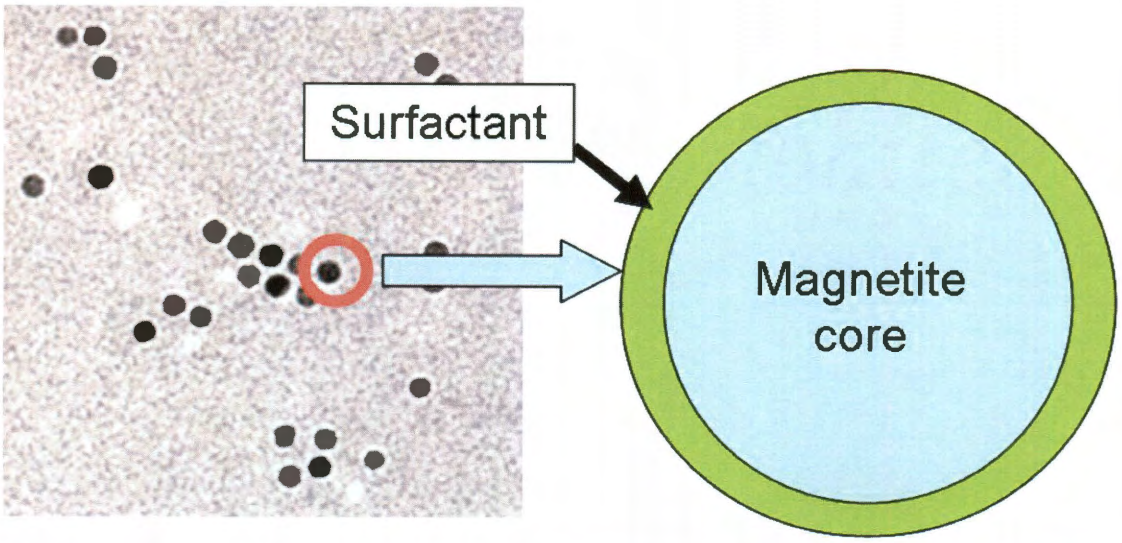

Figure 1.1 TEM image of magnetite NPs and a schematic representation of a single NP showing the core and a coating layer made of PEG, which is not visible in the TEM image.

Figure 1.1 shows that a NP can be described as a NP core with a coating material. The core can act as a functional part or as a scaffold or vector for delivering functional groups, useful for drug delivery, for example.[16] As suggested earlier, the coating serves to stabilize the NPs in suspension. It can also carry out certain functions, e.g. target recognition.[17,18] Depending on the purpose the coating serves, its chemistry can vary from a simple polymer, like PEG, to rather sophisticated mixtures of protective coatings, antigens and image contrast agents.[19]

Significant progress has been made towards developing effective coatings under carefully controlled experimental conditions.[16,20-22] In contrast, an important milestone yet to be fully achieved is ability to monitor dynamic behavior and changes occurring to NPs in the more unpredictable environments imposed by the media of their application. Namely changes to the coating of NPs and potential NP aggregation in these media are of most concern. For example, a highly anticipated photothermal cancer treatment is centered around plasmonic NPs that are positioned on the tissue to be destroyed.[23-25] The

tissue is then irradiated with light of specific frequency at energy levels that are harmless to human tissue. The NPs, however, are designed to have absorption cross-sections that are orders of magnitude higher than the surrounding tissue and they thus efficiently convert the incident radiation to heat. This heat is generated and dissipated only in the vicinity of the NPs, allowing high precision destruction of tissue. The challenge here as in many other proposed applications is to get NPs to their target inside the body. This can be done by designing the coating to make the NPs soluble and only bind to the target, thus leading to high NPs concentrations only near the target.[15,16,20-25] Because the coating is an essential part of the system, any changes to it in situ affect the efficiency of this treatment.

A different approach to targeted delivery is to design NPs that respond to an external field and use them to guide the NPs. Magnetite NPs already mentioned above can be guided by a low gradient magnetic field, which opens possibilities for targeted delivery.[26] How NPs respond to the external field, whether they aggregate and whether that aggregation is reversible is another topic of on-going research.[10,27,28] Similarly, other applications of NPs rely on surface coatings or changes to them to function as biological sensors,[29,30] delivery agents,[31,32] or catalysts.[33,34] What has been shown to work beautifully in well controlled laboratory conditions,[35] needs to be tested under realistic conditions where non-specific binding of matrix material can alter the carefully designed coating.[36]

Most of the traditional methods for NP characterization suffer setbacks when trying to work with changes occurring in real-time or with low concentrations of analyte. To observe a change, one first needs to visualize the characteristics that are being monitored. For example, optical properties of NPs are tied directly to their shape and size,

which makes UV-Vis characterization one of the most common and simplest methods of characterizing NP samples. Ensemble UV-Vis spectroscopy requires a relative high concentrations of NPs and a low background signal, or a constant background that can be later subtracted. There are recent reports on single particle spectra,[2,37-40] but they are limited to either NPs fixed at the surface[2,37-39] or produce spectra that are fluctuating in time due to NPs producing different spectra depending on the relative orientation of NP to the incoming light.[40] Indeed, the anisotropy of the NP shape and and how it affects the interaction with light at different angles in the resulting spectrum is by itself an important question.

Other common methods of characterization are SEM, TEM, and AFM imaging. These are the standard and best methods for the measurement of the core size. However, sample preparation involves drying, which inevitably alters information about the aggregation state of the NPs, affects their coatings,[41-43] and does not allow measurements in real-time. For example, the size of the coating is deduced from TEM imaging (see Figure 1.1A) as the distance between the cores of two neighboring particles in an aggregate. However, this may or may not be the actual thickness of the coating in the solution because the coating is affected by the solvent and presence of charged species, etc.[44-46] There have been modifications to these techniques, like cryo-TEM, aimed at solving those issues, but they still cannot be done in-situ or in real-time. Additionally, the organic coating gives a very low contrast. So those methods are not really applicable to detect changes to the coating of NPs.

Measuring the hydrodynamic radius of NPs is a good way to probe what is happening with the NPs. The hydrodynamic radius, also known as the Stokes-Einstein

radius, is defined as the radius of a sphere that has the same diffusion constant as the particle of interest, thus the sizes of the core and coating are included in the hydrodynamic radius. Because aggregation changes this radius, NP aggregates can be detected directly through monitoring the hydrodynamic radius. Changes in size may indicate loss of the protecting capping, or possible adsorption of additional layers that might inhibit the desired functionality. Also, because the viscosity of the medium affects the diffusion constant , changes to the recovered size can be related to changes in the NP environment[46].

A number of methods have been developed for particle sizing, e.g. dynamic light scattering (DLS), fluorescence correlation spectroscopy (FCS), small angle X-ray scattering (SAXS), single particle tracking, to name a few. Those methods offer opportunities to get information in real-time and each one them has strong and weak aspects as well as requirements determining the degree of difficulty with respect to sample preparation. The underlying principle for all of these methods is that random diffusion of particles generates intensity fluctuations, which can be tracked and converted to a diffusion constant. Selecting properties that provide the highest signal to background ratio is of outmost importance. In single particle tracking, as the name implies, each particle is tracked and information is extracted from the resulting trajectories. Although probably the simplest method in principle, experimental realization of it is often quite complicated because in order to acquire long enough trajectories the particles must not be allowed to move out of the observation volume. That involves employing 3D tracking equipment or confined sample chambers.[47,48] In contrast, it is possible to use methods that collect signal from a specific volume and use fluctuations in intensity from particles

diffusing in and out to calculate the diffusion constant. This collection volume can be relatively large – DLS, SAXS – or small – FCS – depending on the particular need. DLS and SAXS are well established methods for bulk characterization of NPs and work with relatively high concentrations (10^{-3}-10^{-6}M) and observation volumes (microliter and above). Intensity correlation spectroscopy, e.g. FCS, is ideal for low concentrations ($\sim 10^{-9}$ M) and offers high spatial resolution as the detection volume is on the order of femtoliters. The small detection volume also improves the signal to noise ratio, because the background signal is weaker from such a small volume.[49] High spatial resolution, together with a detection limit on the order of single NPs and high signal to noise, makes intensity correlation spectroscopy an ideal candidate for studying NPs in biological environments.

As was discussed previously, the ability to visualize the particles of interest and to separate them from the background is vital for performing intensity correlation spectroscopy. A very common way of visualization is labeling the particles with dyes.[50-52] In doing so one attains flexibility of tuning excitation and observation wavelength, but pays the price of introducing dye molecules into the coating of the particles, affecting the chemistry of the coating, as well as dealing with dye leaking out into the solution.[53-55] Additionally, the dye's photophysical processes, e.g. blinking or bleaching, may further complicate the analysis.[56-58] For those reasons, a stable intrinsic signal of a NP that can be used to visualize the NP directly attracts a lot of interest. While scattering and absorption are obvious choices as intrinsic signals, they require either suppressing background by using pure solutions or increasing signal by switching to plasmonic particles, which have large absorption and scattering cross-sections and will stand out from the background.[59,60]

Luminescence has also been utilized for example in studies of the diffusion of single-walled carbon nanotubes (SWCNTs),[48] semiconductor nanorods,[61] and gold nanorods. The latter have been visualized using two-photon excitation.[62-64] One-photon luminescence of AuNPs, although known for several decades[65,66], has been considered too weak to be used in intensity correlation spectroscopy.[67-71]

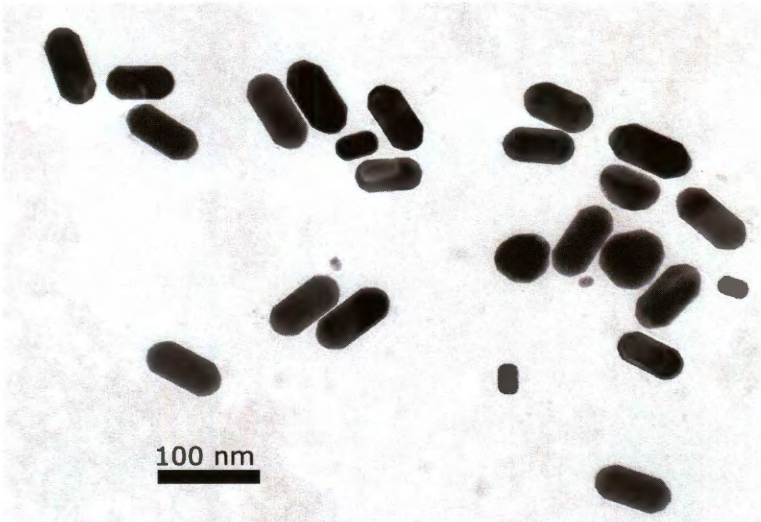

Figure 1.2. A representative TEM image of a gold nanorod sample. Clearly the sample contains particles of different sizes and aspect ratios.

As shown in Figure 1.2, NP samples are never perfectly homogeneous, and the effects of heterogeneity need to be accounted for in the analysis. Intensity correlation spectroscopy relies on intensity fluctuations arising from particles going in and out of the observation volume. It logically follows that brighter particles will create stronger fluctuations and therefore can dominate the analysis.[27,72] Furthermore, as mentioned earlier, the optical properties of plasmonic NPs are strongly dependent on the size and shape[2,73] and it is important to discuss the relationship between sample heterogeneity and signal heterogeneity.

The main theme of this work is the development of methods capable of monitoring the change of hydrodynamic radii in-situ and in real-time using intrinsic signals and accounting for potential size heterogeneity, with specific focus on how intensity correlation spectroscopy can be adapted for this purpose.

In this thesis, the diffusion of NPs is studied primarily with intensity correlation spectroscopy methods, which is a generic term encompassing fluorescence correlation spectroscopy (FCS), scattering correlation spectroscopy (SCS)[74], photothermal absorption correlation spectroscopy (PhACS)[75,76], etc., which all can be traced back to the same method developed by Elson and Magde in 1972 for dyes diffusing freely in solution.[77] Contrary to other fluorescence techniques, in FCS it is not the absolute amplitude of the signal that is of interest, but rather the changes, or fluctuations in the signal that provide information about the system. The first applications of FCS studied binding of small molecules with DNA.[78] In principle, any physicochemical process that affects fluorescence can be studied with FCS: concentration fluctuations, aggregation, photophysical processes like blinking or bleaching, chemical reactions, etc.[78,79] The method quickly gained in popularity resulting in about 50 publications over the next 5 years. However, the early applications of FCS were plagued by a low detection efficiency, high background, and hardware limitations. It was not until the early 1990s with the development of confocal FCS and availability of high quality detectors that sufficient signal to noise levels could be reached and the detection of truly single molecule dynamics was achieved.[49] Over the years, FCS has been adapted and modified, which significantly expanded upon the systems that can be studied. For example, modifying the detected signal to enable polarization correlation spectroscopy allowed the observation of

rotational dynamics of single molecules and particles.[80] Changing the excitation path led to the development of scattering,[74] photothermal,[75] and two-photon luminescence correlation spectroscopies.[62] Dual-beam[81] and dual-color[82] setups provide opportunities to study transport phenomena and interactions between molecules.

Translational and rotational diffusion of particles, their aggregation, photobleaching and other physicochemical processes occurring in the system of interest, some of which are depicted in Figure 1.3A, lead to the fluctuations of the signal in Figure 1.3B. In order to detect fluctuations of the signal, the number of particles in the observation volume has to be quite small, typically only a few at a time, and the background signal has to be kept to a minimum. These problems are alleviated by reducing the observation volume and concentration. By these means only a few particles occupy the detection volume at a time, and the background signal is collected from a small volume only. To achieve small focal volumes, laser light is focused into a tight spot. However tighter focusing alone can only do so much, because there is little control over the depth of the focal volume. A drastic reduction of the observation volume was first implemented by Rigler et al.[49] by installing a pinhole before the detector, creating confocal conditions and subsequently very small detection volumes.

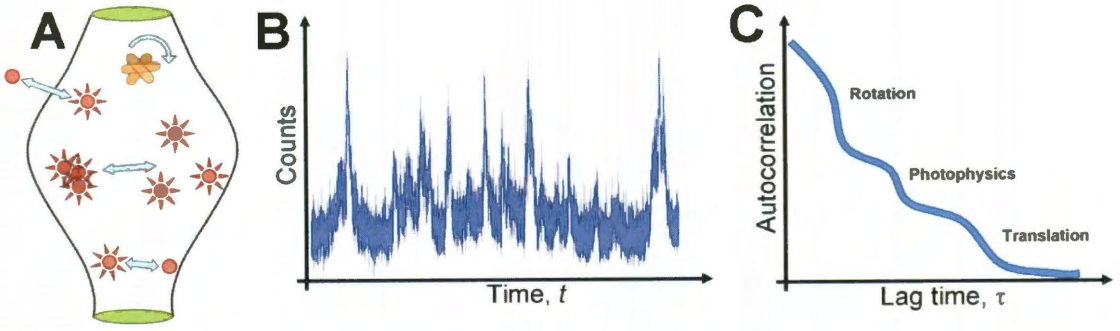

Figure 1.3 *A*: Schematic focal volume and some of the possible mechanisms causing intensity fluctuations: diffusion in and out, blinking, aggregation and rotation. *B*: Raw time transient collected from a solution of diffusing dye molecules. *C*: Autocorrelation curve showing different processes giving rise to intensity fluctuations.

Despite the best effort of reducing the background, certain components, e.g. shot-noise, are inherently present. Therefore, the signal can be obscured by very noisy time transients, such as the one in Figure 1.3B. In order to deal with very fast intensity fluctuations, one can use an autocorrelation function. Autocorrelation from fast random noise decays very quickly, thus leaving only the true signal at longer times. In Figure 1.3C a schematic autocorrelation function is shown for a dye undergoing translational and rotational diffusion as well as photoblinking. For single molecule dyes, rotational dynamics occur on the nanosecond time scale, photophysical processes occur on a microsecond time scale, and the time it takes on average to traverse the focal volume is in the hundreds of microseconds range. As a result, these processes are well separated within the autocorrelation function, which allows them to be evaluated independently. Of course, particular characteristic timescales are highly dependent on the sample and in the case of rotational and translational dynamics, are dependent on the size of the particles.

1.2 Specific aims

To effectively and safely use NPs for bio-medical applications, the questions that require attention are: 1) the fate of the capping material after photothermal treatment, which determines the solubility of the NPs and for the large part toxicity; 2) the actual size of the NPs in the medium, which is the core size plus the capping material; and 3) the state of aggregation of the NPs under physiological conditions. All of these questions can be probed by measuring the hydrodynamic radii of the NPs in real-time. The goal of this work is to adapt intensity correlation spectroscopy to study the diffusion of NPs, and to serve as a tool for answering these critical questions.

Specific aim 1

To understand the limitations and parameters for successfully applying FCS to NP systems and to determine the criteria for analysis and observe the effects of the presence of multiple species in FCS.

Specific aim 2

To apply FCS to a well-characterized and controlled NP system with low heterogeneity to experimentally prove that FCS can be scaled from a single molecule to a single NP, where the size of the NPs are no longer negligible compared to the size of the focal volume, and to concurrently develop tools for reducing the effect of sample heterogeneity on the outcome of FCS measurements.

Specific aim 3

To investigate the size dependence of the intrinsic signal from AuNPs, namely absorption and scattering, and to help in alleviating issues with labeling of NPs and provide correlation of size heterogeneity and signal heterogeneity. To investigate other

possible sources of signal heterogeneity for a NP sample, for example, anisotropy of the signal.

Specific aim 4

To identify other possible intrinsic signals for AuNPs. To study real AuNP samples, which have not been specially prepared, labeled, or purified, and to determine their sizes in solution. To apply the methodology to other shapes, for example, gold nanorods (AuNRs).

1.3 Overview

This thesis contains chapters that are based on publications relevant to the research topic. Chapter 2 presents work on determining the experimental conditions for FCS studies of heterogeneous systems. Specifically, it describes the requirements for the lengths of the transient that is being autocorrelated, a topic that has not been addressed previously, and the important implications of that to studies of heterogeneous systems. The work was published in *Analytical Chemistry* in 2009.[83]

In Chapter 3, FCS is applied to study diffusion of magnetite NPs. The sample that appears very homogeneous by traditional TEM characterization yields wildly varying hydrodynamic radii using FCS. The discussion for possible reasons follows and the effect of NP aggregation is addressed. A burst intensity frequency analysis technique is described and the findings in relation to separating artifacts in FCS analysis for systems with a small percentage of aggregates are discussed. The work was published the *Journal of Physical Chemistry C* in 2009.[27]

Chapter 4 focuses on the characterization of intrinsic signals – scattering and absorption – from gold NPs as a function of NPs size. Mie theory predictions are confirmed at the single particle level for the first time. Explanations for the large deviations of the signal from similarly sized particles are given based on the particle/light interaction at different relative orientations. Important conclusions about signal heterogeneity of "real-life" AuNP samples are provided. The work was published in *Nano Letters* in 2010.[2]

In Chapter 5, the conclusions from the previous work are put to work to study translational and rotational dynamics of AuNPs and AuNRs. One-photon luminescence from AuNPs and AuNRs is proposed as a possible intrinsic signal and its advantages are shown. The thickness of the capping material in solution is estimated using correlation spectroscopy. Additionally, the intriguing nature of one-photon luminescence is probed by single particle spectroscopy and a mechanism is proposed. It is shown that, quite surprisingly, interband transitions are not the only source of one-photon luminescence.

CHAPTER 2

FLUORESCENCE CORRELATION SPECTROSCOPY: CRITERIA FOR ANALYSIS IN COMPLEX SYSTEMS[1]

2.1 Abstract

This work is aimed at evaluating the effect of varying parameters for Fluorescence Correlation Spectroscopy (FCS) analysis, first in the context of a one species/one environment system, and then in a complex system composed of two species, or conversely, two environments. Experimentally appropriate settings are established for the maximum lag time and averaging times over which an autocorrelation is carried out, as a function of expected diffusion decay time for a particular solute. It is shown that use of appropriate settings plays a critical role in recovering accurate and reliable decay times and resulting diffusion constants. Both experimental and simulated data were used to show that for a complex binary system, in order to extract accurate diffusion constants for both species, decay times must be bounded by adequate minimum and maximum lag times as dictated by the fast and slow diffusing species respectively. It is also demonstrated that even when constraints on experimental conditions do not permit achieving the necessary lag time limits for both of the species in a binary system, the accuracy of the recovered diffusion constant for the one species whose autocorrelation function is fully time resolved is unaffected by uncertainty in fitting introduced by the presence of the second species.

---

[1] This chapter is based on the manuscript titled "Fluorescence Correlation Spectroscopy: Criteria for Analysis in Complex Systems" by Alexei Tcherniak, Carmen Reznik, Stephan Link, Christy F. Landes, published in Analytical Chemistry 81, 746-754 (2009). The first two authors contributed to the work equally.

2.2 Introduction

Measuring dynamics in a heterogeneous system is an increasingly important application for Fluorescence Correlation Spectroscopy (FCS). This is witnessed by the use of FCS to probe diffusion conditions in a variety of complex biological media, including diffusion in the presence of crowded biological environments,[84,85] at membrane interfaces,[86-88] and within confined cellular structures.[89] In addition to the many biological applications of FCS, the technique has also been used to characterize a number of complex non-biological systems, for example: to profile flow characteristics in microchannel structures,[90,91] to evaluate diffusion in bulk and thin films,[92-95] and to characterize nanoparticle diffusion.[27,96-98]

Extracting an accurate description of the multiple dynamic processes occurring in these complex systems from an FCS experiment is not trivial. This is because the FCS experimental autocorrelation curve can be convoluted by a number of different optical and experimental conditions.[49,57,99,100] In addition, for a complex system, not only do relative diffusion rates contribute to the autocorrelation function, often over a wide range of time scales, but relative concentration and brightness of species obscure the fitting by contributing additional fitting parameters.[101] To further complicate matters, although an experiment may theoretically be probing a simple system, i.e. one diffusing species in a homogeneous environment, this system may actually be convoluted by the presence of a second species (bright aggregates of the fluorescent entity, for example).[27]

In spite of the challenges, FCS is an attractive method for monitoring the dynamics of diffusion and diffusion mediated processes because the method is selective for fluorescence, and can be applied to a wide range of physical systems in situ, at low volumes, and at low concentrations.[101,102] There exists an extensive body of literature covering FCS theory,[79,80] ideal optical parameters,[49,100] and appropriate experimental conditions.[57,99] Successful implementation of FCS requires attention to each of these areas. And finally, accurate analysis of an experimental FCS autocorrelation decay curve requires attention to several key parameters set within the autocorrelation function itself.[103-105]

We have found that this is particularly true with respect to analysis of complex systems. Even for a single species diffusing in a homogeneous environment, the autocorrelation function is dramatically affected by minimum and maximum lag-time limitations, with direct effects on the accuracy of the recovered diffusion coefficient.[105,106] Considering complex systems, the development of an accurate treatment of multi-species fits with an eye on defining appropriate autocorrelation lag time regions and autocorrelation averaging times is needed.[105,106]

In this work, we present systematic guidelines by which to define appropriate FCS analysis parameters for a complex system composed of multiple diffusing species, or multiple diffusion environments. The behavior of recovered diffusion constants as a function of particle size or solute viscosity was monitored as minimum and maximum lag times were varied for a single species solution,[105-107] and we show that as a rule, minimum lag times need to be 2/3 or less the value of the shortest characteristic diffusion time for a experimental system, and maximum lag times must be on the order of 5,000

times the longest characteristic diffusion time, before observed diffusion constants converge to expected values. Additionally, we show that in the single molecule regime it is necessary to establish that the combination of chosen concentration and averaging time for each experimental system is sufficient to recover an accurate diffusion constant. Each of these parameters is then evaluated for a complex experimental system composed of multiple diffusing species. We also utilize a 3D random walk simulation to complement the experimental data in building a clear picture for the behavior of recovered diffusion constants for complex systems. Using these two techniques, we demonstrate that the minimum and maximum lag time limits defined above can be applied to systems exhibiting complex autocorrelation functions. Moreover, we fully evaluate the effect on ability to recover accurate diffusion constants for two diffusing species in the case when an autocorrelation function is not fully time resolved for the second species. We establish for the first time that the accuracy of the recovered diffusion constant for the first, fully time-resolved, species is unaffected by the behavior of the autocorrelation function in the lag time region exhibiting decay due to the second species. This is true in spite of the uncertainty in fitting that arises in this lag time domain.

2.3 Experimental

2.3.1 Method

The observable in an FCS experiment is the fluctuation in fluorescence intensity measured within a focused laser volume. Autocorrelation analysis of temporal fluorescence fluctuations is carried out as in Equation 2.1, and the resulting function

represents the degree of self-similarity of the measured fluctuations in the signal, $\delta F(t)$, over a set of lag times, τ, ranging from τ_{min} to τ_{max}. Here, τ_{min} is the minimum lag time and τ_{max} is the maximum lag time for which signal correlations are evaluated:[101]

Equation 2.1

$$G(\tau) = \frac{\langle \delta F(t) \cdot \delta F(t+\tau) \rangle}{\langle F(t) \rangle^2}$$

In this expression, $\langle F(t) \rangle$ is the average of the fluorescence signal over time, and $\delta F(t)$ is the signal at time t, minus the average:

Equation 2.2

$$\delta F(t) = F(t) - \langle F(t) \rangle = F(t) - \frac{1}{T}\int_0^T F(t)dt$$

Here T denotes the total time of the transient. Depending on the assumptions about the system and the questions to be answered, fluctuations can be defined as arising from a particle diffusing in and out of the focal volume, $W(\vec{r})$, i.e. concentration fluctuations, $\delta C(\vec{r},t)$; or changes of the absorption cross-section, $\delta\sigma$; or quantum yield, δq; etc.

Equation 2.3

$$\delta F(t) \sim \int_V W(\vec{r}) \cdot \delta(\sigma \cdot q \cdot C(\vec{r},t))$$

W is often referred to as the "focal volume", although in reality it is a convolution of the excitation and detection volumes and for the most part can be approximated as

Equation 2.4

$$W(\vec{r}) = e^{-2\frac{x^2+y^2}{r_0^2}} \cdot e^{-2\frac{z^2}{z_0^2}}$$

Where r_0 and z_0 are the lateral and axial dimensions at which the 3D Gaussian has decayed to $1/e^2$.

Autocorrelation function decays as lag time, τ, increases and the decay is governed by the probability of observing two photons separated by time τ. For a single species undergoing purely translational diffusion, the characteristic diffusion time, τ_D, which is the time it takes on average to traverse the focal volume due to Brownian motion alone, is given by

Equation 2.5

$$\tau_D = \frac{r_0^2}{4D}$$

And the autocorrelation function then takes the following form:

Equation 2.6

$$G(\tau) = \frac{1}{V_{eff}\langle C\rangle}\frac{1}{\left(1+\frac{\tau}{\tau_D}\right)}\frac{1}{\sqrt{1+\left(\frac{r_0}{z_0}\right)^2\frac{\tau}{\tau_D}}}$$

For most of the experimental conditions, because the axial dimension, z_0, of the focal volume is much bigger than the lateral dimension, r_0, the characteristic diffusion time, τ_D, becomes effectively two-dimensional and depends only on the lateral dimensions of the focal volume.

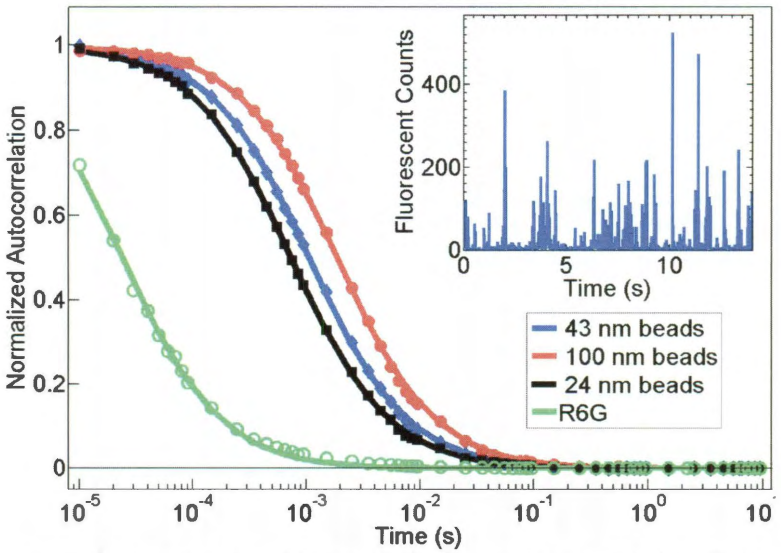

Figure 2.1. Autocorrelation curves for 100 nm (red), 43 nm (blue) and 24 nm (black) polystyrene beads as well as single R6G molecules (green) diffusing in water. Symbols and solid lines are the actual data and the fit with Equation 2.6. Inset: A fluorescence transient binned up to 10 ms for a 100 nm beads sample. Each blip corresponds to a bead going through the focal volume.

Some experimental autocorrelation curves are shown in Figure 2.1. By fitting the experimentally obtained autocorrelation curves with Equation 2.6, τ_D and the diffusion coefficient can be obtained. Using the Stokes-Einstein relationship we then are able to relate diffusion of a solute to solvent viscosity, η, and solute hydrodynamic radius, R_h:

Equation 2.7

$$D = \frac{k \cdot T}{6\pi \cdot \eta \cdot R_h}$$

2.3.2 Simulations

Diffusion was modeled via random walk simulations in 3 dimensions.[103,104,108,109] At each step, the particle position was moved a random and uncorrelated distance along each of the x, y and z-axes. The magnitude of the step in each direction was selected from a uniformly distributed range defined using the Matlab R2006 built-in random number generator, that extended over ± a maximum specific step size. The simulated

sample volume consisted of a rectangular box, extended along the z-axis, with periodic boundary conditions. A 3D Gaussian intensity profile was used to model the focal volume of the laser, with a ratio, r_0/z_0, of 0.1, to approximate the experimental conditions (see Figure 2.6).

For two species simulations, two kinds of particles were defined by establishing a different maximum step length value within the uniform step-length distribution. At the beginning of each simulation, 10 particles were randomly distributed throughout the sample volume. For all data reported in this work, the focal volume r_0 value was set to 250 nm, and maximum step lengths were 25 nm and 79 nm for the slow and fast diffusing particles, respectively. These step lengths were chosen because of the clear visual effects apparent in the autocorrelation function as parameters are varied. Additional simulations conducted over a variety of step length values confirm the same effects on autocorrelation function fitting throughout the lag time regions covered (data not shown).

Simulated fluorescence from each particle was computed as the value of the Gaussian intensity profile at the position of the particle:

Equation 2.8

$$F(x,y,z) = a \cdot \exp(-\frac{2(x^2+y^2)}{r_0^2}) \cdot \exp(-\frac{2z^2}{z_0^2})$$

where $r_0 = 2\sigma_1$ (2 times the standard deviation of the Gaussian in the xy-plane), and $z_0 = 2\sigma_2$ (2 times the standard deviation of the Gaussian along the z-axis). The overall fluorescence signal trajectory as a function of step was computed as the sum of individual particle fluorescence values at each step of the simulation. These fluorescence signals are created assuming no photophysics and 100% fluorescence quantum yield. To better

approximate the experimentally observed conditions, random noise was added to the random walk fluorescence transient.

Simulated trajectories were run for 10^6 steps, yielding the equivalent of a 10 second trace. Ten trajectories were collected to allow adequate averaging of the autocorrelation functions calculated over these 10 second traces, yielding a 100 s sampling time. We verified that the fit quality of the autocorrelation function averaged over 100 seconds was sufficient by comparing the quality of the fit to curves constructed from over 100 averaged trajectories, or 1000 seconds. The fit quality was equivalent. We can thus confirm that for sample volume dimensions of 6 times the $1/e^2$ intensity radius of the Gaussian signal, and for 10 particles, averaging over 10 trajectories was sufficient for the autocorrelation function to converge to a constant value that was well-fit by the standard autocorrelation expression (Equation 2.6) . We observed that for too small sample volume dimensions and too few particles, the autocorrelation fitting at large lag times showed a faster decay region that could not be well fit[109]. Having the complete fluorescence transient from the simulation, subsequent autocorrelation analysis was carried out in the same manner as described for the experimental data in the following sections.

2.3.3 Materials and setup

Carboxylate modified polystyrene beads (orange fluorescent, max abs/em: 540/560 nm, Invitrogen), and Rhodamine-6G (max abs/em: 530/566 nm, Invitrogen) were used as standards for these FCS studies.

All dilutions were made in MB grade water (Hyclone, VWR). Coverslips (no. 1 borosilicate 22x22 mm, VWR) were washed in MB grade water, dried, and then plasma cleaned with oxygen. Sample chambers of either self-adhering pliable silicone (2 mm depth, Grace Bioloabs), or mylar spacers (75 μm depth, McMaster-Carr) with a central cavity were placed on the coverslips. Sample solutions containing fluorescent probes were placed within the central cavity and a clean coverslip was placed over the filled chamber in such a manner that no bubbles were trapped inside the chamber.

The experimental set-up is based on a homebuilt confocal, epiflourescence microscope. Excitation of the sample was achieved with 532 nm laser light (VERDI, Coherent). Laser light was circularly polarized and expanded with a Keplerian beam expander to overfill the back aperture of a 1.3 NA oil immersion 100x microscope objective (Carl Zeiss, GmBH). Spatial filtering of imperfections of the laser light was achieved by passing the light through either a fiber optic cable prior to expansion, or through a pin hole (10 μm) at the focus point within the Keplerian beam expander. Light was attenuated using appropriate neutral density filters to a power density at the sample of between 1 and 1200 W/cm^2, depending on the fluorescent probe. The $1/e^2$ focal volume radius and ½ height for our experimental system were ~230 nm and ~2 μm, respectively, yielding a focal volume of approximately 0.3 fL.

Sample fluorescence was collected by the objective and separated from excitation light via a dichroic mirror (z532rdc, Chroma Technology) and a notch filter (NHPF-532.0, Kaiser). The fluorescence signal was passed through a 50 μm pin hole at the microscope image plane, refocused, and sent to an avalanche photon detector (SPCM-AQR-15, Perkin Elmer). The signal from the photon detector was passed to a photon counting

board (PMS-400-A, Boston Electronics Corporation), which produced single photon counting trajectories which were used for autocorrelation analysis.

2.3.4 Data fitting

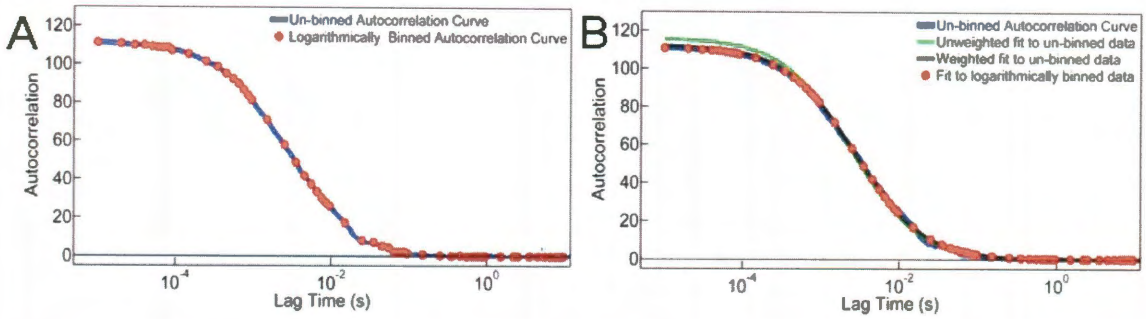

Figure 2.2. (A) Raw experimental autocorrelation data (blue line) and after logarithmic binning (red points). (B) Fits of Equation 2.6 to both sets of data: unweighted fit to the un-binned data (green), weighted fit to the un-binned data (black), and unweighted fit to the logarithmically binned data (red points). In the unweighted fit to the un-binned data, the fit is heavily influenced by the plethora of points at large lag times, which are not as relevant to the decay of the autocorrelation function as the points at smaller lag times, resulting in a poor quality fit.

Autocorrelation curves and fits for 100 nm polystyrene beads are shown in Figure 2.2A. Because of the logarithmic scale, the density of points along the graph increases exponentially towards larger lag times. Because we are interested in the decay of the autocorrelation function, the most relevant points are those where the autocorrelation function exhibits changes (small lag times in Figure 2.2) and not where it is practically constant (large lag times). Fitting the autocorrelation data as is with Equation 2.6 (green line in Figure 2.2B) is heavily influenced by points at large lag times and fails to correctly capture the autocorrelation function. To remove the bias, it is possible during fitting to give bigger weights to points at smaller lag times, resulting in a much better fit (black line). Fitting logarithmically binned data returns the fit that is practically identical to the weighted one (red points). Returned diffusion times were: 2.40 ms for un-binned

and un-weighted data; 2.68 ms for un-binned and weighted data; and 2.74 ms for binned and un-weighted data. Throughout this work, autocorrelation data is first logarithmically binned and then fitted, to balance the contributions to the fit from different parts of the decay.

2.4 Results and discussion

It was found that three key autocorrelation analysis parameters have a dramatic effect on the form of the final autocorrelation function. These three parameters are: 1) the minimum autocorrelation lag time, τ_{min}, 2) the maximum autocorrelation lag time, τ_{max}, and 3), the autocorrelation averaging time, t_{avg}. The following discussion is focused on the maximum autocorrelation lag time and the autocorrelation averaging time. For details on the minimum autocorrelation lag time, I would refer the reader to the published work in *Analytical Chemistry* in 2009.[83]

Autocorrelation for FCS analysis can be performed using either hardware autocorrelator boards or by performing software autocorrelation analysis directly on fluorescence signal trajectories collected with a photon counting board. A real advantage of onboard hardware autocorrelation is that the hardware configuration itself and the use of a multi-tau data acquisition algorithm[103] combine to allow real-time collection of the autocorrelation function with significantly reduced data processing time. However, software autocorrelation performed directly on fluorescence signal trajectories as in Equation 2.1 allows for extensive data manipulation and provides the ability to make comparisons over the same exact data set. Therefore we have used software autocorrelation throughout this work. Note that several algorithms using multi-tau

schemes, in which an autocorrelation function is evaluated at a specific set of lag times rather than all possible lag times, have been developed for use within software autocorrelation as well,[110,111] and these greatly reduce data processing requirements. However we carry out the autocorrelation calculation over all possible lag times to avoid introducing additional analysis variables to our autocorrelation function shape and fitting that may arise from shifting lag time distributions. All analysis programs were written in Matlab (R2006a). Comparisons made by Gell *et al.* for autocorrelation analyses done by both software and hardware methods have demonstrated comparable performance in determining diffusion coefficients.[105]

All data were acquired at a minimum photon binning time of 10 μs. As reported in other studies,[112-114] the concentration regime was adjusted so that no more than one molecule was in the focal volume at a time. Signal trajectories were typically collected over a period of 5 minutes or more. Signal trajectories collected this way could be modified after acquisition using Matlab programs to bin photon counts further (for example, to 100 μs bins and up), and to concatenate successive trajectory files so that varied length trajectories for autocorrelation analysis could be formed. Using these software tools, maximum lag times and averaging times were adjusted as noted in the following sections.

The autocorrelation functions were carried out on signal trajectories using Equation 2.1, and then multiple autocorrelation functions were averaged together to bring the total experiment time to five minutes, except where noted. The final averaged autocorrelation function was then subjected to a logarithmic binning algorithm, which averages all values within successive logarithmically defined decades. This means that

the final autocorrelation curve is composed of individual points that are logarithmically spaced. The final curve resembles an autocorrelation curve obtained using a multi-tau algorithm, however all lag times contribute to the curve. The primary effect of this binning algorithm is to equalize the relative data weights across the logarithmic decades for the subsequent fitting. Curves binned in this way correspond closely to the raw autocorrelation curves. Comparison of fitting done for raw autocorrelation data weighted with standard deviations,[103] and fitting for the logarithmically binned data closely correspond, with returned diffusion times showing less than 3% difference for standards. In comparing fitting for the weighted raw autocorrelation data and non-weighted raw data, we see 10% difference. Comparison of primary fits of the logarithmically binned data and weighted fits of logarithmically binned data for fully resolved autocorrelation curves show less than 2% difference in recovered diffusion times. For the data presented herein, all fitting was done post logarithmic binning via nonlinear least squares, using the Levenberg-Marquardt algorithm with data weighting as described by Wohland, *et al.*[103]

2.4.1 Single Species. Maximum Lag time (τ_{max})

The explicit expression for calculating an experimental autocorrelation function is a discrete time equation given by:[107]

Equation 2.9

$$G(m) = N \cdot \frac{\sum_{i=1}^{N-m-1} (F(i) - \overline{F}) \cdot (F(i+m) - \overline{F})}{\left(\sum_{i=1}^{N-m-1} F(i) \right)^2}$$

In comparing this with Equation 2.1, m is the discrete time equivalent of τ, and represents the time (or lag) between two points in a signal for which the autocorrelation is evaluated. The *maximum autocorrelation lag time*, then, is *N-1* in the above equation, which is the maximum time offset that the variable m can take. For all practical purposes, at large values of N, N-1 ~ N. Thus, for any signal trajectory, the largest possible value for τ_{max} is the length of the fluorescence trajectory.

Because of its non-invasive nature and specificity, FCS is increasingly used to probe complex systems like bio-membranes. A review of the literature shows numerous examples in which very slow diffusion processes are revealed in the autocorrelation functions for these kinds of systems.[115-117] While many diffusion processes traditionally probed by FCS occur with time scales in the range of microseconds to tens of milliseconds, slower processes can show diffusion times on the order of hundreds of milliseconds to seconds. These longer diffusion time scales approach the values of τ_{max} commonly used in FCS experiments, which are often on the order of 1 to 10 seconds.

While τ_{max} values of 1 to 10 seconds are ample for the traditional range of diffusion times probed, we have found that as diffusion processes become longer, these limited values for τ_{max} introduce artifacts into the autocorrelation function and have a dramatic effect on recovered translational diffusion times in single species experimental data. To evaluate the effect of limited τ_{max} values on recovered diffusion times, we iteratively adjusted the value of τ_{max} and ran the resulting autocorrelation evaluations over the same fluorescence trajectories. In Figure 2.3 the percent deviation of the value of the diffusion constant with respect to the final value is plotted as τ_{max} is varied. It can be seen that decreased τ_{max} values affect values for the recovered diffusion constant as τ_{max} begins

to approach the value of the autocorrelation decay time. The data in Figure 2.3A also show that larger species, with longer decay times, require longer τ_{max} times before retrieved diffusion constant values begin to converge. In part B of Figure 2.3, we see the behavior of the autocorrelation curves for 43 nm beads as τ_{max} is reduced. Note the migration of the autocorrelation curve to faster diffusion times with reduced τ_{max}, and particularly, note the development of a significant negative dip in the tail of the autocorrelation function, along with developing negative residuals for the single species fitting.

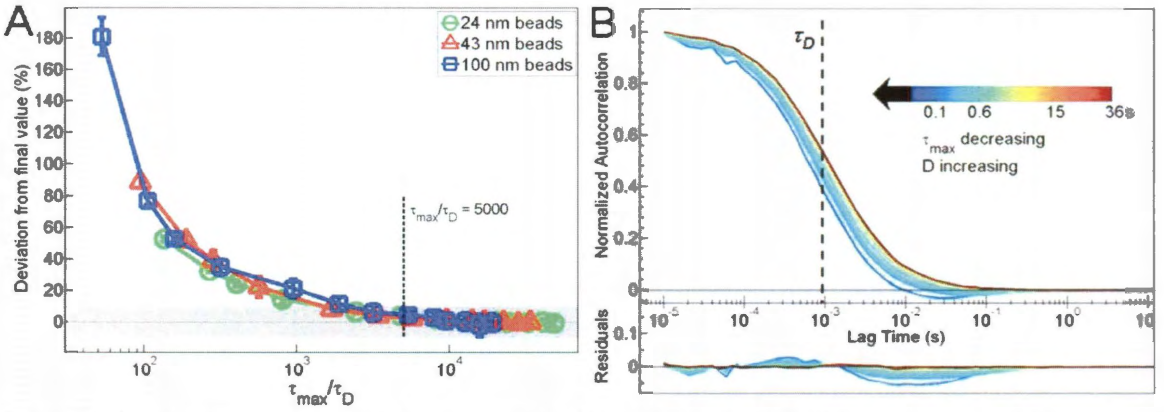

Figure 2.3. (A) Dependence of the recovered diffusion constant on the maximum lag time. When τ_{max} is normalized by τ_D, the dependence of the recovered diffusion constant on τ_{max} becomes virtually the same for different sizes. Thus a single criterion can be chosen for all particle sizes: $\tau_{max} \geq 5000\ \tau_D$. The grey bar region in the graph marks the 10% deviation boundaries. (B) Sample autocorrelation curves for 43 nm beads, analyzed for various τ_{max} times, with single species fit residuals. The characteristic decay time is shown by the vertical line. As τ_{max} approaches τ_D (0.98 ms), the autocorrelation curves migrate to faster times and a negative region appears in the tail of the curve.

The origin of this behavior stems from the fact that the true autocorrelation function of the fluorescent signal due to diffusion of particles through the focal volume is given by the covariance expression:[106]

Equation 2.10

$$G(\tau) = E[F(t) \cdot F(t+\tau)]$$

where E is the expectation value for each value of τ. For diffusion, as for other ergodic processes, expectation values can be replaced by a time average in the limit of infinitely large times.[78]

Equation 2.11

$$G(\tau) = \lim_{T\to\infty} \frac{1}{T} \int_0^T F(t) \cdot F(t+\tau) dt$$

Note that in FCS, fluctuations of the intensity are often used in place of the actual intensity, and $G(\tau)$ is normalized by the square of the mean fluorescent intensity, as was shown in Equation 2.1.

Experimentally, the integral in the equation above cannot be computed, and the discrete time expression shown in Equation 2.9 with a limited number of time lags is used instead, as an estimator of the true function. Inspecting the numerator of Equation 2.9, it becomes clear that at higher lag times, or values of m, the equation has fewer and fewer terms contributing to the sum at $G(m)$, and this results in underestimation of the autocorrelation expression for these higher lag times. Lu *et al.* have reported changes in recovered decay times as a function of τ_{max} from simulated rotational diffusion experiments.[107] Based on analytical evaluation of the autocorrelation function, their recommendation was that τ_{max} of at least 1000 times larger than the decay time would minimize the artifacts arising from underestimation of the autocorrelation function. This is because large values of τ_{max} localize the underestimation bias in regions of the autocorrelation curve where the lag time has already decayed to zero, regions that are well beyond the expected decay times for diffusion processes. In the case of stationary single molecule rotational diffusion experiments, in which photon trajectories are obtained from a single molecule,[118-120] trajectories are short due to the eventual

photobleaching of the molecules. Because of this, τ_{max} times are limited by the experimental conditions.

In translational diffusion experiments, however, trajectories are not collected from the fluorescence of one individual molecule monitored over a long time, but are collected instead from the fluorescence traces arising from different molecules rapidly traversing the focal volume. At appropriate laser powers, photobleaching is not a problem, and this means that trajectories can usually be collected over much longer times allowing much larger values of τ_{max} for the system in question. It should be noted that simply increasing measurement times and averaging over additional autocorrelation curves (see the next section for a discussion of averaging), will not improve the behavior of the autocorrelation function if τ_{max} is not also made sufficiently long.

The data in Figure 2.3B demonstrate experimentally that as τ_{max} approaches the decay time of the curve (shown by the vertical line), the underestimation has a dramatic effect on the position and variance of the measured autocorrelation curve. In evaluating the effect on the autocorrelation curve for our three different diffusers, we found that for accurate experimental evaluation of translational diffusion, τ_{max} should be at least 5,000 times larger then the expected decay time (see Figure 2.3A) in order to remove the effects of discretization of the autocorrelation function. For instance, for the 43 nm polystyrene beads shown in Figure 2.3B, with a characteristic decay time of 0.98 ms, this would correspond to a τ_{max} of 4.9 seconds.

2.4.2 Single Species. Concentration and Averaging Time (t_{avg}).

FCS is able to resolve signal fluctuations from single molecules diffusing through the focal volume, and concentrations of fluorescent solutes are often adjusted so that on

average fewer than one molecule is in the focal volume at a time. However, the autocorrelation analysis relies on averaging over the behavior of many individual molecular encounters with the focal volume. The total number of these encounters is a function of both the concentration of the given solution, and the length of time over which the focal volume is observed. To build up the necessary statistics so that the calculated autocorrelation function represents the true mean behavior of translational diffusion through the focal volume, the autocorrelation function, $G(\tau)$ for a given maximum lag time is typically averaged over numerous measurements taken over an extended measurement time.

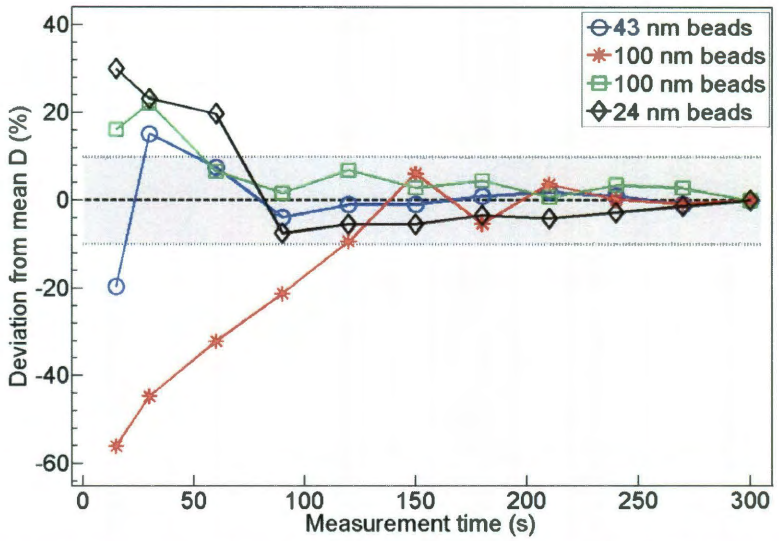

Figure 2.4. Convergence of the value of the diffusion coefficient as a function of averaging time. The grey bar region marks the 10% deviation boundaries.

In Figure 2.4 we demonstrate how the diffusion constant converges to a final value for an experimental system, as averaging time, t_{avg}, is increased for each of the three sizes of polystyrene beads used in this study. Note that two examples of the deviation in recovered diffusion constants for 100 nm beads for different t_{avg} are shown

(calculated on two separate runs, with the same concentration solution), to demonstrate the variation that results from insufficient t_{avg} times. For the concentrations used, averaging for 150 seconds or longer brings retrieved values of the diffusion constant within 8% of the converged value, which is within our experimental error. In carrying out analysis for any system, it is necessary to verify that t_{avg} is sufficient for the sample diffusion constants and concentrations in questions. To determine the lower limit of t_{avg} required for a given sample and analysis scheme, a set of autocorrelation functions can be collected over a series of averaging times, until the autocorrelation function is observed to stabilize and the standard deviation of recovered diffusion constants from the sets is satisfactory (generally < 10% for FCS experiments). Note that excitation light intensity at the source is an additional variable to consider, because detection of focal volume encounters can decrease significantly at low intensity light levels.

2.4.3 Two Species. Experimental.

For complex experimental system, we used FCS to monitor the diffusion behavior of a mixture of 24 nm and 100 nm polystyrene beads. The relative fluorescence brightness of polystyrene beads scales as r^3, and for these two sizes there is a ~ 70 times difference in brightness (FluoSpheres Fluorescent Microsphere Product Information, Molecular Probes, Paisley, PA). In this system therefore, we have species dependent brightness in addition to species dependent diffusion constants. For a complex system such as this, the measured autocorrelation function is a combination of contributing diffusing species:[101]

Equation 2.12

$$G(\tau) = \frac{\sum \eta_i^2 \langle C_i \rangle^2 G_i(\tau)}{\left(\sum \eta_i \langle C_i \rangle\right)^2}$$

where η_i is brightness and C_i is the concentration of species i.

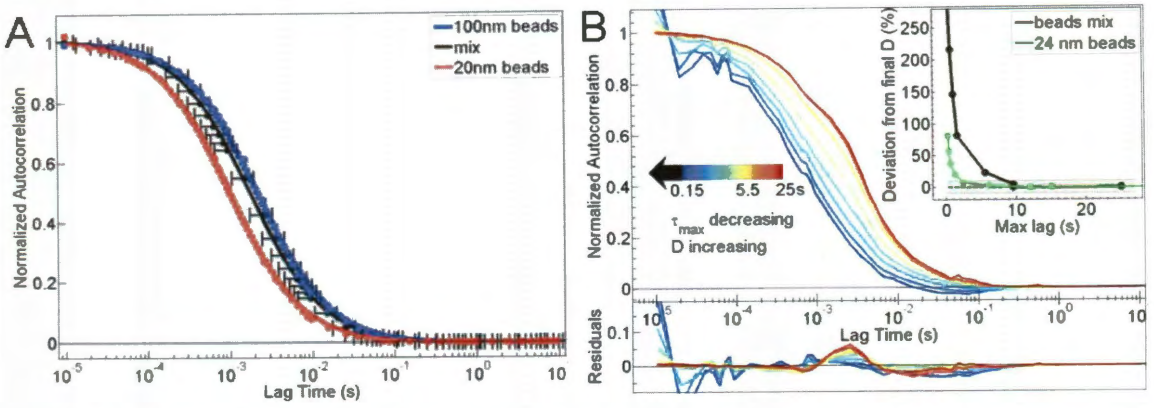

Figure 2.5. (A) Variation in retrieved autocorrelation curves for 24 nm and 100 nm beads, and a mixture of the two at a 1:0.006 ratio of 24 nm: 100 nm beads. (B) Change of the autocorrelation curve for a mixture of 24 nm and 100 nm beads, as a function of varied τ_{max}. Lag times are varied from 0.2 s to 30 s.

Because brightness weights the autocorrelation curve so heavily, we have found that at about a 5% ratio of 100 nm to 24 nm beads, the diffusion of 24 nm beads can no longer be resolved from the autocorrelation curves. Thus, we chose a mixture with a concentration ratio of ~0.6% 100 nm beads to 24 nm beads. Shown in Figure 2.5A are autocorrelation functions averaged over 5 minute analysis windows for 24 nm beads, 100 nm beads, and the mixture of beads. Although for both concentrations of beads we verified that t_{avg} (5 minutes in this case) is sufficient when running these species independently, the error bars in Figure 2.5A for the mixture extend far beyond the <10% region associated with single species samples and show that in the mixture 5 minute

averaging is no longer sufficient. Note that the error bars for the single species samples are not graphed because they coincide with the data points of their respective curves at the visual resolution of the graph. This greater than expected fluctuation from run to run appears to be an indicator of the presence of a complex system.

Figure 2.5B shows the behavior of the autocorrelation curve for the mixture of beads as τ_{max} is varied. We again see the change of the autocorrelation curve, and that a negative autocorrelation region in the tail of the curve develops as τ_{max} decreases. The effect of the presence of the very small concentration of large, bright particles on the τ_{max} dependence curve is seen in the inset of Figure 2.5B. Although the mixture is composed of 99.4% 24 nm beads, the dependence of a recovered single species diffusion constant on τ_{max} looks nothing like the pure 24 nm bead sample. This data shows that even a very small percentage of highly fluorescent species (in our case, 100 nm beads) can dominate the data and if not accounted for, lead to wrong estimations of sizes present in the sample.

We have noticed both experimentally and in simulations that 2 species fits that are based on Equation 2.12 for a brightness convoluted system often compensate for brightness by changing the individual transient times when all parameters (two species, including brightness) must be fit. Therefore in the context of an experiment where both the diffusion coefficients and the relative brightness of individual species are unknown and must be fit, a two species fit needs to be evaluated carefully. For our experimental system we found that the effect of brightness on the fitting leads to inconsistent recovered diffusion constants for both a single and two species fit. It should be noted that even when a system is believed to be simple, i.e. composed of only a single species, a great deal of care must be taken to assure that this is actually the case.[27]

2.4.4 Two Species. Simulations.

Simulations of random walk processes have been established as an excellent model for real world diffusion processes.[103,104,108,109] Therefore, as a means to clarify the effects that the three parameters, τ_{min}, τ_{max} and t_{avg}, have on the recovered diffusion constants for a complex system, we have examined a complex simulated system composed of two diffusing species, but with the simplification that these species have the same relative brightness. By removing brightness as a fitted parameter in the simulated experiment, we are able to perform a consistent two species fit by which to evaluate the effects on the retrieved diffusion constants caused by varying these parameters.

In Figure 2.6A we show a representation of a small region of the simulated sample volume described previously, centered on the focal volume. The first 100 steps of a two species simulation are shown. Note that for visual representation, we have increased the particle number in the figure in comparison to the simulation conditions in which 10 particles total were placed in the sample volume. The diffusion constant for the particles shown in lighter gray is 10 times larger than that for the darker particles. The focal volume of the laser is depicted in the center of the Figure 2.6A (variation in color are due to graphical visualization and carries no information). The autocorrelation curves for the individual species as well as a 50/50 mix of the two are shown in Figure 2.6B. The subset of Figure 2.6B shows the residuals for both single and two species fits for the mixture.

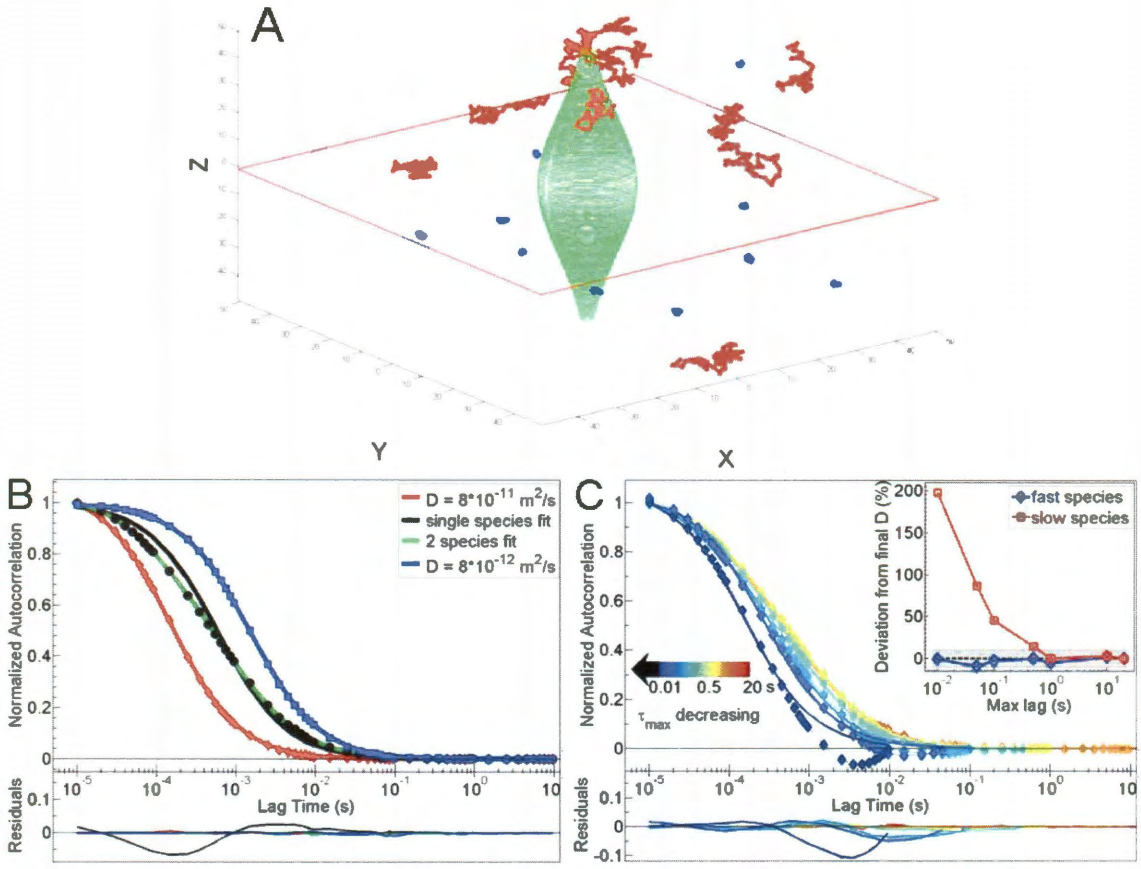

Figure 2.6. (A) A sub region of the simulation diffusion volume, centered on the focal volume, with two species: large lighter walks are due to a fast diffuser, small darker walks (spots) are due to a slow diffuser. The diffusion constants are 10 times different in magnitude. The sample volume maximum radius is 250 nm. Only the first 100 simulation steps are shown. (B) Autocorrelation curves for each of the single species, and for a run with both slow (blue, maximum step size of 25 nm), and fast (red, maximum step size of 79 nm) species combined (black points). The recovered diffusion constants are shown. The green line is a two species fit of the data, and the solid black line is a one species fit. (C) Behavior of the two species autocorrelation curves (normalized to the fitted amplitude) as a function of τ_{max}, with deviation of the recovered diffusion constant from the expected value shown in the inset. The recovered diffusion constant for the slower species is affected dramatically, while the faster species shows no dependence on these changes in τ_{max}.

In Figure 2.6C we see that as τ_{max} is varied, the autocorrelation curve for the simulated mixture behaves in the same way as the two species experimental data. As τ_{max} is reduced, a negative dip in the autocorrelation curve starts to appear, the autocorrelation curve visibly shifts toward faster diffusion, and it appears as if the faster species is dominating. The residuals are from the two species fit and clearly demonstrate the effect.

The inset suggests that reducing τ_{max} dramatically affects the values retrieved for the slower diffuser, without significantly affecting those of the faster species, again, as long as the appropriate limits are met for the faster species (τ_{max} limits in this case).

From this data we can draw an additional conclusion, that the appearance of a negative region in the tail of the autocorrelation function for what appears to be a simple system with one diffusing species and what is estimated to be an adequate τ_{max}, can be evidence for the presence of a slower diffusion process in a more complex mixture, perhaps from aggregates or localized high viscosity regions.

2.5 Conclusions

The ability to reliably retrieve accurate diffusion times critically depends on the parameters chosen for autocorrelation analysis. Through experiments with well controlled fluorescent polystyrene bead samples it was shown that as themaximum lag time, τ_{max}, is decreased and begins to approach the characteristic decay time, the autocorrelation curve shifts toward faster times and a significant negative dip develops in the curve. As a function of particle size, it was found that to retrieve accurate values for experimental diffusion constants, τ_{max} needs to be at least 5,000 times the expected decay time.

Additionally, it was demonstrated that the autocorrelation averaging time must not be overlooked, as under-averaging the autocorrelation function returns unreliable diffusion coefficients. For the range of working solute concentrations within any experiment, evaluation of retrieved diffusion constants versus averaging times should be conducted to assure that accurate and consistent diffusion constants are retrieved for the selected averaging time, concentration, and excitation light intensity.

Both experimental and simulated data were used to show that for a complex binary system, in order to extract accurate diffusion constants of both species, the maximum lag times and averaging times must be set with respect to the slower diffusing species. Furthermore, in a system with a complex autocorrelation curve, if one of two decay times is not fully resolved within the curve, the diffusion constant retrieved from two species fitting can still provide a good estimate for the faster species as long as the autocorrelation parameters defined above are sufficient for that species. For an unknown system, the presence of additional slow diffusion processes can be discerned from the presence of a negative region near the tail of the autocorrelation decay function.

2.6 Acknowledgement

I would like to acknowledge Dr. Carmen Reznik and Dr. Christy Landes with whom I collaborated on this project. This work was supported by the Nanoscale Science and Engineering Initiative of the National Science Foundation under NSF Award Number EEC-0647452.

CHAPTER 3
FLUORESCENCE CORRELATION SPECTROSCOPY OF MAGNETITE NANOCRYSTAL DIFFUSION[2]

3.1 Abstract

We have measured the hydrodynamic radii of magnetite nanocrystals (NCs) with an 11 nm core by fluorescence correlation spectroscopy (FCS). We found that the sizes determined from particle diffusion varied by as much as an order of magnitude for the same magnetite NC sample due to the presence of a small number of larger and brighter aggregates, which bias the fluorescence autocorrelation. By analyzing the fluorescence intensity distributions and applying a magnetic field we were able to gain insight into the size distribution of the magnetite NCs and estimate the percentage of larger aggregates present. Size-selective separation of aggregates larger than about 60 nm in diameter was achieved by applying a magnetic field of 0.24 T.

3.2 Introduction

Magnetic separation techniques are often superior to filter based purification methods because the magnetic particles can be extracted from the solution with a high degree of selectivity by applying an external magnetic field. Due to their large surface-to-volume ratio, magnetic nanocrystals (NCs) are actively explored for many biological applications ranging from ultrasensitive protein detection,[121] protein purification,[122] magnetic field guided drug-delivery,[26] single cell magnetic resonance imaging,[123] to separation of tagged cells.[124] In addition, selective binding of heavy metals to the surface

[2] This chapter is based on the manuscript titled "Fluorescence Correlation Spectroscopy of Magnetite Nanocrystal Diffusion" by Alexei Tcherniak, Arjun Prakash, J. T. Mayo, Vicki L. Colvin and Stephan Link, published in *Journal of Physical Chemistry C* **2009**, 113, pp 844-848

of magnetite NCs followed by magnetic separation makes it possible to inexpensively purify water contaminated with arsenic[10] and uranium.[125]

The efficiency of magnetic separators strongly depends on the particle size and applied magnetic field.[10,126] Colvin and coworkers have shown that magnetite NCs with diameters between 4 and 30 nm can be separated at low magnetic field gradients.[10] While the mechanism for the magnetic separation in high magnetic field gradients has been extensively studied,[126-129] the low field gradient separation of NCs is complicated by Brownian motion, which competes with the magnetic force for particles with diameters below 20 nm.[28,128,130,131] In order to understand the magnetic separation process and to optimize NC-based magnetic separators, it is crucial to directly follow the motion of different size magnetic NCs in the presence of an applied magnetic field.

Here we explore the application of fluorescence correlation spectroscopy (FCS)[78] to the measurement of single magnetite NCs moving freely in water and in the presence of an applied magnetic field. FCS offers a background free detection of fluorescent particles diffusing in femtoliter observation volumes with a time resolution in the sub-microsecond range. While FCS has been widely used to study the diffusion of individual molecules,[102,132,133] only a few reports on FCS of nanoparticles exist.[61,96-98] We were able to measure the diffusion constant and hydrodynamic radius of 9 nm magnetite NCs labeled with dyes in their surface coatings. A major challenge for this application of FCS is that larger and brighter particles and aggregates, even present in small amounts, can skew the measurement if conventional methods are applied. We therefore implemented a single molecule burst intensity frequency analysis (BIFA) to assess the magnetite NC size distribution. Analyzing the fluorescence intensity distribution in combination with FCS

has proven to be a useful tool in determining the diffusion of several species in a multi-component solution. Time-integrated fluorescence cumulant analysis (TIFCA),[134] photon counting histogram (PCH) analysis,[135] and fluorescence-intensity distribution analysis (FIDA)[136,137] make it possible to resolve 2-3 different species even if their sizes are of comparable magnitude.[134,138] Because for a large and unknown number of species (e.g. colloidal nanoparticles) a quantitative analysis becomes difficult due to the increase in fitting parameters and is essentially limited by the signal/noise ratio,[135,139] we show here how BIFA in combination with an applied magnetic field can be used to estimate the percentage of larger particles and aggregates present in solution.

3.3 Experimental

3.3.1 Synthesis of magnetite nanocrystals

Magnetite nanocrystals (NCs) were synthesized by pyrolysis of iron carboxylate salts as described previously.[140] The size of the magnetite nanoparticles was determined by TEM (JEOL 2010) to be 10.8 ± 0.55 nm. Fluorescent labeling of the magnetite NCs in aqueous solutions was achieved using the following procedure. 5 ml of 800 nM magnetite NCs in hexane was added to 15 ml of 10% IGEPAL CO-630 (Polyoxyethylene(9)nonylphenyl ether, Sigma-Aldrich) solution in water. The mixture was stirred overnight and centrifuged at 3,300 rpm for 2 hours (Beckman Coulter Optima L-80XP). The organic and the aqueous phases were separated and the aqueous suspension was filtered using a 200 nm syringe filter (NYLON-Whitman). The filtered suspension was ultra-centrifuged at 30,000 rpm for 2 hours to separate the excess IGEPAL CO-630. The particle settlement was re-dispersed in water, and 5μL of dye

(PKH 26, Sigma-Aldrich) was added, followed by overnight stirring and ultra-centrifugation (30,000 rpm for 2 hours) to remove excess dye. A dye coverage of approximately 165 dye molecules per NC was estimated using UV-vis absorption (Cary-5000 UV-Vis-NIR, VARIAN) and inductively coupled plasma atomic emission spectroscopy (Perkin Elmer ICP-Optimal Emission Spectrophotometer).

3.3.2 FCS sample preparation

In order to work in the single molecule regime, the dye-labeled magnetite NC samples were diluted to a final concentration of about 10^{-10} M using Millipore water. Fluorescent 43 and 100 nm FluoSpheres polystyrene beads with absorption/emission maxima of 540/560 nm were purchased from Invitrogen and diluted to a concentration of 10^{-10} M. The FCS sample chamber was constructed from two 25x25 mm coverslips (Corning) separated by a 75 μm self-adhering mylar spacer (McMaster-Carr). The coverslips were plasma cleaned for 30 seconds using oxygen in a PDC-32G Harrick Plasma Cleaner (Harrick Plasma). The mylar spacer was cut into squares of 25x25 mm with a hole in the center to hold about 7-10 μL of sample solution. A magnetic field was applied by placing a neodymium block magnet (K&J Magnetics Inc.) with a surface field of 0.24 T directly on the top coverslip. The effective distance between the magnet surface and the confocal excitation volume is estimated to be 250 μm. For salt-induced aggregation measurements, excess of biologically clean NaCl (Fisher Scientific) was added to the magnetite NC solution.

3.3.3 FCS setup

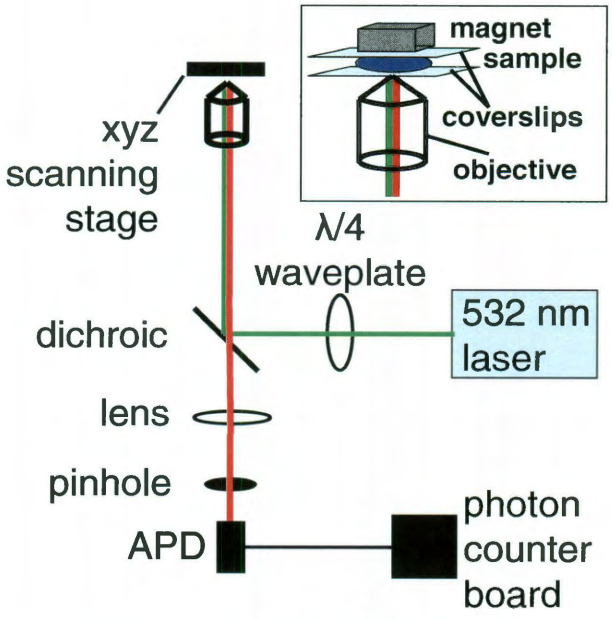

Figure 3.1. Schematic representation of the home-built experimental setup.

The homebuilt FCS instrument consisted of an inverted Zeiss Axiovert 200 microscope with a 100X oil immersion objective (Fluar, Zeiss). A schematic representation of the experimental setup is shown in Figure 3.1. A 532 nm solid state laser (Verdi, Coherent) was used for excitation with powers ranging from 100 W/cm^2 to 4 kW/cm^2. The fluorescence was collected using the same objective, imaged onto a 50 μm pinhole and separated from the laser light using notch and long-pass filters. After the pinhole, the light was refocused onto an avalanche photodiode (SPCM-AQR-15, Perkin Elmer), and the signal was recorded by a single photon counting board (PMS-400A, Becker&Hickl).

3.3.4 FCS analysis

As was discussed in Chapter 2, for a single diffusing species, the analytical solution, which has been derived for the normalized autocorrelation function, is given by:[78,102]

Equation 3.1

$$G(\tau) = \frac{1}{V_{eff}\langle C\rangle}\frac{1}{\left(1+\frac{\tau}{\tau_D}\right)}\frac{1}{\sqrt{1+\left(\frac{r_0}{z_0}\right)^2\frac{\tau}{\tau_D}}}$$

τ is the lag time, $< C >$ is the local number concentration of fluorescent particles, and τ_D is the residence time that particles spent on average in the excitation volume. V_{eff} is the excitation volume of the laser beam, which can be approximated as a 3D Gaussian with r_0 and z_0 as the radial and axial dimensions, respectively. The residence time τ_D is related to the diffusion coefficient D according to:[78,102]

Equation 3.2

$$\tau_D = \frac{r_0^2}{4D}$$

The hydrodynamic radius R_h can be calculated from the diffusion constant D using[78,102]

Equation 3.3

$$D = \frac{k \cdot T}{6\pi \cdot \eta \cdot R_h},$$

where η is the solvent viscosity, k is the Boltzmann constant, and T is the temperature. A fit of the experimental autocorrelation curve using Equation 3.1 yields τ_D, which is then

used to calculate the diffusion constant D with Equation 3.2 and the hydrodynamic radius R_h with Equation 3.3.

3.3.5 Experimental FCS procedure

The instrument was aligned before each measurement series by optimizing the detector and pinhole positions. As an alignment standard, 100 nm dye-labeled polystyrene beads drop-casted on a coverslip were imaged using a closed-loop xyz piezo-controlled stage (P-517.3CL, Physik Instrumente) and a SPM 1000 surface probe controller (RHK Technologies). The focal volume parameters were obtained using a water solution of 100 nm beads. r_0 was determined to be 200 nm with an error of about 5%, which results in an error for the diffusion constant of roughly 10%. The half-height of the focal volume (z_0) was constrained to 2 μm.[49] In order to minimize errors due to focus drift, we performed all measurements at a focus position of 1 μm inside the sample, which was adjusted through the z-axis movement of the piezo-controlled scanning stage.

The autocorrelation analysis was performed by software autocorrelation using programs written in Matlab (R2006a). Fitting was performed with Matlab's built-in Trust-Region algorithm. The bin width of the photon counterboard was set to 10 μs resulting in fluorescent transients with a total length of 0.6 seconds, which was dictated by the finite number of points accessible with our counterboard. Because the diffusion time extracted from the autocorrelation function depends both on the minimum bin width and the length of the autocorrelation trace, we determined the best bin time to be 10 μs with an autocorrelation length of 15 seconds. To achieve the required autocorrelation length, we concatenated 25 files together before computing the autocorrelation function.

There is 60 ms dead time in between the files that is required to write the data on the hard drive (communication with Becker&Hickl). However, we verified that for the systems studied here the dead time does not have an effect on the recovered diffusion constants.

To estimate how well Equation 3.1 fits the data we used a method proposed by Wohland et al.,[1] where data from several autocorrelation curves is used to compute the standard deviation of each point according to:

Equation 3.4

$$\sigma(\tau) = \sqrt{\frac{1}{L-1}\sum_{l=1}^{L}\left(\frac{G_l(\tau)}{G_l(0)} - \frac{1}{L}\sum_{l=1}^{L}\frac{G_l(\tau)}{G_l(0)}\right)^2}$$

L is the total number of autocorrelation curves acquired during the measurement, typically 40-60 curves. The inverse of the standard deviation was used as the weights for fitting the data and computing the residuals.

A burst intensity frequency analysis (BIFA) was carried out in order to identify events in the fluorescent transient originating from single particles diffusing through the excitation volume. With a bin time of 10 μs and typical counts rates of < 1 MHz individual events are not distinguishable from the detector dark counts in the fluorescence transient. However after binning the signal into 10 ms time intervals, individual fluorescence bursts appear in the transient. In order to automatically find the intensity bursts, we developed a Matlab algorithm that first calculates the background and then deletes all points below a threshold value set equal to the background plus 5 times its standard deviation. The cutoff value was adjusted so that a transient from a blank solvent did not produce any events. All fluorescence intensities above the threshold value were assigned to individual bursts and histogrammed.

3.3.6 Dependence of the diffusion constant on measurement time and focus position

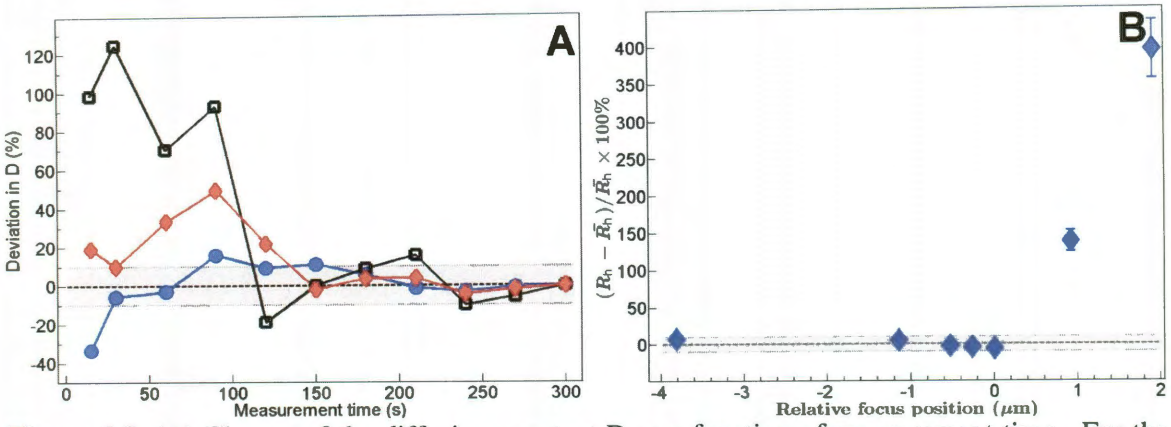

Figure 3.2. (A) Change of the diffusion constant D as a function of measurement time. For the measurement time dependence, the three curves correspond to two magnetite NC samples (black and red) and one 100 nm bead sample (blue). For better comparison despite the different particle sizes, all three curves are plotted as a deviation from the diffusion constant measured at 300 seconds. (B) Change of the hydrodynamic radius as a function of focus position. The focus position dependence was measured for 100 nm dye beads, where 0 μm corresponds to the laser beam focused at the coverslip interface and negative values to a focus inside the sample cell.

We also verified that the distribution in recovered hydrodynamic radii does not originate from an insufficient number of fluorescence fluctuations for each FCS measurement. Figure 3.2A shows the deviation of the calculated diffusion constant from the value obtained after 300 seconds as a function of FCS measurement time for 3 different samples. The gray rectangle denotes the region of uncertainty related to an experimental error of 10 % for the diffusion constant. A negative (positive) deviation corresponds to a smaller (larger) diffusion constant compared to the value measured at 300 s. For short acquisition times, the deviation is large. However, after only about 150 - 200 seconds of continuous data acquisition for samples with a concentration of about 10^{-11} M, the value of the diffusion constant does not significantly change within the experimental uncertainty. All FCS measurements reported here were therefore recorded for at least 300 seconds. For FCS measurements with an applied magnetic field,

autocorrelations were recorded in 300 second measurement increments for a total acquisition time of 10 minutes each while allowing an additional 10 minutes in between applying and removing the magnet.

A hindered diffusion of the magnetite NCs due to an attractive interaction with the coverslip surface, which could be responsible for the larger than expected hydrodynamic radii, was minimized by performing all experiments at a focus position of 1 μm inside the sample chamber. In order to verify that the recovered hydrodynamic radii are independent of the focus position inside the sample, we recorded a series of FCS autocorrelations of 100 nm polystyrene dye beads with varying focus positions. The results are summarized in Figure 3.2B, which shows that the measured diffusion constant is independent of focus position as long as the focus is at the coverslip interface or inside the sample chamber. When the focus is below the sample (positive focus position in Figure 3.2B), the measured fluorescent transient is no longer dominated by free diffusion but by particles interacting with the coverslip interface resulting in unrealistic values for the recovered diffusion constant and hydrodynamic radius. In addition, the same approximations for the geometry of the focal volume no longer apply. Therefore, in order to ensure that the focus did not drift below the sample from the typically used focus position of 1 μm inside the sample, we monitored the focus using a second dichroic beamsplitter and CCD camera placed outside the microscope during the acquisition of the fluorescent transients.

3.3.7 Concentration dependence of FCS and BIFA

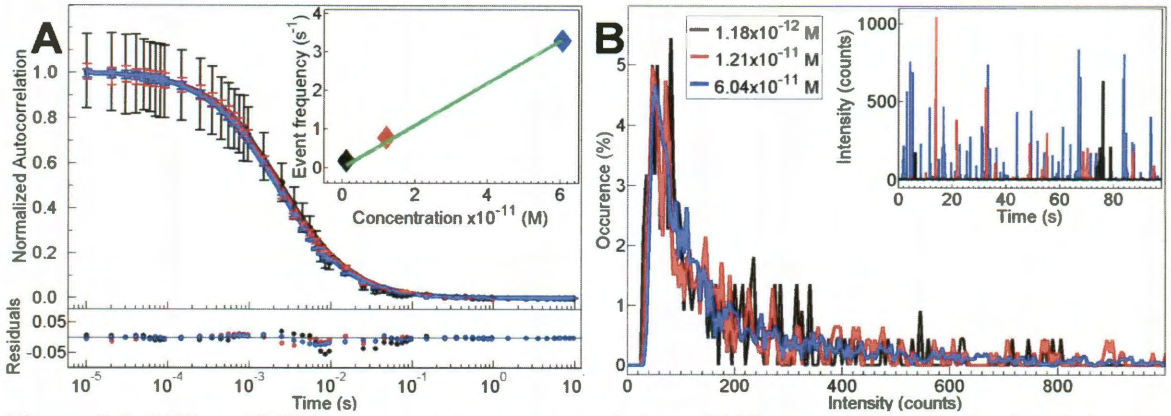

Figure 3.3. FCS and BIFA on a model system consisting of 100 nm polystyrene dye beads in water. The autocorrelation (A) and intensity histogram (B) is independent of concentration, while the number of events increases with increasing concentration (inset in A). The inset in B shows typical fluorescence trajectories for the 100 nm beads after binning the fluorescence counts into 10 ms time intervals.

We tested the applicability of a burst intensity frequency analysis (BIFA) on a model system consisting of nearly monodisperse 100 nm polystyrene dye beads. BIFA works by binning the fluorescence counts initially recorded every 10 μs into longer time intervals of 10 ms, which generates fluorescence trajectories showing individual intensity bursts from single particles (see inset in Figure 3.3B). Using an automated event-finding algorithm, the binned fluorescent transients are analyzed for the burst frequency and intensity. For three 100 nm polystyrene bead samples with concentrations of $6.0*10^{-11}$, $1.2*10^{-11}$, and $1.2*10^{-12}$ M, the normalized fluorescence autocorrelations curves and burst intensity histograms are indistinguishable as illustrated in Figure 3.3A and Figure 3.3B, respectively, while the number of bursts increases with increasing concentration (inset in Figure 3.3A).

3.4 Results and discussion

It is possible to obtain an autocorrelation of the fluorescence fluctuations caused by the diffusion of the dye-labeled NCs through the focused laser beam, as shown in Figure 3.4. The hydrodynamic radius of the dye-labeled magnetite NCs is estimated to be 7.5 to 9.5 nm, which includes an 11 nm NC core and a 1 to 2 nm thick surfactant shell. For the diffusion of magnetite NCs in water (Figure 3.4), we measured a diffusion constant of $3.0*10^{-11}$ m^2/s and a hydrodynamic radius of 8 nm in excellent agreement with the estimated size.

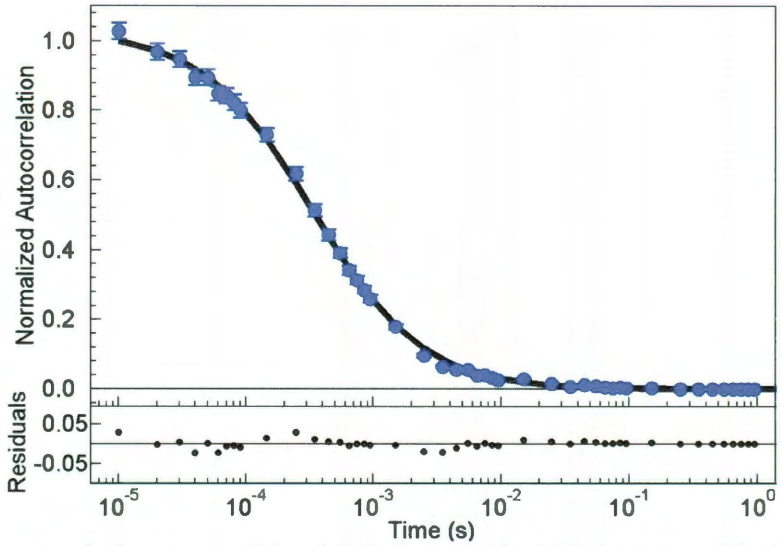

Figure 3.4. Autocorrelation curve of dye-labeled magnetite NCs in water. The black line is a fit to the data using Equation 3.1, which yields a diffusion constant of 3.0*10-11 m2/s and a hydrodynamic radius of 8 nm. Individual error bars for each data point were computed according to Wohland et al.[1] Residuals for the weighted fit are plotted in the bottom part of the figure.

In attempts to test reproducibility, however, we observed that the autocorrelation curves, and thus the calculated diffusion constants and hydrodynamic radii of the dye-labeled magnetite NCs, varied by more than an order of magnitude despite the narrow size distribution of the magnetite NC core of 10.8 ± 0.55 nm measured by TEM. The measured size varied greatly even for different measurements of the same sample. This

is illustrated in Figure 3.5, which shows three normalized autocorrelations of the same NC sample measured during three consecutive 5 minute acquisitions. The recovered diffusion constants of $2.2*10^{-11}$, $1.1*10^{-11}$ and $7.6*10^{-12}$ m^2/s for these three measurements are well outside our experimental error bar of 10%. The inset in Figure 3.5 summarizes the results for 57 measurements of 12 different magnetite NC samples.

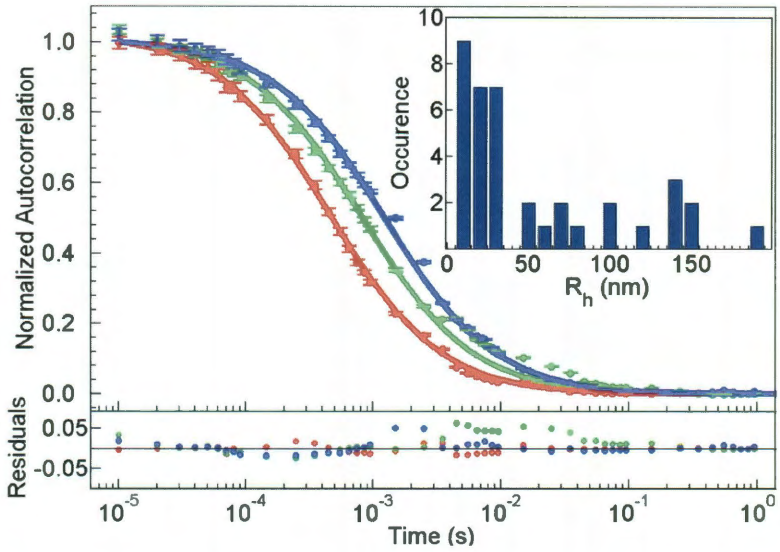

Figure 3.5. Three consecutive FCS measurements of the same magnetite NC sample. The recovered hydrodynamic radii Rh for the red, green, and blue autocorrelation curves are 11, 22, and 32 nm, respectively. The lines correspond to fits using Equation 3.1. The inset shows the distribution of Rh for all FCS measurements.

It is known that a number of experimental factors influence FCS measurements, including varying coverslip thicknesses, fluorescence fluctuations of dye molecules due to their intrinsic photophysical properties, optical saturation of the detectors, etc.[57,100] We therefore have taken measures to assure accuracy in the instrument calibration and have determined an error of less than 10% for recovered diffusion constants. In particular, fluorescently labeled polystyrene beads were used for calibration as this removed problems associated with fluorescence fluctuations encountered when using individual dye molecule. Next, a dependence on the laser excitation intensity has been performed

for both the beads and magnetite NCs with no sign of a power dependence. Furthermore, for all FCS measurements the detector count rate was adjusted with neutral density filters to a maximum of 5% of the saturation limit. Finally, variations in the autocorrelation function due to varying coverslip thicknesses were minimized by using the average of several calibration measurements that were performed each time with a new coverslip. The variation of magnetite NC hydrodynamic radii is therefore well outside the experimental uncertainty with respect to issues arising from the instrument calibration. Contamination of the solvent can also be ruled out as a source because blank water samples produced no signal (data not shown). Individual PKH 26 dye molecules have diffusion constants that are an order of magnitude larger (~ $3*10^{-10}$ m^2/s).[98,105] In addition, we verified that the distribution in recovered hydrodynamic radii does not originate from an insufficient number of fluorescence fluctuations for each FCS measurement or from a hindered diffusion of the magnetite NCs due to an attractive interaction with the coverslip surface, as discussed in section 3.3.6 above.

Although the most abundant measured hydrodynamic radius of 8 ± 1 nm is consistent with the NC size measured by TEM, the majority of the FCS measurements yielded a size larger than expected, indicating that the solutions must contain larger fluorescent particles as well.

The large variation of hydrodynamic radii measured for the same NC sample furthermore suggests that a small number of larger magnetite NCs or NC aggregates is present. This assignment is consistent with the poor quality of the autocorrelation fits with Equation 3.1, which assumes diffusion of only one species of a particular size. However, colloidal nanoparticle solutions always contain a distribution of particle sizes.

Because our FCS experiments were performed at low concentrations with less than one particle present per unit time, we can take advantage of analysis techniques that are commonly used in single molecule spectroscopy.[141-143] We therefore combined FCS with a single molecule burst intensity frequency analysis (BIFA).

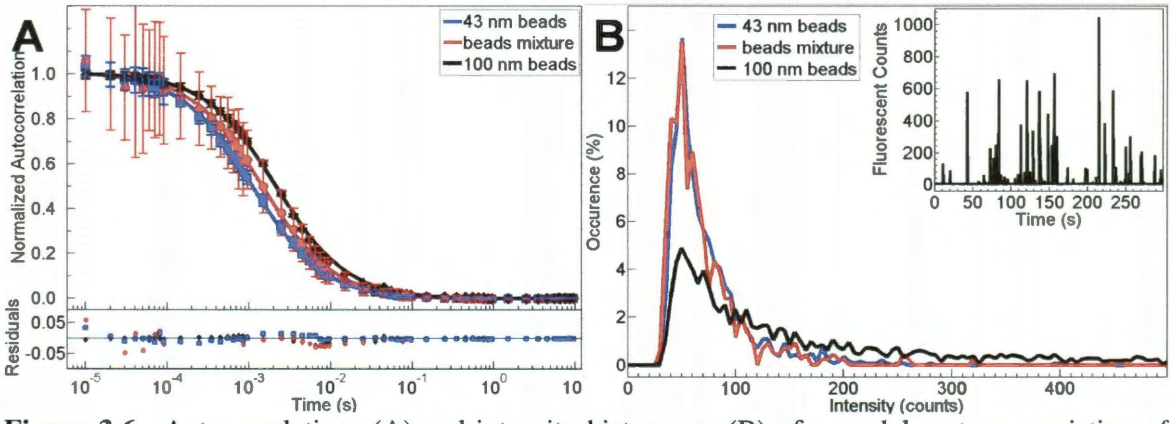

Figure 3.6. Autocorrelations (A) and intensity histograms (B) of a model system consisting of polystyrene dye beads in water. Assuming diffusion of a single species yields hydrodynamic radii of 24, 53, and 32 nm for 43 nm beads (blue), 100 nm beads (black), and a mixture of them (red). The corresponding intensity histograms show nearly identical distributions for the 43 nm beads and the mixture consistent with only a small concentration of 100 nm beads. The intensity histogram for 100 nm beads differs significantly, which is reflected by an increase in the median intensity from 60 to 120 counts. The inset in B shows a typical fluorescence trajectory for 100 nm beads.

We first tested the applicability of BIFA on a model system consisting of nearly monodisperse polystyrene dye beads. Autocorrelation analysis of 43 and 100 nm diameter polystyrene beads yielded diffusion constants of $1.1*10^{-11}$ and $4.9*10^{-12}$ m^2/s and hydrodynamic radii of 24 ± 2 and 50 ± 5 nm (Figure 3.6A) in excellent agreement with the size provided by Invitrogen (21.5 ± 3 and 50 ± 3 nm). Adding only 1.3% of 100 nm beads to the 43 nm beads causes a nearly 50% change in diffusion constant ($7.6*10^{-12}$ m^2/s) and hydrodynamic radius (32 ± 3 nm). In contrast, the burst intensity distributions (Figure 3.6B) and median intensities for the 43 nm beads and the mixture are the same with a value of 60 ± 5. The median intensity instead of the mean intensity was chosen

here for better comparison in order to avoid biasing from rare events with much larger intensities. The 100 nm beads have a significantly larger median intensity of 120 ± 11 with a much broader distribution. The intensity histogram thus reflects the true size distribution for the dye bead mixture more accurately than the standard autocorrelation analysis.

If the difference in particle brightness is accounted for, the autocorrelation for the dye bead mixture can be described quantitatively. The autocorrelation function for multiple species diffusing in solution is the average of the individual autocorrelation functions $G_i(\tau)$ which are weighted by the brightness η_i and the concentration $\langle C_i \rangle$ of each component i according to:[101,104]

Equation 3.5

$$G(\tau) = \frac{\sum (\eta_i \langle C_i \rangle)^2 G_i(\tau)}{\left(\sum \eta_i \langle C_i \rangle\right)^2}$$

Using the dye equivalent provided by the manufacturer as the brightness and the measured diffusion times τ_D of the 43 and 100 nm beads, the experimental autocorrelation curve of the dye bead mixture was fit using the ratio of concentrations $\langle C_i \rangle$ as the only adjustable parameter. Good agreement with the data is obtained for a concentration ratio of 98.7% 43 nm to 1.3% 100 nm beads (see red line in Figure 3.6A). This result shows that only a very small percentage of larger and brighter particles can cause a dramatic change in the deduced hydrodynamic radius for a mixture of particle sizes. In fact, a simulated autocorrelation with 4% of 100 nm beads is indistinguishable from a pure 100 nm bead sample (not shown). Note that, although dye labeling leads to a statistical distribution of brightnesses for each component i, η_i is assumed here to be the mean brightness.

BIFA of the magnetite NC samples confirms that the large variation of recovered hydrodynamic radii is indeed due to a small number (< 5%) of larger particle sizes. The intensity histograms for the same magnetite NC sample discussed in Figure 3.5 are almost indistinguishable, all having median intensities of 75 ± 9 (Figure 3.7A). In fact, the median intensities and number of events are independent of the measured hydrodynamic radius for the dye-labeled magnetite NCs studied here (Figure 3.7B). We estimated dye coverage of approximately 165 dye molecules per NC, which gives brightness comparable to polystyrene beads of similar size. We also checked that the dye labeling gives a normal distribution of brightnesses similar to 20 nm polystyrene beads containing ~ 180 dye molecules by sample scanning confocal microscopy of individual magnetite NCs deposited on a coverslip. A small number of larger and brighter magnetite NCs can therefore easily dominate the shape of the autocorrelation curve, irrespective of the actual mean of the particle size distribution.

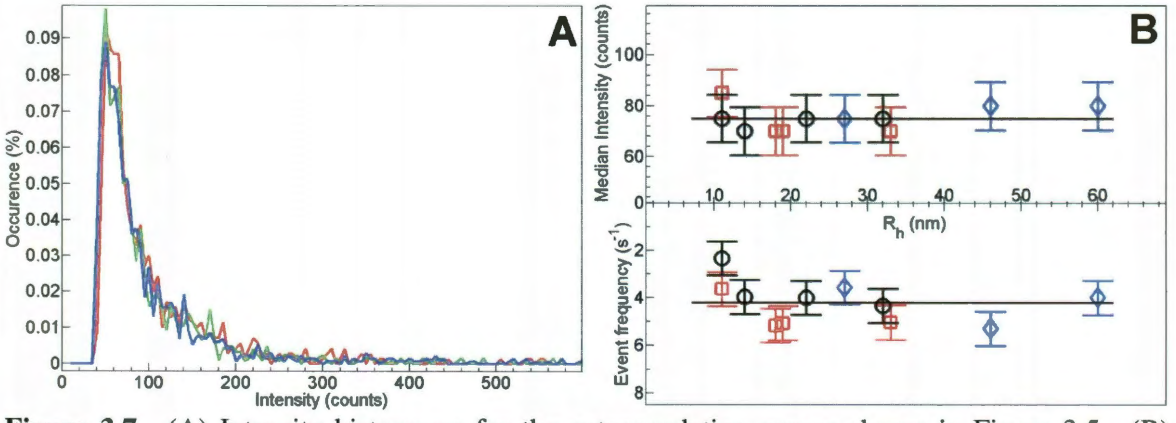

Figure 3.7. (A) Intensity histograms for the autocorrelation curves shown in Figure 3.5. (B) Median intensity (top) and event frequency (bottom) as a function of hydrodynamic radius Rh. Data points corresponding to FCS measurements taken before, during and after application of a magnetic field are given by blue diamonds, red squares and black circles, respectively. The horizontal lines represent the average values.

In order to verify that the larger particles present in the measured samples are either large NCs or aggregates of the 11 nm NCs, we performed FCS measurements before, during, and after applying a magnetic field by placing a 0.24 T magnet on top of the FCS sample chamber. We observed a size selective magnetic separation of larger magnetic NCs. For an applied magnetic field gradient of 870 T/m, particles had to exceed 60 nm in diameter before magnetic separation occurs. Figure 3.8A shows the mean hydrodynamic radii for three different samples measured before, during, and after application of the magnetic field. The corresponding autocorrelation curves are given in Figure 3.8B. The maximum hydrodynamic radius decreased from 60 nm to 33 nm by applying the magnetic field. BIFA furthermore confirms that the percentage of particles removed by the magnetic field is small because the burst intensity histograms recorded before, during, and after the application of the magnetic field are nearly identical (not shown) with no change in the average number of events and the median intensities (Figure 3.7B).

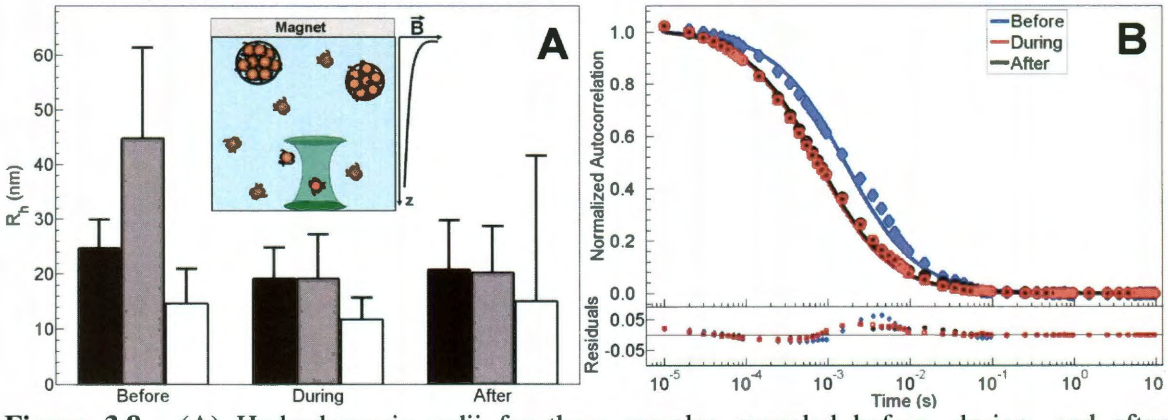

Figure 3.8. (A) Hydrodynamic radii for three samples recorded before, during, and after applying a magnetic field gradient of 870 T/m. The inset shows a schematic representation of the sample setup with an applied magnetic field. Only the larger aggregates migrate towards the magnet. (B) Average autocorrelation curves for the grey sample measured before (blue diamonds), during (red open circles), and after (black squares) applying a magnetic field. The recovered hydrodynamic radii Rh are 43, 19, and 20 nm, respectively.

Magnetic field-induced aggregation has been suggested as a mechanism for the low magnetic field gradient separation of magnetite NCs from water.[10] Using Cryo-TEM and small angle neutron scattering (SANS), Klokkenburg et al.[28,130,131] have recently shown a chain-like ordering of magnetite NCs caused by the alignment of individual dipole moments, which greatly depends on the size of the magnetic core and the applied magnetic field. In our FCS measurements, a magnetic field-induced aggregation of the magnetite NCs would lead to larger hydrodynamic radii and a decrease in the number of events. We first tested the effect of NC aggregation on FCS and BIFA by inducing aggregation with NaCl, Figure 3.9. A drop in the number of events by a factor of 2.3 upon aggregation is consistent with the change of diffusion constants by 2.5 times assuming that mostly aggregates consisting of only 2-3 particles have been formed. For the magnetic field dependent FCS measurements presented here, the number of events did not change for the applied magnet field (Figure 3.7B). However, the concentrations of the FCS samples are a factor of 1000 lower compared to the magnetite NCs solution that were previously used in a low magnetic field gradient separator.[10] Low NC concentrations are likely to prevent the observation of a magnetic field-induced aggregation during the course of the measurement (20 minutes). Future FCS experiments on dye-labeled NCs mixed together with an excess of non-labeled NCs to increase the overall NC concentration while permitting single particle sensitivity, will provide further insight into this important mechanism for low magnetic field gradient NC separation.

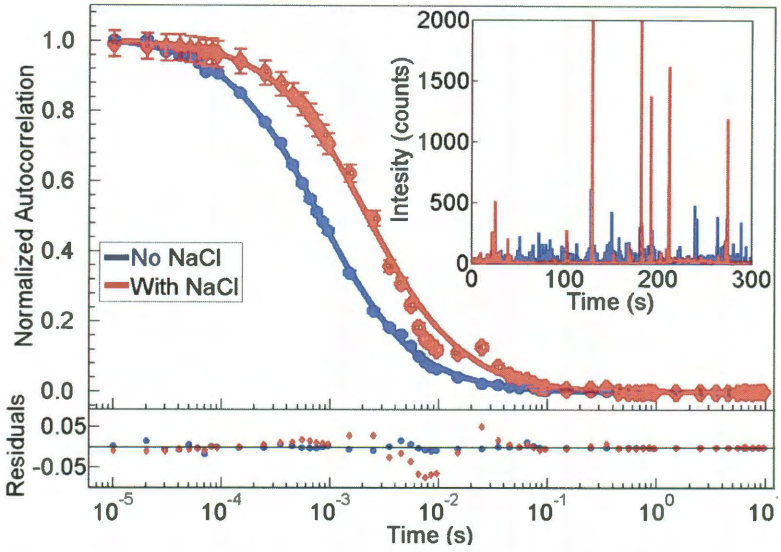

Figure 3.9. Salt-induced aggregation of magnetite NCs studied by FCS. Autocorrelation curves and fluorescence trajectories (inset) were recorded before (blue) and after (red) adding salt to the magnetite NCs.

With the FCS results from the magnetic field study, we can estimate an upper limit of the number of larger magnetite NCs by fitting the autocorrelation curve measured with an applied magnetic field to a size distribution that consists of a mixture of individual magnetite NCs (R_h = 8 nm) and NC aggregates with dimensions equal to the largest hydrodynamic radius recovered from runs with the magnetic field switched on (R_h ~ 30 nm). Assuming a cubic brightness dependence, the experimental autocorrelation curve in Figure 3.8B can be fit assuming four to five percent aggregate population (red data points and red solid line). This level of aggregation corresponds to an average of 56 to 70 out of 1400 total events per 300 second acquisition time. The actual number of aggregates is expected to be even lower because the same aggregate can enter the focal volume multiple times during the measurement. In addition, for this analysis we assumed an aggregate radius of only 30 nm, which presents the lower size

limit and therefore further leads to an overestimation of the concentration of larger particles.

The FCS measurements for the dye-labeled magnetite NCs as well as for the polystyrene beads highlight the strong dependence of autocorrelation signal on particle brightness. As a result, in order to measure the size of nanoparticles using correlation spectroscopic techniques it is necessary to take into account the size dependence of the nanoparticle optical properties. If the latter is known together with the shape of the size distribution (i.e., Gaussian, log-normal, etc.), the measured autocorrelation function can be fitted to accurately obtain the actual particle size distribution. However, for an unknown, heterogeneous size distribution as in the two systems measured here or for a multi-component sample,[104] care must be taken when interpreting the measured hydrodynamic radii. Similar complications can arise when the particle brightness varies due to fluorescence intermittency as observed in semiconductor NCs.[61,97,98]

3.5 Conclusions

In conclusion, we have successfully measured the diffusion of dye-labeled magnetic NCs with an 11 nm magnetite core in water by FCS. If autocorrelation data were analyzed without accounting for size dependent fluorescence, then the sample's apparent hydrodynamic radii varied by as much as an order of magnitude for the same magnetite NC sample due to the presence of a few percent of larger aggregates. To remove this bias we applied a burst intensity fluorescence analysis to directly measure signal intensity thereby removing the artificial weighting of brighter signals. We were able to gain insight into the size distribution of the magnetite NCs by combining FCS

with single molecule BIFA. Size-selective separation of aggregates larger than about 60 nm in diameter corresponding to an effective magnetite core size of 30-35 nm was achieved by applying a magnetic field of 0.24 T. Individual 11 nm magnetite NCs did not separate on the short timescales of this experiment. The results obtained here together with the analytical methods will enable us in the future to study the detailed NC size and magnetic field strength dependence of the separation of magnetic NCs. Using single molecule correlation spectroscopy techniques for the real-time measurement of the forces acting on nanometer magnetic particles inside a low magnetic field gradient separator will be crucial for the understanding and improvement of magnetic NC based separations systems.

3.6 Acknowledgements

This work was supported by the Nanoscale Science and Engineering Initiative of the National Science Foundation under NSF Award Number EEC-0647452, Robert A. Welch Foundation (Grant C-1664). I would also like to thank Dr. Carmen Reznik and Dr. Christy Landes for many fruitful discussions regarding the application and analysis of FCS.

CHAPTER 4
PROBING A CENTURY OLD PREDICTION ONE PLASMONIC PARTICLE AT A TIME[3]

4.1 Abstract

In 1908 Gustav Mie solved Maxwell's equations to account for the absorption and scattering of spherical plasmonic particles. Since then much attention has been devoted to the size dependent optical properties of metallic nanoparticles. However, ensemble measurements of colloidal solutions generally only yield the total extinction cross-sections of the nanoparticles. Here we show how Mie's prediction on the size dependence of the surface absorption and scattering can be probed separately for the same gold nanoparticle by using two single particle spectroscopy techniques: 1) dark-field scattering and 2) photothermal imaging, which selectively only measure scattering and absorption, respectively. Combining the optical measurements with correlated scanning electron microscopy furthermore allowed us to measure the size of the spherical gold nanoparticles, which ranged from 43 to 274 nm in diameter. We found that even though the trend predicted by Mie theory is followed well by the experimental data over a large range of nanoparticle diameters, for small size variations changes in scattering and absorption intensities are dominated by factors other than those considered by Mie theory. In particular, spectral shifts of the plasmon resonance due to deviations from a spherical particle shape alone cannot explain the observed variation in absorption and scattering intensities.

[3] This chapter is based on the manuscript titled "Probing a century old prediction one plasmonic particle at a time" by Alexei Tcherniak, Ji Won Ha, Sergio Dominguez-Medina, Liane Slaughter and Stephan Link, published in *Nano Letters* **2010**, *10* (4), pp 1398–1404

4.2 Introduction

Plasmonic nanoparticles (NPs) have attracted significant attention in various fields because of their size and shape tunable optical properties. Possible applications of metallic NPs range from sub-wavelength optical devices,[144-146] catalysis,[34] biological sensing[29,30,147,148] and imaging,[149-152] to disease diagnostics and treatment.[23,153,154] In contrast to smaller molecules, the surface plasmon oscillation of NPs gives rise to both strong absorption and scattering of the incident light.[6,155] Many modern applications of plasmonic NPs rely on either their absorption or scattering properties. Thus, it is useful to obtain experimental information about how these properties evolve with NP size and shape so that the optimal plasmonic NPs can be designed for a particular use. For example, the sensitivity of plasmonic sensors that are based on spectral shifts of the surface plasmon scattering spectrum[29,30] benefit from increasing the NP size and hence scattering intensity. However, this is usually accompanied by an increase in absorption efficiency and hence photothermal heating of the environment as well. Because DNA bound to the surface of gold NPs is very sensitive to the local temperature,[156,157] for studies that rely on biomolecular recognition[30,158] it is important to minimize absorptive photothermal heating and hence to compromise with respect to the magnitude of the scattering signal. On the other hand, photothermal cancer therapy with plasmonic NPs relies on both absorption for heat delivery and scattering for imaging.[23] It is therefore vital to know the ratio between absorption and scattering cross-sections in order to correctly estimate the NP coverage and temperature change from the scattering images.[159,160]

The size dependent absorption and scattering cross-sections of spherical metallic NPs were solved analytically by Gustav Mie in 1908.[161] His theory predicts that the absorption and scattering cross-sections as well as the scattering-to-absorption ratio increase with increasing NP size.[6,155,161,162] Although many studies have shown excellent agreement between UV-vis spectra and Mie theory,[6,150,155,163] typical ensemble measurements yield the total extinction only, i.e. the sum of absorption and scattering. Experimentally separating the contributions of absorption and scattering to the spectra of plasmonic NPs is more difficult, but can be accomplished by combining extinction measurements with off-axis scattering[164] or photo-acoustic spectroscopy.[165] Nevertheless, size and shape inhomogeneities of typical colloidal NP samples remain a major disadvantage in ensemble optical measurements as only average values can be obtained.

Ensemble averaging of optical properties due to inhomogeneous NP size distributions is eliminated using different single particle spectroscopy techniques.[38,59,162,166-171] Furthermore, it is possible to separately measure either surface plasmon absorption[59,168,172,173] or scattering.[38,169,170,174,175] Surface plasmon *scattering* from individual NPs is most commonly detected by dark-field microscopy, which has been used to determine the plasmon resonances and linewidths of single NPs with different sizes and shapes[38,169,175-177] including spherical gold NPs with diameters between 20 and 150 nm.[178] However, the magnitude of the scattering intensity is often neglected in these single particle studies. On the other hand, single particle *absorption* spectra of gold NPs with mean diameters of 5, 10, 20, and 33 nm have been recorded independently using photothermal imaging.[173] In addition, the size dependence of the

photothermal signal intensity at 532 nm has been determined for NPs with average diameters up to 75 nm.[166,168]

Although single particle spectroscopy yields the homogeneous linewidth, the spectra can vary greatly among the individual NPs even for the same sample. This arises from small inhomogeneities in NP size and shape, including the presence of small aggregates, different orientation of the NPs with respect to the incident radiation, variations in the local dielectric function of the surroundings, and interactions of the NP with the substrate.[38,173,177-182] Because optical and structural characterizations of metallic NPs have mostly been performed separately, only the mean values and their standard deviations for the plasmonic response and the NP dimensions could be correlated with each other. To circumvent some of these issues, optical studies have to be carried out on the same individual NPs that are also characterized by a structural imaging technique such as transmission or scanning electron microscopy (TEM or SEM). This can be achieved using substrates with registration marks that allow for identification of the same areas in optical and electron microscopes. Such an approach, although tedious, has been taken more recently especially for correlating the scattering spectra with the shapes of non-spherical NPs.[38,175-177,179,182-184]

To directly probe Mie's prediction for the size dependence of the absorption and scattering of spherical metallic NPs over a large range of diameters with single particle resolution, we measured both *absorption and scattering* intensities of the *same* individual NPs that were also characterized by SEM. This was accomplished using single particle photothermal imaging and laser dark-field scattering, both carried out using 532 nm as the exciting wavelength for five samples of spherical gold NPs with average diameters *d*

varying from 51 to 237 nm. We found good general agreement with the size dependence predicted by Mie theory considering the entire size range. In particular, for the largest NPs we observed the departure from the simple scaling laws of d^3 and d^6 for the absorption and scattering intensities, respectively.[6,155,162] However, our results also show that factors other than the NP size lead to strong fluctuations in the often less analyzed absorption and scattering *intensities* even for NPs with comparable diameters.

4.3 Experimental

4.3.1 Sample preparation

Gold NPs were purchased from NanoPartz (10, 51, 76, and 88 nm diameter NP samples) and Ted Pella (155 and 237 nm diameter NP samples) and were used as purchased. Patterned glass substrates were prepared by evaporating gold on plasma cleaned coverslips (Fisher Scientific), to which indexed TEM grids (Ted Pella) had been taped beforehand.[38] The gold formed a uniform layer on the coverslip and the TEM grid; after the TEM grid was peeled off, areas of clean glass were exposed. The pattern helped in locating the same NPs in the electron and optical microscopes. Stock solutions were sonicated and diluted 20-50 times with deionized water. Samples for single particle measurements were then prepared by drop casting the NP solutions. SEM images were taken on a FEI Quanta ESEM2 operated at 30 kV under low vacuum in a water vapor atmosphere to avoid charge buildup on the nonconductive glass substrates. The estimated uncertainty in determining the NP size was approximately 4 nm. Optical extinction measurements were performed with a home-built spectrometer consisting of a halogen lamp (OSL1, Thorlabs) as a light source and a fiber-coupled spectrometer

(S1024DWX, Ocean Optics). Spectra were integrated for 100 ms and averaged 100 times.

4.3.2 Mie theory calculations

Mie theory calculations were carried out using FORTRAN code following the algorithm given in Bohren and Huffman.[6] For the dielectric function of gold we used the tabulated values by Johnson and Christy.[185] To compare Mie theory calculations to ensemble extinction measurements the medium refractive index was set to 1.33, while for the single particle experiments we used a refractive index of 1.25 as an average between air and glass.[166] Experimentally the scattered light was integrated over a collection angle that was defined by the numerical aperture of the objective. In our reflected light setup, it was predominantly the back-scattered signal that was detected by the objective. This is important because Mie theory predicts that, as the size of NPs increases, most of the light is scattered in the forward direction.[6] We therefore accounted for this effect using numerical simulations (discrete dipole approximation calculations with DDSCAT 7.0[186]) that give the size dependent NP cross sections for different scattering angles. A correction factor was then computed based on the ratio of the intensity integrated for the experimental collection cone divided by the total scattering intensity. The data presented in Figure 4.6 already includes this correction for the experimental collection geometry. For NPs below about 100 nm, the detection geometry does not play a significant role.[187] Indeed, our calculations also showed that only for the 237 nm NPs the correction factor deviates significantly from that of the other samples.

4.3.3 Laser dark-field imaging

Dark-field imaging is a common technique used to study single metallic NPs. White light from a halogen lamp is traditionally used as an illumination source.[38,169,170,175] To obtain the scattering intensities at a fixed wavelength, we employed a laser for excitation instead of a lamp.[188-190] This also gave us access to a larger range of excitation powers and enabled a comparison with the absorption intensities measured by photothermal imaging, a technique that relies on laser rather than lamp excitation.[168] Our laser dark-field imaging setup is shown in Figure 4.1A. It is similar to a conventional microscope setup with reflected light dark-field illumination. Instead of expanding the laser beam to match the profile of the light from a lamp[47] or using axion lenses,[190] we directed the laser through the outer ring of a dark-field objective.[189,191] The laser dark-field imaging setup consisted of an inverted microscope (Axio Observer, Zeiss) with a 100X objective (Epiplan, Zeiss). A solid state laser operating at a wavelength of 532 nm (Verdi V6, Coherent) was used for excitation. The laser light was linearly polarized before entering the microscope and was mostly polarized parallel to the glass substrate at the sample. Incident laser light illuminated the sample at an angle of about 60 degrees with respect to the surface normal, while only light scattered by the NPs was collected using the same objective. The collection cone for the scattered light was defined by the numerical aperture of the objective (NA = 0.75) and had an opening of less than 50 degrees, defined again with respect to the surface normal. The scattered light was focused on an avalanche photodiode (PDM 50CT SPAD, Micro Photon Devices), and the signal was acquired with a photon counting board (PCI-6602, National Instruments). Dark-field scattering images were formed by scanning the sample using a piezo stage (P-

517.2CL, Physik Instrumente). In this setup the area of the detector effectively acted as a confocal pinhole. The photon counting board and scanning stage were controlled by a program written in LabView. 88 nm NPs were measured at the beginning of each experiment to optimize the instrument and establish a reference for the other samples.

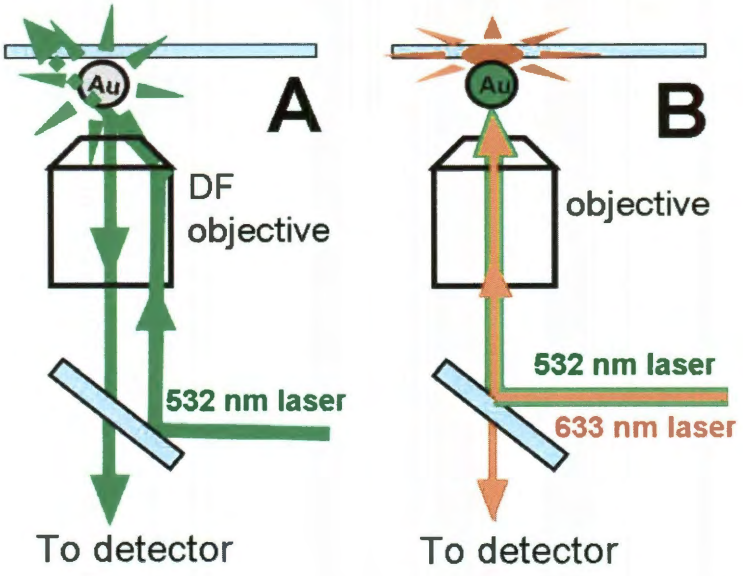

Figure 4.1. Schematic of the experimental setups for laser dark-field (A) and photothermal imaging (B). A - The 532 nm laser was directed through the outer ring of a dark-field objective. The scattered light by the NPs was collected in reflection mode using the same objective. B - The 532 nm laser heated the NPs and their surrounding following surface plasmon absorption. The change in refractive index due to the local change in temperature was detected by the 633 nm probe beam. We ensured that the peak absorption and scattering intensities for each NP sample was detected by independently optimizing the foci of the exciting laser beams in the two types of experiments.

4.3.4 Single particle scattering spectroscopy

Single particle scattering spectra were acquired using the same microscope setup already described. A halogen lamp was used for excitation and the scattered light was redirected to a spectrometer (Acton SP2150i, Princeton Instruments) equipped with a CCD camera (PIXIS 400BR, Princeton Instruments). The excitation light was unpolarized and a depolarizer was inserted before the spectrometer.

4.3.5 Photothermal imaging

We implemented a photothermal imaging setup as originally described by Berciaud *et al.*[168] Photothermal imaging requires the combination of a time-modulated heating beam and an off-resonance probe beam. A schematic diagram of the setup is shown in Figure 4.1B. A 532 nm diode laser (Compass 315M-100SL, Coherent) and a 633 nm HeNe laser (JSD Uniphase) were used as the heating and probe beams, respectively. The intensity of the heating beam was modulated at 300 kHz by an acousto-optic modulator (IntraAction) driven by a function generator (Exact Electronics). Both laser beams were focused with a 100X objective (Epiplan, Zeiss). The reflected probe beam was collected with the same objective and sent to a 125 MHz photoreceiver (New Focus). The signal was demodulated using a lock-in amplifier (Princeton Applied Research) and processed by a surface probe microscope controller (SPM 1000, RHK Technology). Images were acquired with a piezo scanning stage (P-517.3CL, Physik Instrumente). 88 nm NPs were measured at the beginning of each experiment to optimize the instrument and establish a reference intensity for the other samples. Because laser irradiation can cause nanoparticle melting,[192] we used low excitation powers of 500 μW for the heating beam. We furthermore confirmed the absence of significant shape changes of the NPs by performing SEM before and after the photothermal imaging experiments.

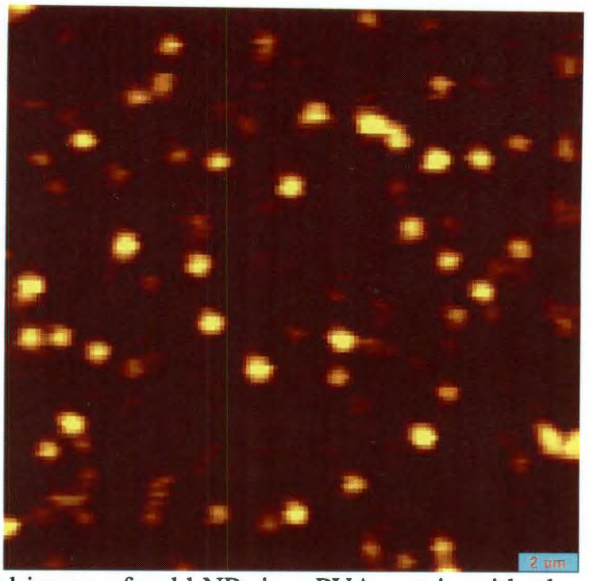

Figure 4.2. Photothermal image of gold NPs in a PVA matrix with glycerol added on top of the sample. The diameter of the NPs was 10 nm according to the specifications of the manufacturer (NanoPartz).

For photothermal imaging, the highest signal to noise ratios can be achieved if the NPs are homogeneously embedded in a medium which facilitates efficient heat transfer between the NPs and their surrounding.[168,172] Figure 4.2 shows a photothermal image of 10 nm NPs in a PVA matrix with glycerol added on top of the sample, as suggested by the developers of photothermal imaging.[168] This sample was prepared by spin casting the 10 nm NPs from a water solution containing 0.5 wt.-% PVA. Despite the loss in sensitivity we decided to carry out all photothermal imaging experiments without the polymer matrix and glycerol so that the same NPs could be compared directly and repeatedly between the different imaging methods. In particular, SEM imaging before and after the optical experiments would not have been possible otherwise. With the NPs supported by the glass substrate and surrounded by air heat transfer is restricted to the glass only, which impedes a homogeneous heating of the surrounding medium. We indeed observed a decreased sensitivity in our photothermal imaging experiments. However, the NPs studied here were relatively big with the smallest size about an order

of magnitude larger than the detection limit.[168] The experimental error in photothermal signal was estimated to be about 10% from repeated measurements of the same NPs. However, even when considering the experimental conditions it is, at this time, not clear why the mean absorption intensity for the 155 nm NP sample differs more significantly from the calculated value especially in comparison to the much better agreement between experiment and theory for the other samples.

4.4 Results and discussion

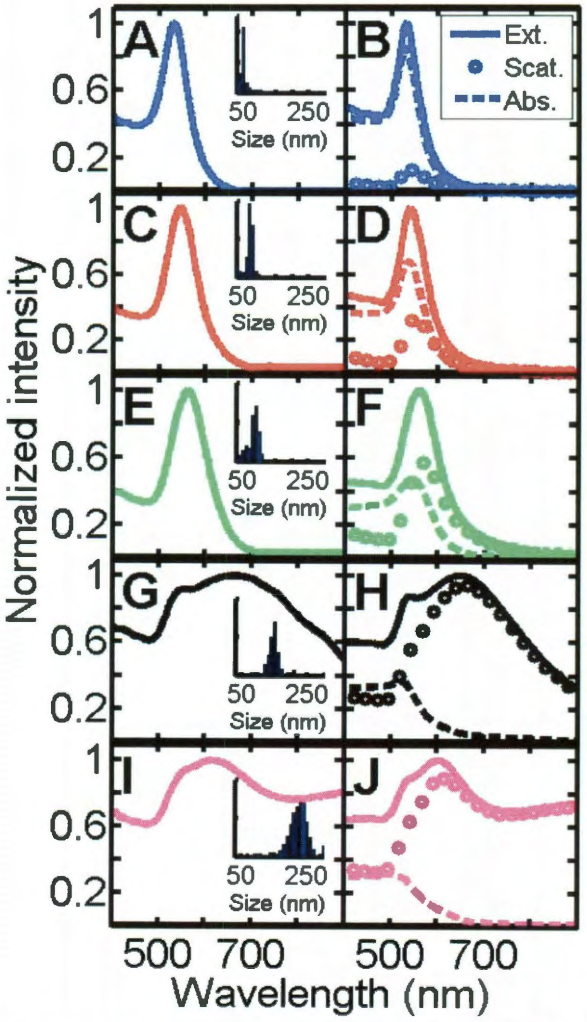

Figure 4.3. Experimental ensemble extinction (left column) and Mie theory spectra (right) for spherical gold NPs with different mean sizes: A, B – 51 nm, C, D – 76 nm, E, F – 88 nm, G, H – 155 nm, and I, J – 237 nm. The Mie theory extinction spectra (solid lines) can be separated into

contributions from scattering (open circles) and absorption (dashed lines).

We selected five gold NP samples with average diameters ranging from 51 to 237 nm so that the relative contributions from absorption and scattering change from absorption-dominated for the smaller NPs to scattering-dominated for the larger NPs. Each sample was first characterized by ensemble extinction spectroscopy and SEM. In Figure 4.3 the extinction spectra are compared to Mie theory calculations carried out for the mean NP sizes for each sample. Considering that the average experimental size distributions of 15 % were not included in these calculations, the agreement between theory and experiment is excellent even for the larger 155 and 237 nm NPs, which show higher order plasmon resonances in addition to the dipole mode due to phase retardation effects.[6,155] For the three smallest NP samples with average diameters of 51, 76, and 88 nm the linewidths of the dipole plasmon resonance are in good agreement with the values obtained from the theoretical spectra. The line widths defined as the full width at half maximum were computed by fitting a single Lorentzian curve to each spectrum giving 0.24, 0.29 and 0.38 eV for the experimental spectra of the 51, 76, and 88 nm NPs, respectively. The corresponding theoretical values are slightly narrower with 0.23, 0.28, and 0.36 eV. However, this is commonly found for ensemble measurements, in which the broadening can be attributed to the size and shape inhomogeneity of the NPs.[38,173,182] Because of the multiple overlapping peaks for the two largest NP samples with diameters of 155 and 237 nm, we were not able to determine the line widths of their dipole plasmon resonances.

Mie theory allows one to separately calculate the pure absorption and scattering spectra,[6,155,161] while ensemble UV-vis spectroscopy yields the sum of both processes, i.e.

the extinction. Figure 4.3 B and D show that absorption (dashed line) dominates for the 51 and 76 nm NPs. However with increasing NP diameter, scattering (open circles) increases more steeply and becomes about equal in strength compared to absorption for 88 nm NPs (Figure 4.3F). For 155 and 237 nm NPs scattering is much stronger than absorption and dominates the overall extinction spectrum (Figure 4.3 H and J). Furthermore, it is evident from the spectra in Figure 4.3 that the ratio between absorption and scattering is not constant for all wavelengths, but depends strongly on the spectral dependence of the absorption and scattering as a function of NP size. A quantitative comparison between absorption and scattering for different NP sizes is therefore best accomplished either by defining integrated spectral densities or at a particular wavelength.

Here we chose 532 nm to compare absorption and scattering cross-sections because this wavelength is close to the maximum of the plasmon resonance and lasers operating at 532 nm are widely used in different imaging and spectroscopy applications. To obtain the size dependent absorption and scattering cross-sections at 532 nm, we performed Mie theory calculations for NP diameters ranging from 20 to 300 nm, as shown in Figure 4.4. The inset in Figure 4.4 illustrates how the ratio between absorption and scattering cross-sections scales with NP size. For a wavelength of 532 nm and assuming a refractive index of 1.25, the scattering cross-section becomes larger than the absorption cross-section for a NP size of 102 nm. For applications that utilize only scattering such as imaging and tracking of single NPs in cells,[23,151,152,154] one can thus predict theoretically the optimal NP size for maximizing the scattering intensity while minimizing the absorption efficiency and hence unwanted photothermal heating of the surrounding medium. For example, according to Figure 4.4 the absorption cross-section

grows by less than 10% for NPs with diameters from about 90 to 120 nm, while the scattering cross-section increases by over 90%.

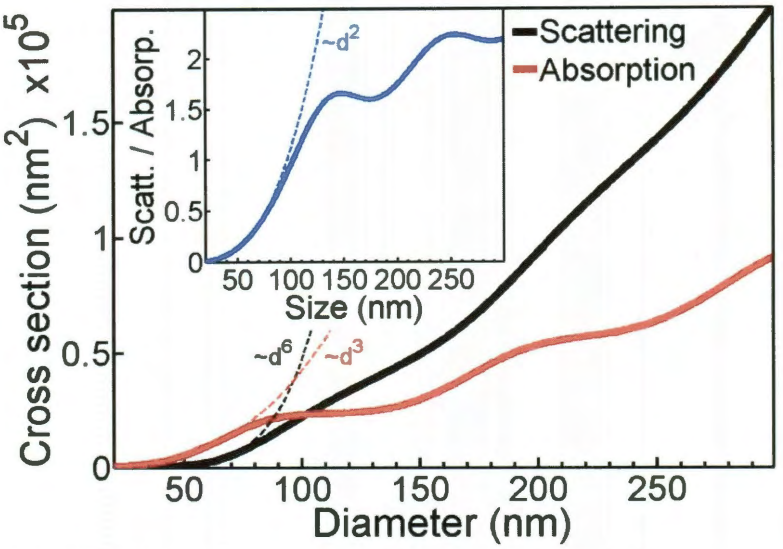

Figure 4.4. Mie theory prediction for scattering (black) and absorption (red) cross-sections as functions of NP size at a wavelength of 532 nm and with a medium index of refraction of 1.25. Inset: Ratio of scattering and absorption cross-sections as a function of NP size. The dashed lines show how simplified power dependences are only accurate for NP sizes below 80 nm.

Simple scaling laws have been assumed for the size dependence of the surface plasmon absorption and scattering.[25,160,162,173] If the NPs are substantially smaller than the wavelength of the light, the absorption and scattering cross-sections then scale as d^3 and d^6, respectively. The dashed lines in Figure 4.4 illustrate this dependence. While for NPs smaller than ~ 80 nm these approximations reproduce Mie theory well, it is clear that for larger NPs larger these simple scaling laws are no longer applicable. The deviation from the d^3 and d^6 behavior occurs as the NP size becomes comparable to the wavelength of the interacting light due to phase retardation effects. One must therefore take care when comparing cross-sections for larger NPs. The trends shown in Figure 4.4 are furthermore strongly dependent on the wavelength and the refractive index of the medium.

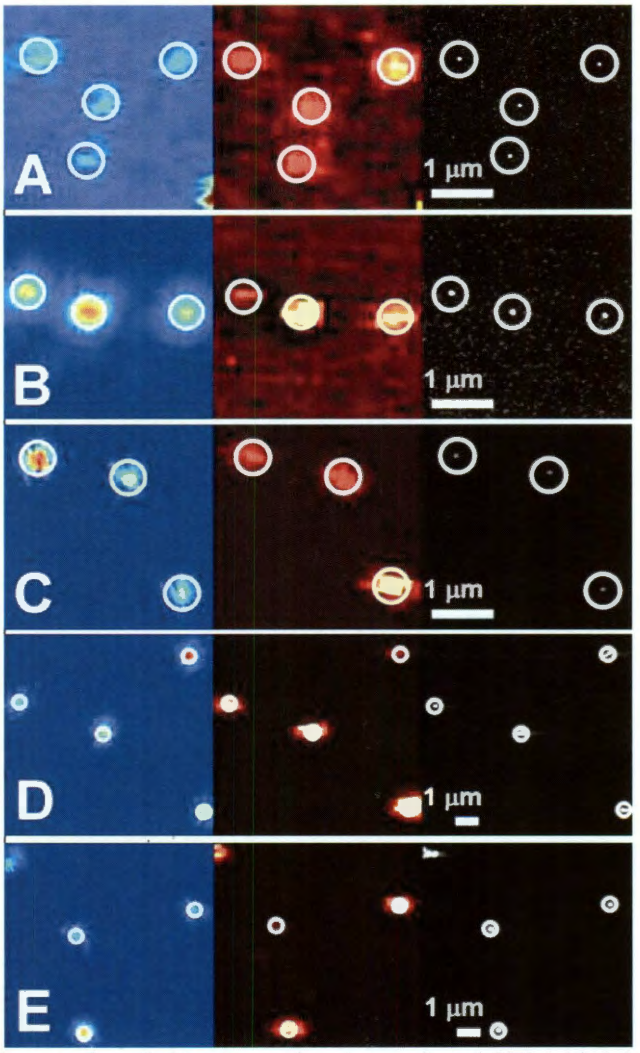

Figure 4.5. Correlated scattering (left), absorption (center) and SEM (right) images of the same NPs for the five samples shown in Figure 4.3: A – 51 nm, B – 76 nm, C – 88 nm, D – 155 nm, and E – 237 nm. White circles are given as guides to the eye. They also provide the size of the signal area used in the intensity analysis. The sizes of an individual pixel were 60 and 150 nm for the scattering and absorption images, respectively. See experimental section for details.

To test the predictions from Figure 4.4 experimentally, we performed single particle absorption and scattering measurements on the same NPs that were also characterized with SEM. Correlated structural imaging and optical spectroscopy can avoid averaging the plasmonic properties of heterogeneous samples as is otherwise inevitable for characterizing chemically prepared colloidal NPs with ensemble techniques. Moreover, single particle techniques can turn heterogeneity into an advantage as more

data points can be collected from a single sample. This is particularly important in this case where we are interested in mapping out the size dependences of the surface plasmon absorption and scattering intensities for spherical NPs. We measured the scattering and absorption intensities of individual gold NPs at 532 nm using dark-field scattering with laser excitation and photothermal imaging,[168,173] which employs two laser beams: one to heat the NPs and the other to detect the resulting changes in the local refractive index. The details of both setups are discussed in detail in the experimental section. The same NPs were also characterized using SEM. Figure 4.5 shows magnified views of correlated images obtained from these three different techniques for the five NP samples characterized in Figure 4.3.

This approach allowed us to correlate the NP size, absorption, and scattering intensities for many NPs. The NP size was calculated from high magnification SEM images of individual NPs using an automated image analysis program written in Matlab. The algorithm identified pixels that belonged to the same NP and performed a principle component analysis to determine the main NP axes. The size of the NP was then taken as the average dimensions along the first two components. We estimated the uncertainty in determining the size for each dimension to be about 4 nm based on the magnification and quality of the SEM images. Assuming spherical NP shape, the relative uncertainty in the NP volume therefore ranged between 24% for the 51 nm NPs and 5% for the 237 nm NPs. Absorption and scattering intensities were calculated by summing over all pixels that were associated with a NP based on the diffraction-limited resolution of our setups (~ 500 nm). The signal was also corrected for the local background intensity using adjacent pixels around each NP. In Figure 4.5 the white circles approximate the areas that were

used to calculate the corresponding signal. Note that the single particle samples for the two largest NP sizes had in general a lower NP coverage and therefore the scale is smaller for those images. In addition to determining the NP size, correlated SEM images were also used to locate the precise positions of NPs with low absorption and scattering intensities and to exclude small NP aggregates from the analysis, which was not always possible based on the signal intensity only.

With the measured NP sizes and the corresponding signals from the dark-field scattering and photothermal images, Figure 4.6 was constructed which shows the scattering (A) and absorption (B) intensities as a function of NP diameter for about 25 gold NPs for each of the five samples. The trend predicted by Mie theory is given by the solid black line and is well reproduced by the experimental data points when considering the entire size range. Each data point (open circles) represents a NP that was unambiguously identified by all three imaging methods. Because only relative intensities and not absolute cross-sections were measured, the experimental data was scaled so that the mean absorption and scattering for the 88 nm NP sample have the same values as the ones calculated using Mie theory. Any NP size could have been chosen for this normalization, but we selected this particular size because it also served as a reference when measurements were repeated on different days.

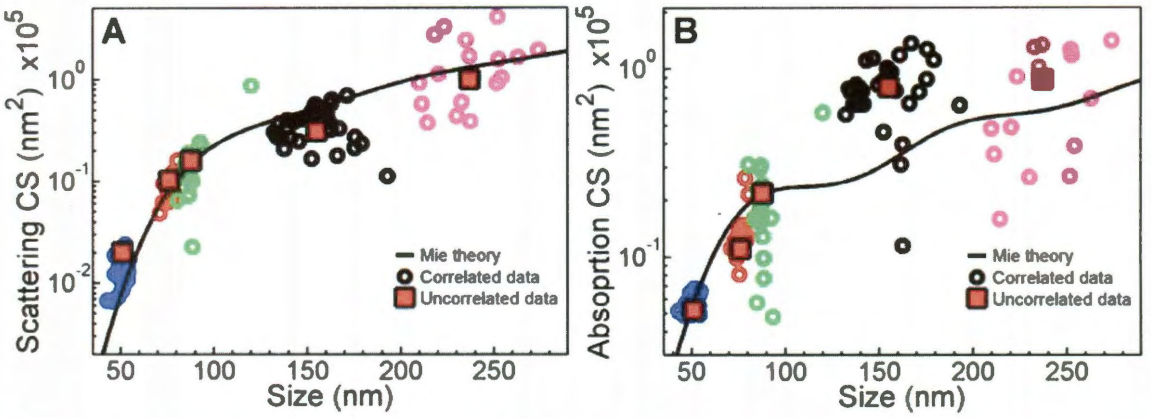

Figure 4.6. Gold NP scattering (A) and absorption (B) as a function of size at 532 nm. Trends predicted by Mie theory are shown as solid black lines. SEM correlated data points are shown as open circles with each sample colored coded according to Figure 4.3. The experimental error is approximately equal to the size of the data points. The red squares give the mean scattering and absorption intensities of at least 250 NPs for each sample obtained from intensity distributions for which the optical measurements were not correlated with SEM images (uncorrelated data). Note the different scaling of the y-axis for scattering and absorption and that the experimental collection geometry has been taken into account to scale the experimental data correctly (see Section 4.3.2 for details).

As seen in Figure 4.6, a major advantage of single particle measurements is that not just average intensity values, but also the entire intensity distributions are obtained directly. The mean intensities for the five samples show good agreement with the size dependence of the absorption and scattering cross-sections based on Mie theory. However, for NPs with similar sizes there is a significant variation of comparable magnitude for both the absorption and scattering intensities. The observed spread cannot be explained by the experimental error associated with determining the intensity values from the absorption and scattering images. We imaged randomly selected sample areas several times on the same and different days and estimated an uncertainty of about 10% for both the absorption and scattering intensity independent of the NP size. In contrast, the observed intensities had relative standard deviations varying from about 30% to nearly 100%.

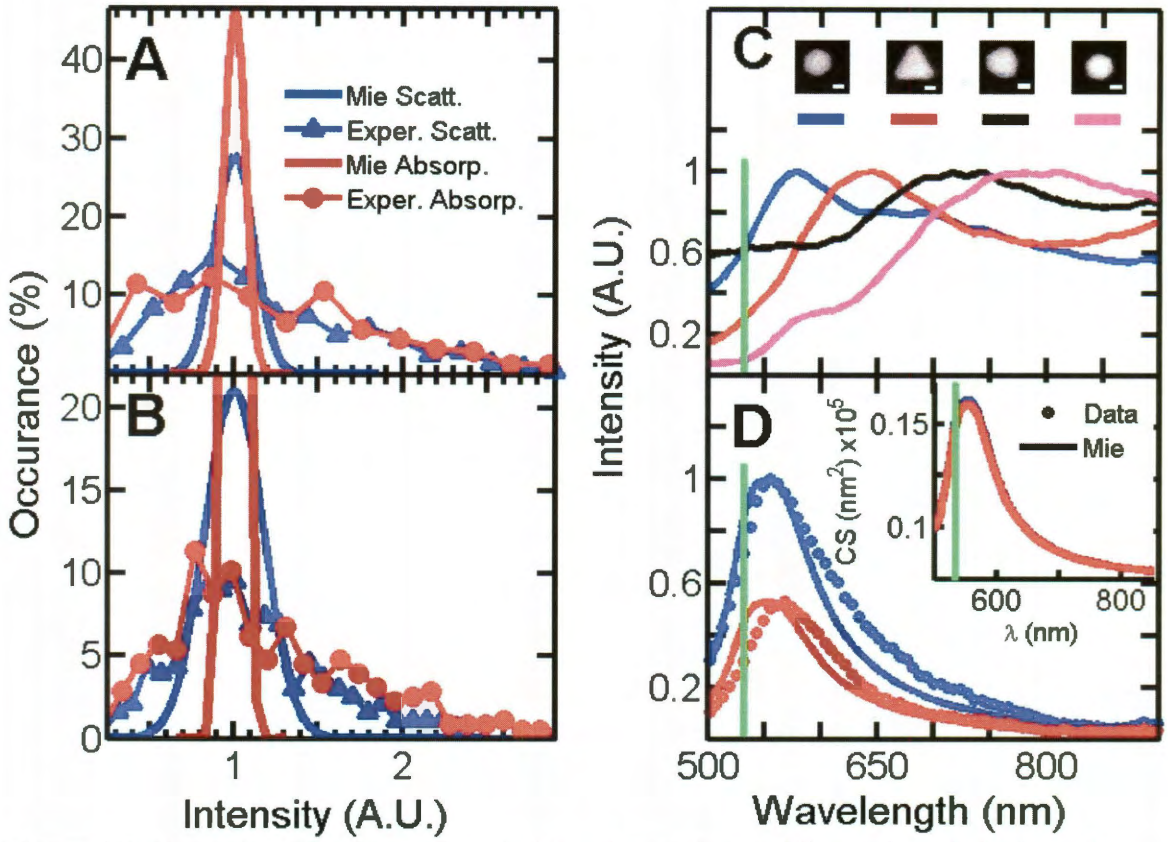

Figure 4.7. Absorption (blue line and symbols) and scattering (red line and symbols) intensity histograms constructed from at least 250 NPs for the 237 (A) and 88 (B) nm samples. Solid lines correspond to Mie theory calculations assuming the NP size distribution determined by SEM. Each histogram was normalized to 100% and centered at an arbitrary intensity of 1. (C) Normalized single particle scattering spectra selected from the 237 nm sample and corresponding high magnification SEM images. (D) Single particle scattering spectra for 88 nm (blue symbols) and 87 nm (red symbols) NPs. Calculated spectra (solid lines) using Mie theory and scaled to the experimental amplitudes are included for comparison. The inset shows the same calculated spectra, but plotted as scattering cross-sections (CS). The green vertical lines mark the 532 nm laser excitation wavelength for the dark-field imaging experiments.

The variations in NP size were implicitly taken into account by correlating the absorption and scattering intensities with the dimensions obtained from the SEM images. However, the data shown in Figure 4.6 only represents a small subset of the NPs contained in each sample. To improve the statistical significance of our experiments we collected the absorption and scattering intensities of at least an additional 250 NPs for each sample, but without correlated SEM imaging. Although the presence of some NP

aggregates could not be excluded, the impact that the aggregates had on the results was minimal. Based on the correlated SEM studies the percentage of aggregates was low (about 5 %) for the 51, 76 and 88 nm samples. For the two larger NP samples, the intensity histograms showed a distinctive bimodal distribution and aggregates were easily excluded using an upper intensity cutoff. The mean intensities from these measurements are included in Figure 4.6 as the uncorrelated data points (red squares). The good agreement between the mean uncorrelated absorption and scattering intensities and the corresponding correlated data justifies our analysis.

To evaluate the distributions in more detail, the histograms of uncorrelated absorption and scattering intensities are shown in Figure 4.7 A and B (symbols) for the 237 nm and 88 nm NP samples, respectively. The experimental intensity distributions were fitted to single Gaussian curves, which are shown as dashed lines for visual comparison. Included in Figure 4.7 A and B are also the histograms that are expected theoretically, based on the measured size distributions from Figure 4.3 and Mie theory. Each histogram was normalized to 100% and centered at an arbitrary intensity of 1 by dividing all values by the means of the fitted Gaussian curves. This was done to aid in the visual comparison of the widths for the different histograms. Because surface plasmon absorption and scattering cross-sections scale differently with NP diameter as discussed in Figure 4.4, the widths of the intensity histograms differ for absorption and scattering as clearly seen from the theoretical curves in Figure 4.7. However, the experimental absorption and scattering intensity distributions are nearly equal and broader by at least a factor of 2 compared to the ones expected from the NP size variations. Although only the data from the 237 and 88 nm NPs is shown, we found very

similar intensity variations for SEM correlated and uncorrelated measurements for all five NP samples. Therefore, the NP size distribution alone cannot explain the much larger variations in the observed absorption and scattering intensities.

In addition to variations in size, we found that the shape of some NPs deviated strongly from an ideal sphere. In particular, the larger NP samples (155 and 237 nm) showed stronger shape variations than the smaller ones (51, 76, and 88 nm). In our analysis, however, we have not excluded any NPs based on their shape (or any other parameter, thus representing the behavior of real colloidal NP samples under typical single particle imaging conditions). Instead, we assumed that all NPs are spheres with the diameter given as the average of the first two principal components. Of course this approach also treated the NPs as 2-dimensional objects despite their sometimes complex 3-dimenesional shapes. Because the NP shape has a much bigger effect on the surface plasmon absorption and scattering spectra than the NP size, [6,155,182] significant changes in the absorption and scattering intensities could result from spectral shifts of varying magnitudes due to shape inhomogeneity. We therefore measured single particle scattering spectra using a white light excitation for randomly selected NPs that were also characterized by SEM. Figure 4.7 C shows four single particle scattering spectra from the 237 nm NP sample and the corresponding high magnification SEM images. Both the NP shapes as well as the scattering spectra varied greatly for these NPs. In fact, the scattering intensity at 532 nm changed by about an order or magnitude. Hence, shape inhomogeneity at least for the larger NPs sizes played an important role and contributed to the observed spread in absorption and scattering intensities.

For the NPs with smaller sizes, the shape variation was not as pronounced, consistent with the fact that the single particle spectra showed only small differences in spectral shape. Figure 4.7 D shows the spectra of two gold NPs with nearly identical diameters of 88 (blue symbols) and 87 nm (red symbols.) Based on the theoretical spectra (shown as solid lines), the shift in the resonance maxima of 11 nm was not due to the difference in NP size, but most likely was caused by an inhomogeneous local refractive index of the NP surroundings including the surface.[180] Excess citrate was likely deposited when the NPs were drop cast from the solution and left to dry. However, even a change in the local refractive index from 1.25 to 1.4 results only in a variation of at most 6% for the scattering intensity at 532 nm according to Mie theory and therefore could not be a major factor for the observed intensity variations. While in Figure 4.7 D the calculated spectra have been adjusted to match the amplitudes of the experimental spectra, the inset displays the same spectra without scaling. As expected from the very similar NP size, the difference in calculated scattering intensity is less than 2 %. In contrast, the experimental scattering intensities differ by about a factor of 2 (or 58 %) despite the absence of noticeable changes in NP size, shape, or dielectric environment for these two NPs. Similar observations were also made for NPs from the 51 and 76 nm NP samples.

Based on these results so far, NP shape heterogeneity contributed to the width of the intensity distributions, but it was not the sole factor especially for the smaller NP sizes. We therefore propose that the presence of the support surface gave rise to the fluctuations in the observed absorption and scattering intensities. Recent single particle studies have pointed out that the surface plasmon resonance can strongly depend on the

substrate due to local charge interactions between the plasmon oscillation and image charges created in the substrate.[37,181,193] The fact that the single particle scattering spectra in Figure 4.7 D are broader than the ones predicted by Mie theory is indeed consistent with a charge interaction between the NPs and the glass.[194] In addition, the presence of the substrate breaks the symmetry of the system thereby further amplifying heterogeneities in NP size and shape.[177,195] In ensemble extinction measurements of colloidal NP solutions, the NP orientation with respect to the interacting light is not as important because of averaging over many NP orientations within the detection volume. The UV-vis spectra in Figure 4.3 hence agree well with Mie theory even for the two largest NP sizes.

The explanation that shape heterogeneity and the presence of the substrate are responsible for the observed intensity fluctuations is further supported by photothermal imaging of NPs in different media as well as by correlating scattering intensities from laser dark field imaging and single particle spectroscopy. We tested the effect of the surrounding medium on the intensity distribution for the 88 nm NP sample. In Figure 4.8 intensity distributions are compared for 88 nm NPs supported on glass and surrounded by air (blue) vs. embedded in PVA with glycerol added (red). The width of the latter distribution is significantly smaller with a relative standard deviation of 33% compared to 48% for the NPs in air. Variations in NP shape and the resulting different orientations on the glass coverslip were likely the main contributing factors to the observed difference. In the PVA matrix the heat transfer is expected to be homogeneous independent of the NP orientation, while in the other case the relative surface area that touched the glass mattered as energy loss predominantly occurred between the NPs and the coverslips.

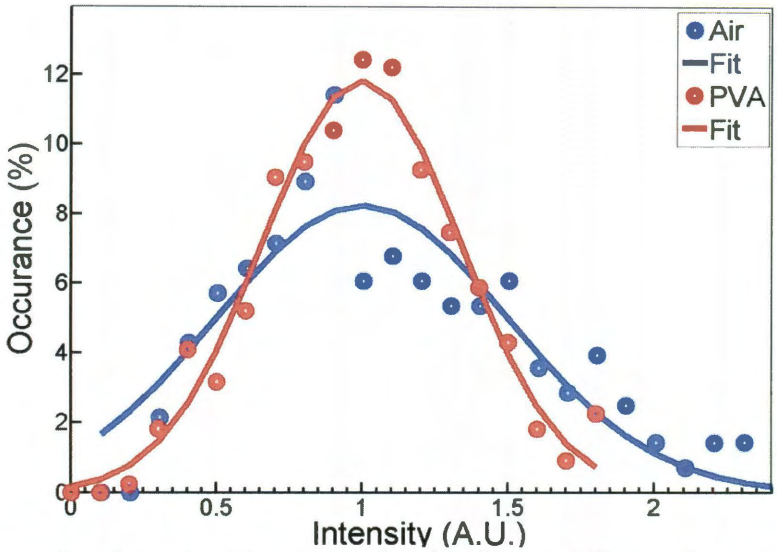

Figure 4.8. Absorption intensity histograms for the 88 nm NP sample under two different experimental conditions. Blue: NPs on glass surrounded by air. Red: NPs embedded in PVA with glycerol added on top of the sample. For ease of comparison, the histograms are centered at 1 and the areas are normalized. Fits to Gaussian curves are shown as solid lines.

Single particle spectra can be used to determine the scattering intensity at 532 nm as well by recording the amplitude of the spectrum at this wavelength. NPs for which both a scattering spectrum and a corresponding intensity value from a laser dark-field image were available were analyzed for the degree of correlation between the scattering intensities at 532 nm. In Figure 4.9 the intensities according to the dark-field images were plotted against the intensities obtained from the scattering spectra for the 88 nm (A) and 237 nm (B) NP samples. The size variations for the NPs included in Figure 4.9 were 5 % and 10 % for the 88 and 237 nm NP samples, respectively. The average uncertainty in determining the scattering intensity from the images and spectra was about 10% as estimated from repeated measurements. It can be concluded that for a relatively small size range the correlation between scattering intensities for the same single NPs but measured by two different methods is low. The absence of a strong correlation was most likely due to a combination of several factors. Excitation geometry together with

different orientations of even slightly anisotropic NPs on the support substrate appears to play an important role in the measured scattering intensity.[177,182,195] The substrate together with the NP shape inhomogeneity led to different orientations of the NPs with respect to the incident light. Also, the illumination geometry was different for the laser dark-field imaging vs. single particle spectroscopy. In laser dark-field imaging the laser light was incident from only one direction, while for the single particle spectra the light from the halogen lamp illuminated the NPs from all in-plane directions as determined by the cone of light formed by the dark-field dichroic and objective. The interaction of the NPs with the incident light was therefore different for these two measurements, further amplified by the deviation from a perfect spherical shape of the NPs sitting on the glass substrate.

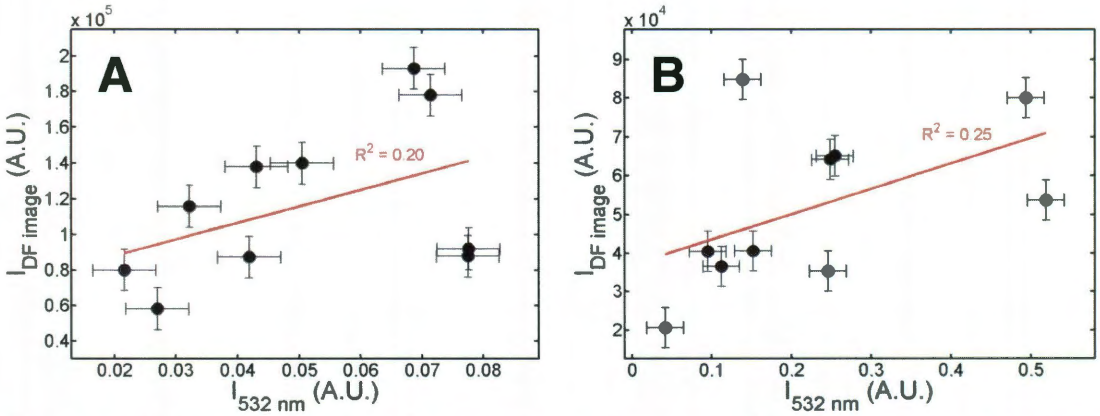

Figure 4.9. Scattering intensity at 532 nm acquired from the dark-field images vs. from the single particle spectra for the same NPs. A – 88 nm NP sample. B - 237 nm NP sample. Each data point represents a NP for which both laser dark-field images and single particle scattering spectra were recorded. The linear fits to the data shown as red lines illustrate only low correlation between the scattering intensities for these two measurements. The range of NP sizes included in (A) is 5% and in (B) 10%. Note that the experimental error of 10% for the scattering intensity is much lower compared to the variation in scattering intensity between the two methods used.

For the 88 nm NP sample we measured two NPs that were significantly bigger with diameters of 112 and 120 nm. If those NPs were included in the analysis, the

correlation between the scattering intensity measured by laser dark-field imaging and single particle spectroscopy greatly improved (Figure 4.10). Differences in NP illumination geometry and incident light polarization are therefore only important for a certain size range. Once the diameter of the NPs changes more significantly, the NP size becomes the most dominating factor in determining the average scattering intensity, which is also consistent with the trends shown in Figure 4.6. Note that there also was no correlation between how much absorption and scattering deviated from the calculated value for the same NP (Figure 4.11).

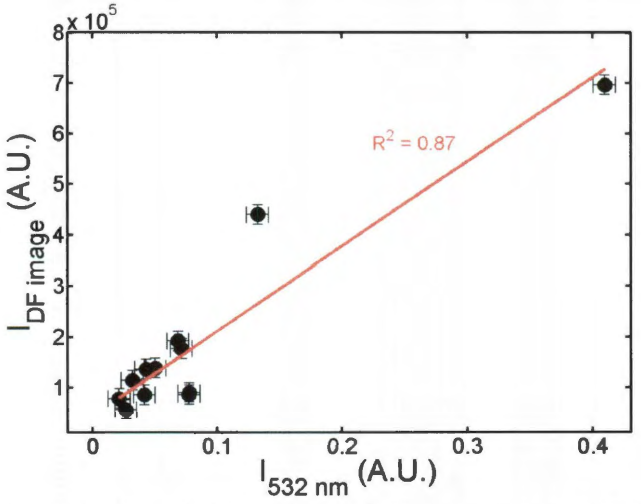

Figure 4.10. Scattering intensity at 532 nm acquired from the dark-field images vs. from the single particle spectra for the 88 nm NP sample. Each data point represents a NP for which both laser dark-field images and single particle scattering spectra were recorded. The data shown here is the same as in Figure 4.9 except that two larger NPs with diameters of 112 and 120 nm were added. The linear fit to the data shown as the red line illustrates a much better correlation between the scattering intensities for these two measurements if a larger size range is considered.

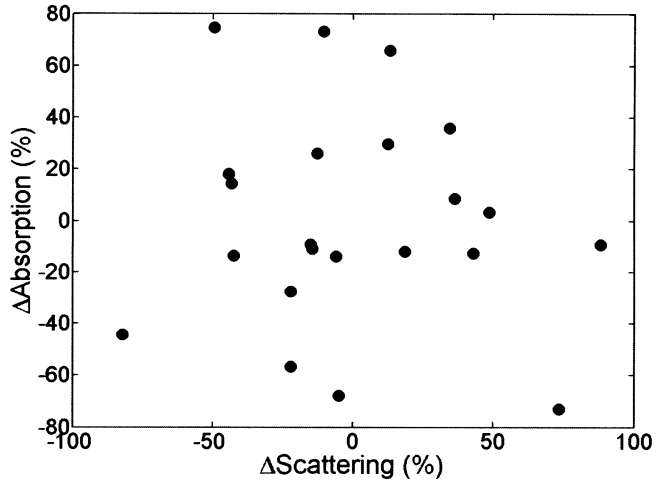

Figure 4.11. Percentage deviation of the absorption intensity from the calculated value using Mie theory plotted against the corresponding percentage deviation of the scattering intensity for the data points of the 88 nm NP sample shown in Figure 4.6. This analysis demonstrates that there is no correlation between how much absorption and scattering deviated from the calculated value for the same NP. For example, some NPs that absorbed more strongly scattered both more or less than expected based on Mie theory. Furthermore, it is important to point out that the percentage deviation is similar for absorption and scattering in agreement with the intensity distributions shown in Figure 4.7A.

4.5 Conclusion

We have investigated the size dependence of the absorption and scattering intensities predicted by Mie theory for spherical gold NPs covering a large range of NP diameters from 43 to 274 nm. Using a combination of dark-field scattering and photothermal imaging together with correlated SEM we were able to separately determine the contributions from surface plasmon absorption and scattering for the same single plasmonic NP, while taking the NP size distribution within each of the five samples studied directly into account and eliminating NP size inhomogeneities. We found good general agreement at 532 nm between Mie theory and the absorption and scattering intensities that were averaged over the distribution of NP diameters for each sample. However, for nanoparticles of similar diameters, absorption and scattering

intensities could differ by as much as 50% under our experimental single particle spectroscopy conditions, causing the width of the intensity distributions to be significantly larger than expected from the nanoparticle size distributions alone. While heterogeneity in NP shape could partially account for the widths of the intensity distributions especially for the largest NPs as shown by single particle scattering spectra and correlated SEM imaging, our results suggest that the primary reasons for the observed intensity variations were the orientations adopted by the not perfectly spherical NPs on the glass substrate as well as their interactions with it. Hence, our results add to the important notion that the presence of an interface needs to be taken into account for applications that involve supported plasmonic NPs. Our findings are important for applications that rely on the absorption and scattering intensities of single NP instead of spectral shifts of the plasmon resonance.

4.6 Acknowledgements

This work was supported by the Nanoscale Science and Engineering Initiative of the National Science Foundation under NSF Award Number EEC-0647452. I would like to thank our group members with whom I collaborated on this project: Ji Won Ha, Sergio Dominguez-Medina and Liane Slaughter. I would also like to acknowledge Dr. Christy Landes for tremendous help preparing this manuscript, Dr. Jason Hafner for insightful discussions, Britain Willingham for providing the source code for the Mie theory calculations, and Saumyakanti Khatua for help with acquiring the single particle spectra.

CHAPTER 5
ONE-PHOTON PLASMON LUMINESCENCE CORRELATION SPECTROSCOPY AS A PROBE FOR ROTATIONAL AND TRANSLATIONAL DYNAMICS OF GOLD NANORODS

5.1 Abstract

A strong intrinsic signal is advantageous over labeling for optical detection of nanoparticles. Intense scattering and absorption by the surface plasmon resonance, which exceeds molecular cross sections, provides a direct method for visualizing noble metal nanoparticles. While two-photon luminescence in gold nanoparticles also yields a strong signal, one-photon luminescence is generally regarded to be much weaker and has seldom been employed for optical nanoparticle detection. In this project we investigated one-photon luminescence of gold nanospheres and nanorods using single particle spectroscopy with excitation at 514 and 633 nm. We characterized the polarization dependence, determined the quantum yield, and present a mechanism describing one-photon luminescence. Our results suggest fast intercorversion between surface plasmons and hot electron-hole pairs and show that the luminescence occurs via emission by a surface plasmon. Using the information obtained from the single particle studies, we were able to successfully employ one-photon luminescence for correlation spectroscopy measurements and to correctly interpret auto- and crosscorrelation functions, which were used to determine the hydrodynamic sizes of several gold nanoparticle samples and to extract rotational dynamics of nanorods. For practical applications of colloidal nanoparticles the questions of mobility and aggregation are of paramount importance. A comparison between luminescence and scattering correlation spectroscopy revealed that one-photon luminescence gives more consistent results for studying diffusion in systems

that are prone to aggregation because luminescence correlation spectroscopy is not as strongly biased by a small percentage of contaminants consisting of larger nanoparticles or aggregates.

5.2 Introduction

Any practical application of nanoparticles (NPs) inevitably involves answering questions about NP mobility and aggregation for the various media in which they will be applied. For example, it is important to understand the diffusion of gold NPs inside cells for their biomedical applications.[154,196,197] There are two general techniques to optically visualize NPs. One is labeling NPs with fluorescent dyes[27,50-52] and the other involves using an intrinsic optical signal, e.g. luminescence, scattering, or absorption[74,76,198-201] For plasmonic NPs, visualization is possible by exploiting their enhanced scattering and absorption cross sections at the plasmon resonance.[60,151,199] Two-photon luminescence is also routinely used for gold NPs.[62-64] On the other hand, while one-photon luminescence in gold NPs has been observed, it is generally much weaker and therefore not commonly used for NP detection.[67-71] Furthermore, the origin of one-photon luminescence remains a subject of debate with proposed mechanisms including plasmon enhanced interband transitions[68] or direct plasmon emission.[67] Moreover, a recent report by Gaiduk *et al.* showed that the fluorescence of spherical gold NPs in organic solvents can be enhanced under strong laser excitation, which was attributed to temperature assisted chemical modifications of the NP surface.[202]

Methods to study NP diffusion include single particle tracking, which works best for diffusion on surfaces or in thin films because NPs drifting out of focus makes the

measurement and analysis difficult or requires complex setups.[40,48,203,204] A different approach is to follow not a single NP, but to monitor changes in signal due to NP diffusion from a small focal volume. This approach, pioneered as fluorescence correlation spectroscopy, offers advantages over bulk measurements because of high spatial resolution – observation volumes are on the order of femtoliters – and the ability to work with low concentrations – nanomolar range.[100,205-207] Small detection volumes have the additional benefit of an improved signal to background ratio, because the background signal is reduced for smaller collection areas.

Besides translational diffusion, NPs in solution also undergo rotational diffusion. For nanorods, the rotational diffusion constant, D_{rot}, is more sensitive to the length, L, and aspect ratio, AR, compared to the translational diffusion constant, D_{tr}. A number of phenomenological descriptions exist for rotational diffusion, but they all share a common functional form of $D_{rot} \sim \frac{1}{L^3}\ln(AR)$, while translational diffusion scales as $D_{tr} \sim \frac{1}{L}\ln(AR)$.[208] To observe rotational NP diffusion, the measured signal has to be anisotropic and intrinsic to the NP, which for nanorods typically means polarized along either or both of the two major axes.

A technique that is capable of simultaneously measuring rotational and translational diffusion in principle offers greater accuracy because it provides two independent manifestations of the NP size. For gold nanorods (AuNRs), it has been shown that scattering,[43,209-211] absorption,[172] and two-photon luminescence[64] are highly polarized and correlate well with the AuNR orientation. Conflicting reports, however, exist for the polarization of the one-photon luminescence from AuNRs, varying from

unpolarized[212] to highly polarized along the long axis of the AuNRs.[68] In addition to a well characterized polarized NP signal, the size scaling of these optical processes need to be considered for inhomogeneous systems. For example, because plasmon scattering scales as the square of the NP volume for NPs smaller than about 100 nm, scattering correlation spectroscopy of plasmonic NPs is very sensitive to the presence of larger and hence brighter NPs and NPs aggregates, potentially biasing the recovered diffusion constants.[74]

Furthermore, ease of experimental implementation is another issue that needs to be considered for high throughput screening of NP sizes in solution. Absorption based approaches such as photothermal correlation spectroscopy[75,76] require the careful adjustment of two laser beams and for NP rotation additional variation of the excitation polarization. Multi-photon luminescence is only possible with more expensive ultrafast lasers.[62,213] Scattering and one-photon luminescence, on the other hand, require relatively simple and inexpensive setups, offer excellent control over polarization, and can be used on the same instrument, which makes them great candidates for correlation spectroscopy.

Despite the potential benefits that extracting the rotational diffusion constant offers to the field of NP rheology, there have been only a handful of studies involving rotational dynamics of NPs. The anisotropic luminescence of semiconductor nanorods was used in correlation spectroscopy measurements to yield rotational and translational diffusion constants.[61] Plasmon scattering has been utilized to track AuNR rotation on substrates by dark-field imaging.[209] One-photon luminescence of plasmonic NPs has been used as well, but to study only the translational diffusion of gold NPs and

AuNRs.[69,70] To the best of our knowledge, the unconstrained rotational dynamics of AuNRs in solution has not been studied yet using correlation spectroscopy.

Here we show how luminescence correlation spectroscopy fares against scattering correlation spectroscopy, provide results for rotational and translational diffusion of different sizes of AuNRs in aqueous solution, describe the conditions that worked best, and offer an insight into the nature of the one-photon luminescence of gold NPs. We found that it is very important to understand the polarization anisotropy of the one-photon luminescence in AuNRs in order to correctly interpret our results. This was best accomplished using single particle spectroscopy.

5.3 Materials and methods

5.3.1 Correlation spectroscopy analysis

Correlation spectroscopy relies on intensity fluctuations within an observation volume to determine the diffusion constant and hydrodynamic radius of molecules or NPs.[83,207,214] Both scattering and luminescence can be used for correlation spectroscopy and intensity autocorrelation analysis is most commonly applied.[60,74] Assuming the presence of only one analyte of interest in the sample, a Gaussian beam-shaped observation volume, and only translational diffusion, the autocorrelation, G_D, as a function of lag time, τ, can be expressed in terms of the observation volume parameters – volume, V_{eff}, beam waist, r_0, and beam height, Z_z – mean transient time through the detection volume, τ_D, and analyte concentration, $< C >$:[78,133]

Equation 5.1

$$G_D(\tau) = \frac{1}{V_{eff} < C >} \cdot \frac{1}{\left(1 + \frac{\tau}{\tau_D}\right)} \cdot \frac{1}{\left(1 + \left(\frac{r_0}{z_0}\right)^2 \left(\frac{\tau}{\tau_D}\right)\right)^{1/2}}$$

The mean transient time, τ_D, is in turn related to the translational diffusion constant, D_{tr}, according to:[78,133]

$$\tau_D = \frac{r_0^2}{4D_{tr}}$$ **Equation 5.2**

The hydrodynamic radius, R_h, is then obtained through the Stokes-Einstein relationship:[215]

$$D_{tr} = \frac{k_B T}{6\pi\kappa R_h}$$ **Equation 5.3**

k_B is the Boltzmann constant, T the temperature, and κ the solvent viscosity. The hydrodynamic radius recovered following this analysis yields an average size for the NPs present in the solution. If the NP brightness, i.e. scattering or luminescence intensity, depends on the NP size, then the contribution to the autocorrelation, $G_i(\tau)$, from each species having a different size is weighted by its concentration, $< C_i >$ and brightness, η_i:[101]

$$G(\tau) = \frac{\sum \eta_i^2 < C_i >^2 G_i(\tau)}{\left(\sum \eta_i < C_i >\right)^2}$$ **Equation 5.4**

Deriving the equation to describe the rotational component of the autocorrelation function is more complex involving several assumptions about the relative timescales of the intrinsic signal decay and rotational relaxation, the geometry of the setup, and the relative orientations of the absorption and emission dipoles. Aragon and Pecora[205] and

later Kask *et al.*[216] developed a model describing the rotational component of the autocorrelation function for correlation spectroscopy experiments assuming rigid particles with collinear absorption and emission dipoles. Based on this model, the rotational autocorrelation function for a perfect dipole, G_R, is given by:[216]

$$G_R(\tau) = \sum_l B_l(\hat{a},\hat{e}_1,\hat{e}_2)\exp[-l(l+1)D_{rot}\tau] \qquad \textbf{Equation 5.5}$$

D_{rot} is the rotational diffusion constant, l is the index of the angular momentum eigenvalue and can take values of 0, 2 and 4. $B_l(\hat{a},\hat{e}_1,\hat{e}_2)$ are the coefficients calculated for different relative orientations of excitation polarization, $\hat{a}$, and two detection polarizations, $\hat{e}_1$ and $\hat{e}_2$. For the autocorrelation function, the signal from a single detector is used and the detection polarizations are the same. For the crosscorrelation function, the polarization of $\hat{e}_1$ and $\hat{e}_2$ can be different. Following the convention used by Tsay *et al.*,[61] we considered three configurations: two autocorrelations with detection polarization parallel and orthogonal to the excitation polarization (XXX and XYY where the first letter denotes the excitation polarization) and one crosscorrelation of the signal from the two detectors (XXY). Crosscorrelation curves can be calculated as either XXY or XYX, but in all of our experiments XXY and XYX looked identical and we therefore show only data for XXY.

It was shown that the rotational component can be reduced to a single exponential when a high numerical aperture (NA) objective is used, as is the case in our setup, which employed a 1.3 NA objective.[61,217] For our experimental data we compared fits to single and multiple exponentials and found that single exponential fits were more consistent.

To relate rotational diffusion constants recovered from correlation spectroscopy measurements to the size of the NPs we used the model by Tirado *et al.*[208] derived for

short cylinders, which has been shown to describe rotational and translational diffusion of rods accurately:[61]

Equation 5.6

$$D_{rot} = \frac{3k_BT}{\pi\kappa L^3}\left[\ln\left(\frac{L}{d}\right) + \sigma\right]$$

Equation 5.7

$$D_{tr} = \frac{k_BT}{3\pi\kappa L}\left[\ln\left(\frac{L}{d}\right) + \nu\right]$$

Here, L and d are the rod length and diameter, respectively, with σ and ν given by

$\sigma = -0.662 + 0.917\,{}^{d}\!/_{L} - 0.05\left({}^{d}\!/_{L}\right)^2$ and $\nu = 0.312 + 0.565\,{}^{d}\!/_{L} - 0.1\left({}^{d}\!/_{L}\right)^2$.

By equating Equation 5.3 and Equation 5.7 the relationship between the rod dimensions and the hydrodynamic radius can be extracted according to:

Equation 5.8

$$R_h = \frac{L}{2\ln\left(\frac{L}{d}\right) + \nu}$$

The overall equation for the autocorrelation function including rotational and translational terms is then given by:[61,216]

Equation 5.9

$$G(\tau) = G_D(\tau)G_R(\tau) = \frac{1}{V_{eff} < C >} \cdot \frac{1}{\left(1 + \frac{\tau}{\tau_D}\right)} \cdot \frac{1}{\left(1 + \left(\frac{r_0}{z_0}\right)^2\left(\frac{\tau}{\tau_D}\right)\right)^{1/2}} \cdot (1 + A \cdot B_l \cdot \exp(-6D_{rot}\tau)$$

The parameter A is introduced to account for the anisotropy of a real system, which can be different from 1. The same equations given above also apply to crosscorrelation

measurements with more than one detector and can be used for both scattering and luminescence correlation spectroscopy experiments.[218]

5.3.2 Correlation spectroscopy setup

Correlation spectroscopy experiments were performed on a home-built instrument based on an inverted Zeiss microscope described elsewhere.[27,83] Excitation was carried out using the 514 nm line of an Ar^+ laser (Modu-Laser) and a 633 nm He-Ne laser (JSD Uniphase). The lasers were focused more than 3 μm deep inside the sample chamber to avoid sampling NP diffusion at the interface and to minimize reflected light from the glass coverslips. For luminescence correlation spectroscopy experiments, light collected from the sample was passed through a dichroic mirror and a notch filter (z532rdc, Chroma Technology, and RNF-514.5, CVI, for 514 nm excitation and z633rdc, Chroma Technology, and RNF-632.8, CVI, for 633 nm excitation), which were used to assure that all excitation light was removed from the signal. No other filters were used and therefore spectrally integrated intensities were collected for the luminescence correlation measurements. To switch from luminescence to scattering correlation spectroscopy, the dichroic mirror was switched to a 50/50 beam splitter and the notch filter was removed. Sample preparation for correlation measurements was carried out according to the procedure published earlier.[83]

To avoid effects of optical trapping or detector saturation, we performed a power dependence study independently for the scattering and luminescence correlation spectroscopy experiments to find the appropriate range of laser powers, where the recovered NP sizes did not depend on the excitation power. The luminescence was found

to be a much weaker signal compared to scattering and therefore powers used for luminescence correlation spectroscopy were orders of magnitude higher: ~15 kW/cm^2 for luminescence correlation spectroscopy and ~15 W/cm^2 for scattering correlation spectroscopy.

Calibration with particles of known size is necessary to correctly determine the observation volume parameters in Equation 5.1.[27,83] We used a solution of 100 nm fluorescent polystyrene beads, purchased from Invitrogen, to calibrate the instrument before each scattering and luminescence measurement. Pure solvent samples were measured using similar excitation powers to make sure that the signal originates only from the NPs in question. Each sample was measured at least 3 independent times to yield mean values and corresponding errors.

5.3.3 Polarization geometry

The samples were excited with linearly polarized light and two avalanche photodiode detectors (PerkinElmer) were set up to collect light polarized parallel and perpendicular to the excitation polarization. The propagation direction of the laser light was set along the z-axis and the x-axis was chosen to be parallel to the excitation polarization. The two detectors were then set up to collect light polarized along the x- and y-axis. The autocorrelation curves were calculated using data from either of the detectors – XXX or XYY, where the latter configuration refers to collecting light that is polarized orthogonally to the excitation. Crosscorrelation curves were calculated using data from both detectors (XXY).

5.3.4 Single particle spectroscopy

Single particle spectra were acquired using the same instrument described above. For scattering spectra, a halogen lamp was used for excitation in a dark-field geometry and the scattered light was redirected to a spectrometer equipped with a CCD camera (Princeton Instruments PIXIS 400BR). For luminescence spectra, the same laser lines were used for excitation as for the correlation spectroscopy experiments and the luminescence collected in an epi-illumination geometry was sent to the same spectrometer. As needed, specific polarizations of the incident and emitted light were controlled by half wave plates and placing polarizers in the detection light path. A 100X Zeiss Epiplan objective was used to collect all spectra. Correlation between single particle spectra and the dimensions of the NPs was accomplished using a patterned substrate for identification in the optical setup and a scanning electron microscope (SEM, model: FEI Quanta 400 ESEM FEG) as previously described in detail.[2,39]

5.3.5 Luminescence characterization

It was also necessary to confirm that collected luminescence photons were real and not due to stray scattered light because luminescence at the NP plasmon frequency has been shown to have a very low efficiency of 10^{-6}.[212] Dichroic mirrors and notch filters were placed in the detection beam path to block out any scattered excitation light, but to further verify that the recorded signal was indeed due to luminescence, we measured polarized luminescence spectra for all excitation wavelengths used. Because of the high excitation rate and short life time enough signal could be collected, when using a laser excitation source. On the other hand, we could not observe luminescence in bulk

measurements with lamp excitation. Further details about the luminescence characterization are discussed below.

5.3.6 Nanoparticle characterization

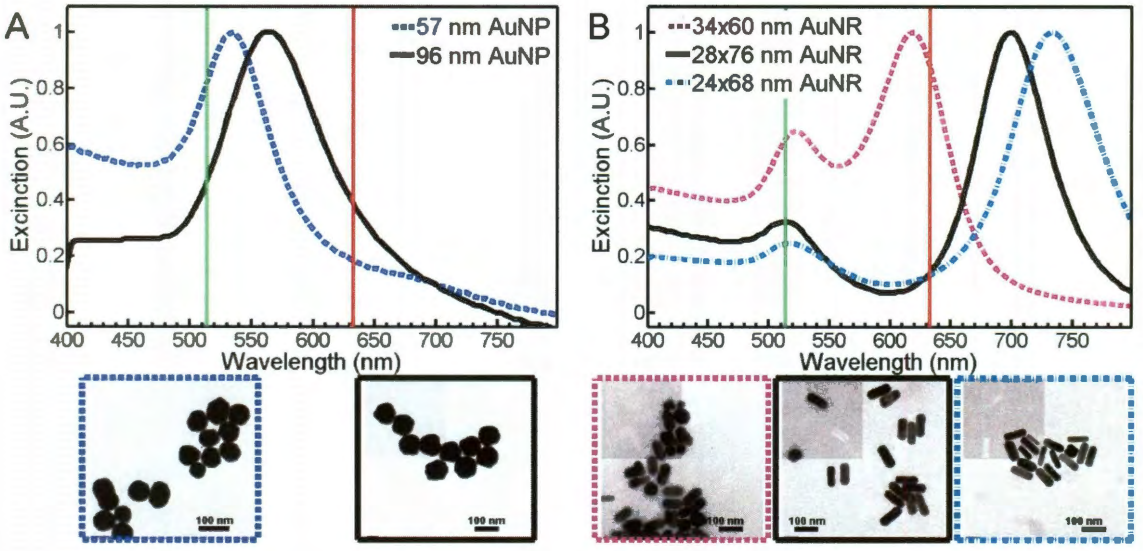

Figure 5.1. UV-Vis spectra and TEM images for (A) AuNP samples and (B) AuNR samples used in this study. Vertical lines denote the two excitation wavelengths that we used: 514 nm (green) and 633 nm (red). Representative TEM images for each sample are also included.

Spherical gold NPs (AuNP) and AuNRs were purchased from Nanopartz and characterized with bulk UV-Vis spectroscopy (Shimadzu UV-3101PC) and transmission electron microscopy (JEOL 2010 TEM), as shown in Figure 5.1. This allowed us to quantify the extent of size and shape heterogeneity of these AuNP and AuNR samples. The UV-Vis spectra in Figure 5.1A show single plasmon peaks for the 57 nm (dashed blue line) and 96 nm (solid black line) AuNPs at 535 and 564 nm, respectively. The AuNRs in Figure 5.1B exhibit two well-defined plasmon peaks in their extinction spectra. The resonance near 520 nm has contributions from both interband transitions and the transverse plasmon. The spectral position of the longitudinal plasmon resonance depends

mainly on the aspect ratio of the AuNRs for this particular size regime.[8,219] The maximum of the longitudinal plasmon resonance is at 620 nm for the 34x60 nm AuNR sample (dashed purple line), at 700 nm for the 28x76 nm AuNR sample (solid black line), and at 735 nm for the 24x68 nm AuNR sample (dashed blue line). The samples are labeled according to their mean dimensions. Representative TEM images for these samples are given in Figure 5.1 as well, while the analysis of the size distributions for each sample is provided in Figure 5.2.

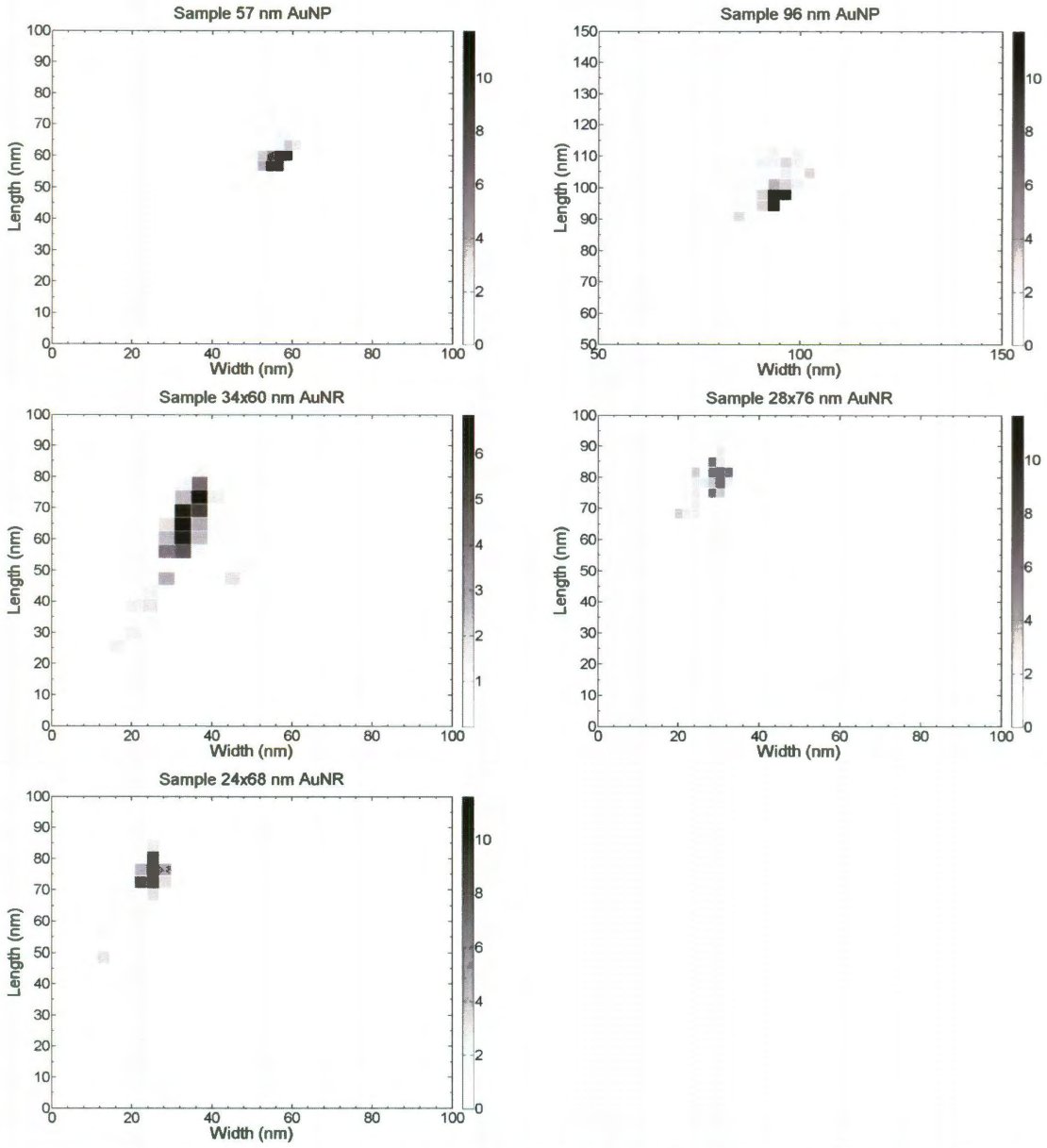

Figure 5.2. Size distributions of all samples used in this study based on TEM images. TEM images were taken with a JEOL TEM 2010 using a magnification of 30,000 – 50,000X. Individual histograms contain at least 150 particles. Each particle was measured along two dimensions and the shortest was arbitrarily assigned as the width, while the longest was assigned as the length. Uncertainty in the measurement of a particular dimension was on the order of 2 nm based on the resolution of the images. All histograms are normalized and color scales are in percent. From the histograms it is clear that a significant size distribution is present for all samples.

5.4 Results and discussion

In performing a correlation analysis on a NP sample, one of the most important considerations is the effect of sample heterogeneity on the extracted sizes, as shown in earlier work.[46,83] No NP sample is ever perfectly homogeneous. The TEM images given in Figure 5.1 clearly show both that the AuNP samples contain NPs that are not spherical, and that the AuNR samples include NPs with other shapes including spheres (see also Figure 5.2). The question is whether scattering and fluorescence correlation spectroscopy suffer equally from the effects of sample inhomogeneity, or whether there is an advantage of one technique over the other.

Scattering and luminescence of AuNPs and AuNRs can both be used to study rotational dynamics. As compared in Figure 5.3, scattering and luminescence produce very similar autocorrelation curves for the AuNP and AuNR samples used in the present study. The insets of Figure 5.3A and Figure 5.3C depict the size distributions for each sample, as determined from TEM. Scattering and luminescence experiments are shown at two excitation wavelengths (514 nm and 633 nm) for the AuNR sample, but only at 514 nm for the AuNP sample, because of a lack of signal for 633 nm excitation, as expected from the spectra in Figure 5.1. As shown in the inset of Figure 5.3B, the luminescence intensity scales linearly with laser power, which confirms a one-photon excitation process. It should also be noted that the luminescence from the AuNPs and AuNRs does not show any signs of intensity blinking, which is illustrated in Figure 5.4.

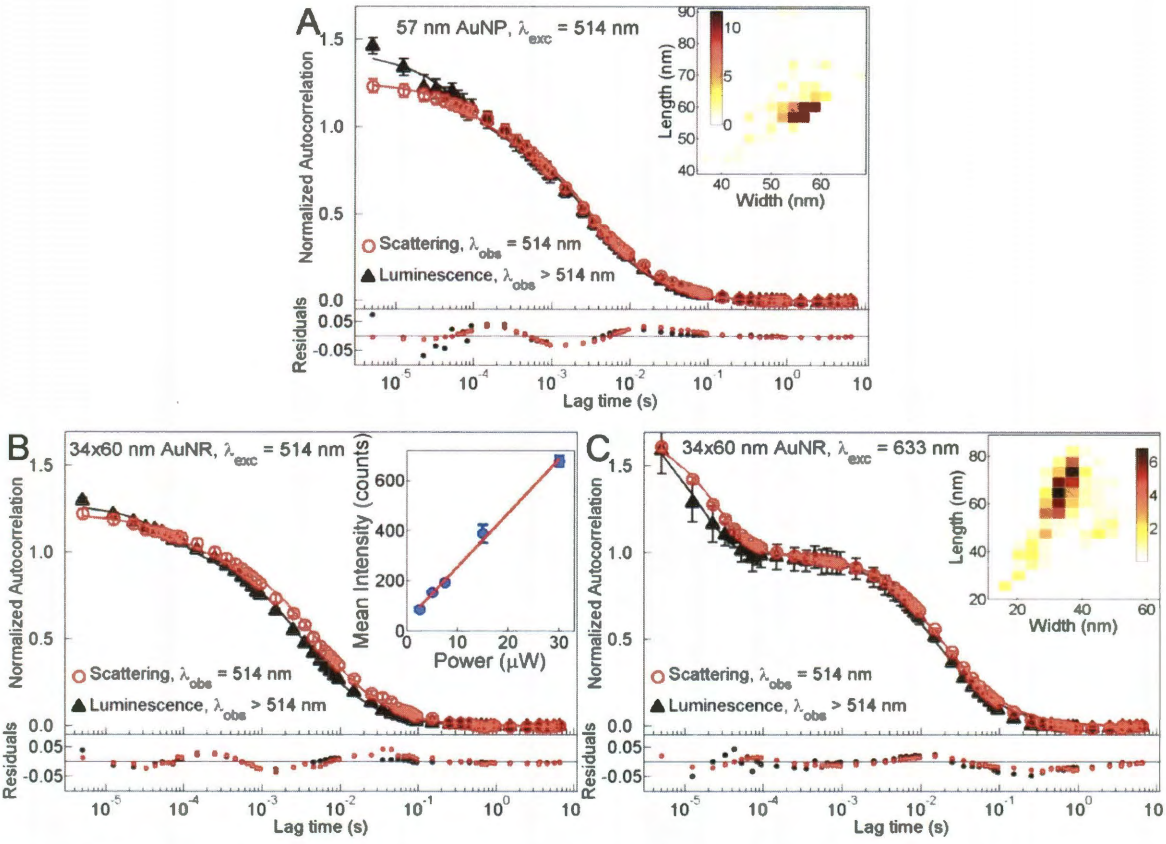

Figure 5.3. Autocorrelation curves from luminescence (black triangles) and scattering (red circles) for 57 nm AuNPs with 514 nm excitation (A), 34x60 nm AuNRs with 514 nm excitation (B), and 34x60 nm AuNRs with 633 nm excitation (C). A rotational component is present in all three cases. The luminescence intensity as determined from the raw time transients scales linearly with the excitation power, shown in the inset of (B), which indicates a one-photon process. Size distributions for the 57 nm AuNP and the 34x60 nm AuNR samples are shown in insets of (A) and (C), respectively.

Scattering and luminescence correlation spectroscopy produce two-component autocorrelation curves. The longer component is attributed to translational diffusion, because the values extracted for the hydrodynamic radii correspond well to those obtained from TEM analysis, as discussed further below. It is important to distinguish between size heterogeneity, photophysical processes such as blinking, or rotational dynamics as the physical origin of the faster component.[220] To do this, we can compare the relative amplitudes of the fast component for the AuNR sample when excited at the

transverse or longitudinal plasmon resonance. As is clearly shown in Figure 5.3C compared to Figure 5.3B, the fast component has a much greater contribution to the autocorrelation intensity decay when the AuNR sample is excited at the longitudinal plasmon resonance. This suggests that the faster component is largely due to the rotational diffusion, because the anisotropy of the longitudinal plasmon is higher than that of the transverse plasmon.[172] The fact that a small fast component is observed also for the AuNP sample, as shown in Figure 5.3A, can be attributed to deviations from a perfectly spherical particle shape. However, additional small contributions due to intrinsic photophysical processes, effects of the capping material, and/or size heterogeneity cannot be completely discounted. These results, along with previous reports of rotational dynamics of NPs,[40,221] provide strong evidence that it is possible to use rotational diffusion analysis to characterize AuNP and AuNR transport in solution.

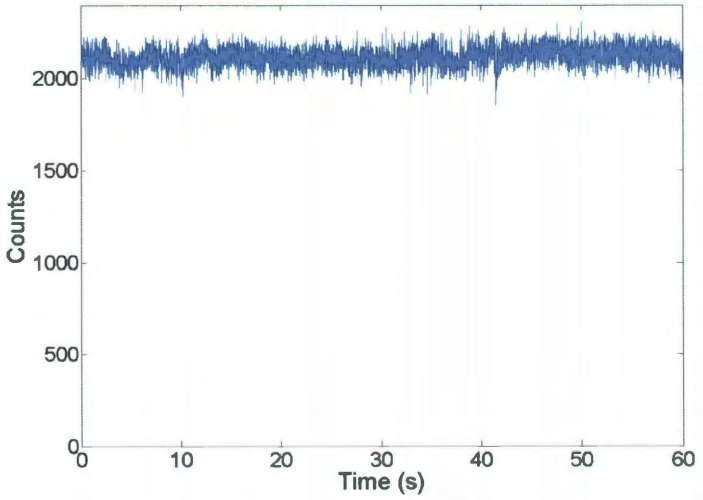

Figure 5.4. Luminescence transient of a single AuNR immobilized on a glass coverslip. The luminescence signal is stable for minutes. The luminescence intensity of the AuNR clearly shows no blinking or photobleaching, which allows us to collect enough photons for luminescence correlation spectroscopy despite a low quantum yield.

To examine how well a quantitative analysis of the rotational and translational diffusion works, it is useful to compare the AuNP and AuNR sizes extracted from scattering and luminescence correlation spectroscopy with those obtained from TEM analysis. This is illustrated in Figure 5.5, in which recovered average sizes from each method are compared, along with the spread in values collected, at the two excitation wavelengths. In order to show all measurements on the same graph, the results are presented as relative deviations from the expected values based on the NP sizes determined by TEM. The beige rectangles in Figure 5.5 illustrate the spread of one standard deviation for the hydrodynamic radii calculated using the TEM size distributions (Figure 5.2) and the equations given in the experimental section. To compare all NP samples on the same scale the mean sizes based on the TEM analysis are set to zero and the percentage deviations are shown. The error bars for the correlation spectroscopy data correspond to the standard deviation of at least 3 independent measurements. It should be noted that the hydrodynamic radius also includes the organic capping material stabilizing these colloidal NPs, which is not included though in the values calculated from the TEM analysis. The cetyltrimethylammonium bromide (CTAB) coating for the AuNRs has previously been determined to be 1-3 nm.[41,42] While our correlation spectroscopy results are certainly consistent with this value, the associated error did not allow for an independent quantitative analysis of the CTAB thickness. However, in general we find very good agreement between the average hydrodynamic radii obtained by the different correlation spectroscopy measurements and the sizes determined by TEM. The origin of the error in determining the hydrodynamic radius from correlation spectroscopy as well as the fact that the error appears to vary between methods

(scattering vs. luminescence and 514 vs. 633 nm excitation) will be discussed in more detail next.

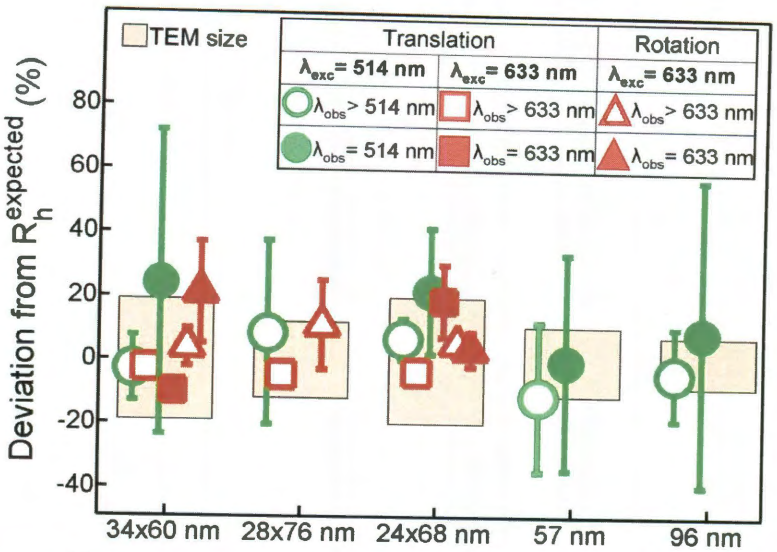

Figure 5.5. Recovered hydrodynamic radii R_h for the 5 different samples used in this study are shown as deviations from the values that are expected based on the TEM measurements. Data for scattering correlation spectroscopy ($\lambda_{obs} = \lambda_{exc}$) are shown as solid symbols; luminescence correlation spectroscopy ($\lambda_{obs} > \lambda_{exc}$) results are given by the open symbols. Green and red colors refer to 514 and 633 nm excitation, respectively. Values recovered from rotational components of the autocorrelation curves are shown as triangles. The size heterogeneity as determined by TEM is indicated by the beige rectangles.

As shown in Figure 5.5, and as reported previously,[27,83] sample size heterogeneity affects the result of correlation spectroscopy measurements. This is observed as a broad spread in extracted sizes. However, as is also shown in Figure 5.5, by careful selection of experimental conditions, the effects of size heterogeneity can be mitigated. In particular for the AuNR samples, 633 nm excitation leads to lower uncertainties in recovered values as compared to 514 nm excitation. Two factors possibly lead to this difference. The first is the fact that at 514 nm almost all NPs present in these samples have a plasmon resonance and therefore all of them will contribute to the recovered value. Only the AuNRs produce enough signal to be detected for photoselective excitation with 633 nm. The second factor is that the amplitude of the rotational component is larger for 633 nm

compared to 514 nm excitation. Therefore the rotational and translational components can be better separated by the fitting algorithm, making the recovered sizes more accurate. From comparing Equation 5.1 and Equation 5.5 it is evident that the translational diffusion constant relies only on the calibration of the focal volume parameters, whereas the rotational component requires assumptions about the geometry of the sample and the setup, but is independent of the calibration parameters. Likewise, assumptions about the rotational diffusion model do not affect the translational component. Therefore combining the results from the two measurements allows us to perform a consistency check and improve the reliability of the measured values. In addition, recovering similar sizes from the rotational and translational diffusion constants independently justifies any assumptions made in the data analysis.

We can obtain further information from the data shown in Figure 5.5. In nearly all samples studied, we observed that the NP sizes and standard deviations recovered using scattering correlation spectroscopy are larger than those extracted using luminescence correlation spectroscopy. A possible explanation is that the presence of larger NPs influences scattering correlation spectroscopy measurements more severely because the scattering intensity scales more strongly with NP size. There is little known about how luminescence depends on NP size, or the effect of the presence of larger NPs on the resulting autocorrelation function. Therefore we decided to compare the results from scattering and luminescence correlation spectroscopy for a mixture comprised of 98% 57 nm and 2% 96 nm AuNPs (Figure 5.6).

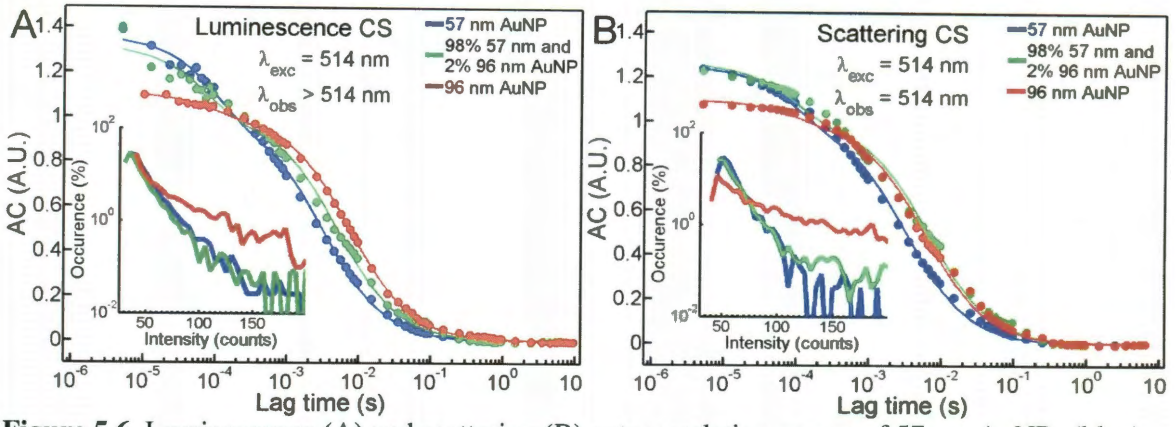

Figure 5.6. Luminescence (A) and scattering (B) autocorrelation curves of 57 nm AuNPs (blue), 96 nm AuNPs (red), and their mixture (green), consisting of 98% 57 nm and 2% 96 nm AuNPs. Insets show intensity histograms for each sample.

As Figure 5.6 shows, we found that luminescence correlation spectroscopy is not as strongly influenced by the presence of low concentrations of larger NPs, as compared to scattering correlation spectroscopy, although size heterogeneity still complicates the recovery of correct hydrodynamic radii because of the size dependent NP brightness. Scattering and absorption cross sections strongly depend on NP size and shape.[2,73,222] Therefore NP size and shape heterogeneity lead to a distribution of signal intensity for scattering and luminescence, biasing the recovered hydrodynamic radii towards larger sizes in all correlation spectroscopy experiments.[83] Luminescence (Figure 5.6A) and scattering (Figure 5.6B) correlation spectroscopy was carried out on the 57 and 96 nm AuNPs as well as a mixture of these two samples. Strikingly, the mixture of 57 and 96 nm AuNPs looks indistinguishable from the pure 96 nm AuNPs for the scattering experiments. In contrast, the size recovered for the mixture using luminescence correlation spectroscopy falls in between 57 and 96 nm, therefore indicating that larger AuNPs do not completely overwhelm the signal from the 57 nm AuNPs. Based on this data we can conclude that luminescence correlation spectroscopy is advantageous over

scattering correlation spectroscopy because the former is not as strongly affected by the presence of a small percentage of aggregates or larger NPs.

In Chapter 2 it was shown that burst intensity frequency analysis (BIFA) of the signal transients is a powerful way to gain more insight into the composition of NP mixtures.[27] Intensity histograms constructed by BIFA are shown in the insets of Figure 5.6A and Figure 5.6B. For both luminescence (Figure 5.6A inset) and scattering (Figure 5.6B inset) the intensity histograms of the pure AuNP samples are clearly different from each other. Average blip intensities for pure 57 and 96 nm AuNPs are 48±1 and 75±3 respectively for luminescence and 58±1 and 140±20 for scattering. On the other hand, the intensity histogram of the mixture is virtually indistinguishable from that of the 57 nm AuNPs, which is in agreement with the very small percentage of 96 nm AuNPs present in the mixture.

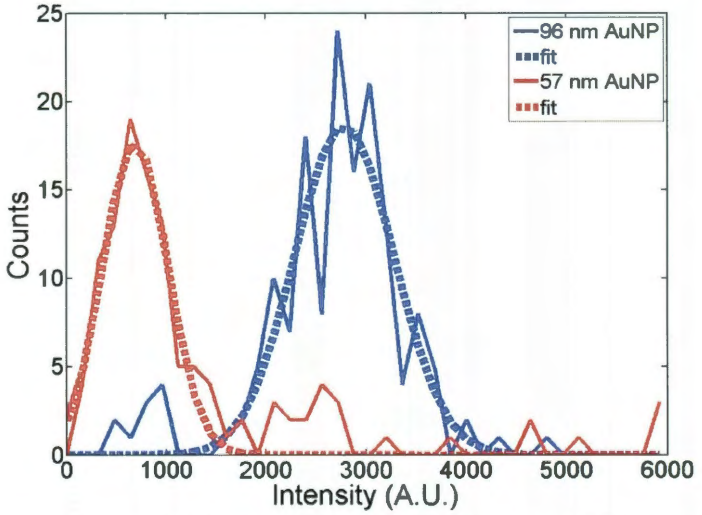

Figure 5.7. Luminescence intensity histograms for 57 nm (red) and 96 nm (blue) AuNPs deposited on a glass coverslip. The intensity histograms were determined from luminescence images recorded with 514 nm excitation using an automated algorithm described in Chapter 2.[2] Average values were determined by fitting a single Gaussian function to the histogram. For the 57 nm AuNPs the average intensity is 690 and for the 96 nm AuNPs it is 2780.

We can further determine, using intensity analysis of single NP images,[2] that the luminescence intensity scales with size similarly to the absorption cross section of the NPs. Based on Mie theory[161] and our previous work described in Chapter 4 on the scattering intensity of individual AuNPs,[2] the average scattering intensity of the 96 nm AuNPs is 12 times higher than that of the 57 nm AuNPs. The absorption cross section varies by only 2.5 times between the 57 and 96 nm AuNPs. Measurements of the luminescence intensities show that the 96 nm AuNPs are on average ~4 times brighter than the 57 nm AuNPs (Figure 5.7). We therefore hypothesize that the luminescence intensity scales according to the absorption cross section. Because having only two data points cannot yield robust conclusions about the nature of the size scaling, further experiments covering a larger range of AuNP sizes will be necessary. However, the data in Figure 5.6 and Figure 5.7 give a clear trend that the dependence of the luminescence intensity on NP size is smaller compared to plasmon scattering.

So far, the rotational and translational dynamics of AuNPs and AuNRs were discussed. We determined that 633 nm excitation is advantageous for correlation spectroscopy studies of AuNRs; rotational diffusion offers an additional very sensitive tool for determining hydrodynamic radii of AuNRs; and that luminescence is preferred compared to scattering for correlation spectroscopy. The most consistent results were achieved for AuNRs with luminescence correlation spectroscopy using 633 nm excitation. We also observed that scattering and luminescence autocorrelation curves seem to follow each other very closely in terms of relative amplitudes of rotational and translational components.

The fact that scattering and luminescence yield the same amplitudes in Figure 5.3 and we get better results with luminescence correlation spectroscopy at 633 vs. 514 nm excitation is rather odd though if we take a closer look. As mentioned already briefly, the drop in amplitude of the rotational component is expected for both scattering and lunminescence correlation spectroscopy when changing the excitation wavelength from 633 to 514 nm, considering that with 633 nm laser light only AuNRs are selectively excited. Previous work on imaging of single AuNRs has also shown that the anisotropy is lower for the excitation at the transverse compared to the longitudinal plasmon resonance due to overlapping interband transitions.[172,223,224] For scattering, however, interband absorptions should be contributing to the depolarization of the signal to a much smaller degree. Furthermore, luminescence in molecular systems predominantly occurs from the lowest excited state independent of the excitation wavelength,[225] suggesting that excitation at 514 and 633 nm should result in similar emission properties including polarization anisotropies.

Only a few studies on the photoluminescence of AuNPs exist,[64,65,67,68,187,202,212,226] and the mechanism is still rather poorly understood. However, two general explanations have been proposed. One mechanism hypothesizes that the luminescence is due to interband electron-hole pair recombination, which is enhanced by the spectrally overlapping plasmon field.[68,212] The other explanation is that the luminescence is caused by direct emission of a plasmon.[67] We then can expect very different polarization dependencies for the luminescence: depolarized emission for interband electron-hole pair recombination and polarized along the plasmon oscillation for direct plasmon emission. Therefore we decided to investigate the nature of the luminescence in more detail using a

correlation spectroscopy setup, described in the experimental section, with two orthogonally polarized detectors so that it was possible to study the signal from each of the detectors as well the crosscorrelation between them.

The autocorrelation (XXX and XYY) and crosscorrelation (XXY) curves for the 34x60 nm AuNR sample are shown in Figure 5.8A and B, for 633 nm scattering and luminescence, respectively, and in Figure 5.8C and D, for 514 nm scattering and luminescence, respectively. All curves are normalized so that the amplitude of the translational component is 1. The component at smaller lag times in all curves corresponds to the rotational diffusion of the AuNRs. The auto- and crosscorrelation traces (symbols) for 633 nm excitation perfectly follow the theoretically predicted trends (dashed lines of matching colors) for a perfect dipole. The average recovered value for the anisotropy is ~0.95 for both scattering and luminescence consistent with a single dipole behavior. The model describes the data extremely well: the autocorrelation for the detector monitoring polarization parallel to the excitation (XXX, red circles) has the largest amplitude; the autocorrelation for the other detector (XYY, black triangles) and the crosscorrelation (XXY, blue crosses) coincide with each other as well as the theoretical curve.

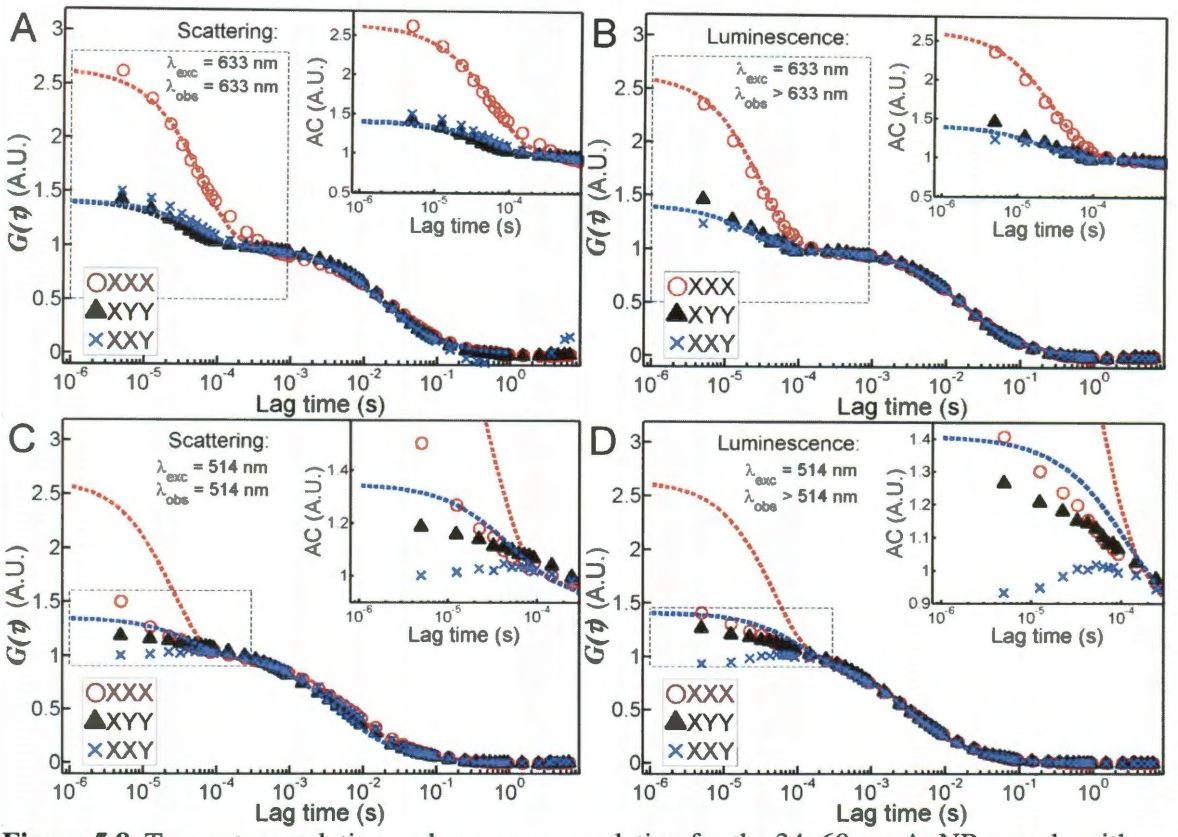

Figure 5.8. Two autocorrelation and one crosscorrelation for the 34x60 nm AuNR sample with 514 and 633 nm excitation. The 1st letter of the legend denotes the excitation polarization, 2nd and 3rd letters stand for the detection polarizations (see experimental section for more details). (A) and (B) show scattering and luminescence correlation curves, respectively, at 633 nm. Experimental data are given by symbols and theoretically expected trends for a perfect dipole are shown as dashed lines. (C) and (D) show scattering and luminescence correlation curves, respectively, at 514 nm. For this excitation wavelength, however, experimental data do not follow the theoretical trends for a perfect dipole, shown as dashed lines, and moreover scattering and luminescence data are no longer the same. Also note that the luminescence crosscorrelation curve has a significant rising edge at short lag times.

Experimental data, shown in Figure 5.8C, for scattering correlation spectroscopy with 514 nm excitation cannot be described by the model of Kask *et al.*[216] even if a variable anisotropy term is introduced as suggested by Tsay *et al.*[61] Fitting of the two autocorrelation curves gave recovered anisotropy values that are different from each other: 0.3 and 0.6 respectively for XXX (red circles) and XYY (black triangles). Theoretically expected auto- and crosscorrelation curves for a perfect dipole are shown as dashed lines of the corresponding color to emphasize the difference compared to the

results for 633 nm excitation. It is also important to note that the fits to the autocorrelation curves in Figure 5.8C are good, as further illustrated in Figure 5.9 and that an erroneous conclusion could have been made about the anisotropy at 514 nm if each detector were considered separately. We therefore hypothesize that Equation 5.5 fails to correctly describe the data because of the cylindrical symmetry of the transverse plasmon mode, which is different from a molecular dipole that is assumed in the derivation of Equation 5.5.

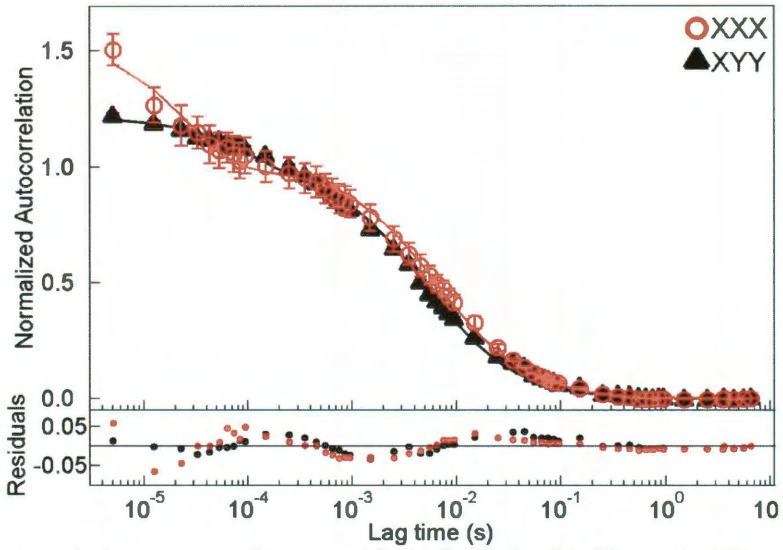

Figure 5.9. Autocorrelation curves of scattered light from the 34x60 nm AuNR sample collected by two detectors with different geometries for the collected polarization – XXX, red open circles, and XYY, black solid triangles. The quality of the fits is surprisingly good, given the size distribution of the sample, see Figure 5.2. If autocorrelation curves are considered independently, then anisotropy values of 0.3 and 0.6 are recovered for XXX and XYY, respectively. Such mismatch in recovered values cannot be explained by the uncertainty in the data and therefore supports our conclusion that the model fails to describe the system when 514 nm excitation light is used.

The luminescence crosscorrelation for 514 nm excitation suggests that the absorption and emission dipoles are not collinear. Similarly to the scattering data, the two autocorrelations produce different values for the anisotropy. But unlike the scattering crosscorrelation (XXY in Figure 5.8C), crosscorrelation of the luminescence

resulted in a crosscorrelation intensity that initially rises (XXY in Figure 5.8D). A rise is expected if the absorption and emission dipoles of the AuNRs are not collinear for 514 nm excitation. If the directions of the absorption and emission dipoles are different, then a major assumption in the model of Aragon and Pecora[205] and Kask *et al.*[216] is no longer valid and the coefficients $B_l(\hat{a},\hat{e}_1,\hat{e}_2)$ in Equation 5.5 can become negative, leading to an initial intensity increase for the rotational component. Thus, we decided to check the collinearity of the absorption and emission dipole moments using single particle spectroscopy as discussed below.

Before proceeding to measure the orientations of the absorption and emission dipoles, it is important to understand the nature of the luminescence, which can be accomplished by recording single particle spectra. For single particle studies, AuNPs and AuNRs were deposited on glass coverslips, which lowered the effective refractive index of the medium. Therefore the 24x68 nm AuNR sample with a higher aspect ratio was used in order to better resolve the spectra with 633 nm excitation.

For a single AuNP the luminescence follows the scattering spectrum and shows a weak polarization dependence. The AuNPs are not perfect spheres and interact with light differently depending on their orientation relative to the incident light polarization as was observed previously for scattering.[2,40] Figure 5.10A compares the scattering and the luminescence spectrum excited at 514 nm for the same AuNP that was also imaged by correlated SEM. The luminescence spectra vary with the detected polarization angle, as shown in the inset of Figure 5.10A. This anisotropy is also noticeable in the correlation spectroscopy measurements, causing a deviation from the expected translational behavior of a samples containing only a single species, as seen in Figure 5.3A. To determine

whether the observed spectra could be due to scattering we compared luminescence spectra for AuNRs excited at different wavelengths.

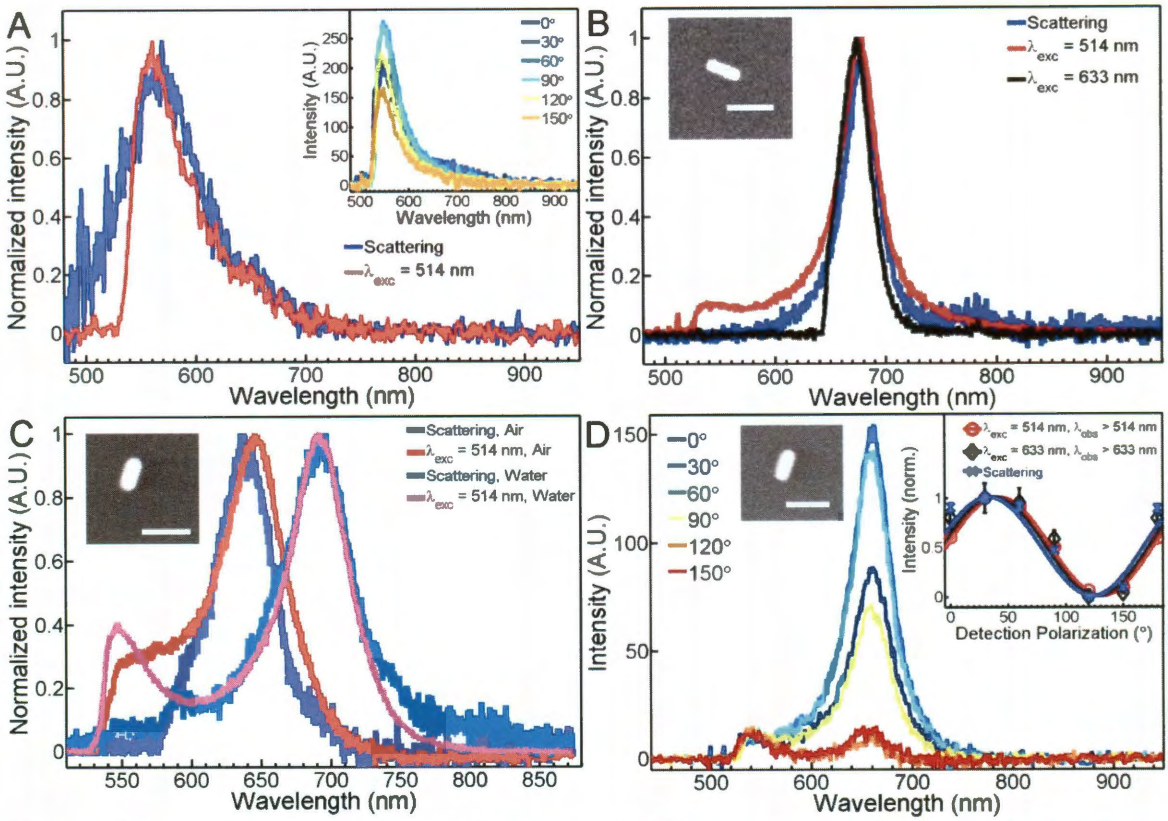

Figure 5.10. (A): Scattering (blue) and 514 nm excited luminescence (red) spectra of a AuNP. The inset shows polarized spectra that change in amplitude as the detection polarization is varied. (B): Unpolarized scattering (blue) and luminescence spectra excited at 514 nm (red) and 633 nm (black) of a 27x75 nm AuNR shown in the inset. (C): Unpolarized scattering (blue and cyan) and 514 nm excited luminescence (red and magenta) spectra of a 33x70 nm AuNR shown in the SEM image, which was immobilized on a glass coverslip and surrounded by air and water, respectively. (D): Polarized luminescence spectra with 514 nm excitation of a 34x68 nm AuNR shown in the SEM image. The inset illustrates the intensity as a function of detected polarization obtained by integrating the area under the spectra for the corresponding entire spectral ranges and then normalized to the maximum value, for luminescence excited at 514 nm (red) and 633 nm (black) as well as for scattering (blue). The error bars were computed from at least 3 spectra that were acquired for each polarization. The excitation light is unpolarized and circularly polarized for the scattering and luminescence spectra, respectively. All scale bars correspond to 100 nm.

The luminescence spectra of the AuNRs are independent of the excitation wavelength. For the single AuNR, shown in the SEM image in the inset of Figure 5.10B, unpolarized spectra of scattering, 514 nm, and 633 nm excited luminescence are

displayed in the main part of Figure 5.10B. The three spectra are almost indistinguishable from each other for the longitudinal plasmon resonance. Thus we can conclude that these spectra excited at a single laser wavelength are due to luminescence and not elastic scattering and also that luminescence can be excited both at the transverse (514 nm) or the longitudinal (633 nm) plasmon resonance giving nearly identical responses that spectrally overlap with the long wavelength plasmon band. The luminescence spectrum when excited at 514 nm also has a peak near 520 nm that coincides with the transverse plasmon resonance, which is visible in the bulk extinction spectrum, but too weak to be seen in the single particle scattering spectra.[39] The exact location of this short wavelength peak cannot be determined because of the dichroic filter that was used.

The luminescence spectrum shifts with a change of the dielectric constant of the surrounding medium in the same way as the scattering spectrum does. Figure 5.10C shows single particle scattering (blue and cyan) and 514 nm excited luminescence (red and magenta) spectra for a 33x70 nm AuNR supported on glass taken in air and water, respectively. The effective refractive index changes from 1.25 as in the case of the spectra taken in air, to 1.4 for the spectra taken with water on top of the sample. The shift in the resonance maximum is about 50 nm for both scattering and luminescence. The transverse plasmon resonance did not shift measurably, but is resolved better in the luminescence spectrum with the added water because the shoulder of the longitudinal resonance no longer overlaps significantly. These results suggest that the observed luminescence is caused by emission of a plasmon. This mechanism can be probed in

more detail by studying the polarization dependence of the luminescence excited at 514 and 633 nm.

The polarized luminescence spectra of a single 34x68 nm AuNR in Figure 5.10D and its inset show a strong polarization dependence for the longitudinal mode which modulates in phase with the scattering signal. In contrast, the short wavelength peak is only weakly polarization dependent. To calculate the modulation depth of the scattering and luminescence intensity as a function of the detection polarization, we recorded spectra for 10 different AuNRs as a function of polarizer angle and integrated the entire area under the spectra for each of them. An example for scattering and luminescence of the same AuNR is shown in the inset of Figure 5.10D. The resulting polarization traces were fit to $I(\theta) = N(1 + M \cos 2(\theta - \varphi))$, where N is a normalization factor, M is the modulation depth, θ is the polarizer angle, and φ represents the angle of the longest projected dipole axis with respect to a reference frame.[172] Scattering exhibits a perfect dipole behavior with an average modulation depth of 0.95±0.05 obtained from 10 individual AuNRs. Luminescence for 633 nm excitation closely follows amplitude and phase of scattering and its modulation depth is 0.94±0.05. The integrated luminescence for 514 nm excitation has a slightly lower modulation depth of 0.90±0.07 because the short wavelength peak does not change in amplitude for different detection polarizations.

These results support the conclusion that the model used in Equation 5.5 fails to correctly describe the experimental autocorrelation curves for 514 nm excitation because the luminescence polarization anisotropy is close to that of a perfect dipole, whereas the amplitude of the rotational component suggests an anisotropy that is much lower. Besides the emission dipole, the absorption dipole also affects the amplitude of the

rotational component and we can probe it by recording spectra as a function of the excitation polarization.

We found that the longitudinal plasmon luminescence is independent of the excitation polarization at 514 nm and always occurs along the long axis of the AuNR. This was achieved by independently controlling the polarization angles of both excitation and detection as shown in Figure 5.11A. When the excitation is set parallel to the short axis of the AuNR and the detected polarization is parallel to the long AuNR axis the highest intensity is obtained (90°-0°, cyan). No changes are observed when the excitation polarization is rotated by 90° (0°-0°, green). On the other hand, rotating the emission polarizer by 90° erases the longitudinal peak independent of the excitation polarization. Therefore we can conclude that luminescence of the AuNR is always aligned parallel to the long axis, regardless of the excitation polarization. The independence of the excitation polarization is further illustrated in the inset of Figure 5.11A, where the unpolarized integrated luminescence intensity is plotted as a function of excitation polarization yielding an almost negligible modulation depth.

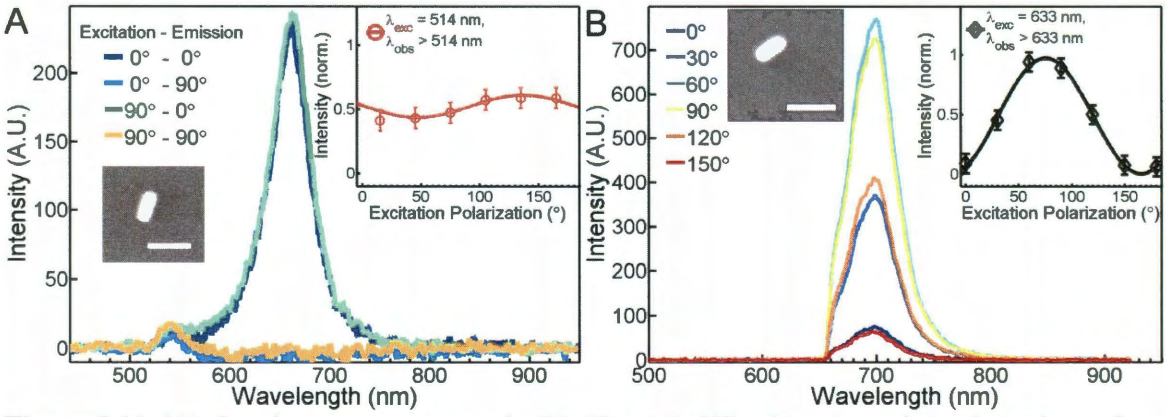

Figure 5.11. (A): Luminescence spectra of a 34x68 nm AuNR taken at varying orientations of excitation and detection polarizations relative to the long axis of the AuNR. The integrated intensity as a function of excitation polarization is given in the inset. For this data the detection polarizer was removed. (B): Unpolarized luminescence spectra of a 35x72 nm AuNR shown in the SEM image excited at 633 nm for different excitation polarizations. The integrated intensity as a function of excitation polarization is shown in the inset. All scale bars correspond to 100 nm.

Excitation at 633 nm on the other hand exhibits the expected dipole behavior and matches the phase of the luminescence. Therefore absorption and emission dipoles are collinear for 633 nm excitation. Unpolarized luminescence spectra of a 35x72 nm AuNR for different excitation polarizations are shown in Figure 5.11B. Plotting the integrated area under the spectra versus the excitation polarization yields the curve shown in the inset of Figure 5.11B and a modulation depth of 0.97 confirming a perfect dipole behavior.

We assign the luminescence to the radiative decay of surface plasmons.[64,67] Figure 5.12 shows a suggested mechanism for one-photon plasmon emission of AuNRs. Luminescence occurs from both the transverse and longitudinal surface plasmon resonances with the latter being the dominant decay channel. This model is supported by the nearly perfect spectral overlap of the luminescence with scattering in both air and water environments and the high polarization dependence of the longitudinal surface plasmon emission.

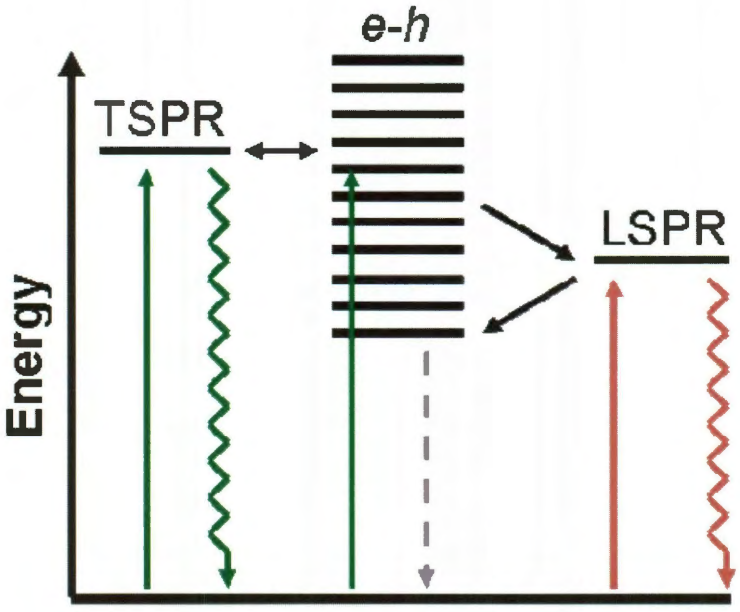

Figure 5.12. Schematic diagram of the mechanism for one-photon plasmon luminescence of AuNRs. The solid green lines represent excitation with 514 nm laser light, which excites both d-sp interband transitions creating electron-hole (e-h) pairs and the transverse surface plasmon resonance (TSPR). The solid red line depicts excitation of the longitudinal surface plasmon resonance (LSPR) with 633 nm laser light. The wavy green and red lines represent emission from the TSPR and LSPR, respectively. Nonradiative relaxation occurs through recombination of e-h pairs as indicated by the dashed gray line.

The observation that the emission of the AuNPs also follows the plasmon resonance validates the assignment of the short wavelength peak in the AuNR luminescence spectrum to emission of the transverse plasmon. At 514 nm, both d-sp interband transitions and the transverse surface plasmon are excited due to their spectral overlap. Interband absorption creates electron-hole pairs that can relax very efficiently through nonradiative pathways because of the large density of states in the conduction (sp) and valence (d) bands. However, analyzing the excitation and emission polarizations of the short wavelength peak in the AuNR luminescence spectra revealed a significant depolarization of the emission compared to previous polarization sensitive photothermal imaging of the absorption at 514 nm.[172] This loss of polarization is assigned to a fast

interconversion between electron-hole pairs and the transverse surface plasmon resonance that subsequently decays radiatively. Because of the limited spectral range for the transverse mode due to the dichroic used, other luminescence mechanisms like plasmon amplified electron-hole pair recombination can at the moment not be ruled out completely for this wavelength range.

The importance of hot electron-hole pairs and the fast interconversion between them and surface plasmons becomes even more evident when considering the longitudinal surface plasmon resonance. Direct excitation at 633 nm is highly polarized parallel to the long AuNR axis for both absorption and emission and leads to either direct plasmon emission or nonradiative decay through the generation of electron-hole pairs. However, excitation at 514 nm also gives rise to mainly longitudinal surface plasmon emission, which does not depend on the excitation polarization. Because the transverse and longitudinal modes are orthogonal to each other, this observation can only be rationalized if hot electron-hole pairs can also create surface plasmons again. The decay of surface plasmons into electron-hole pairs is a well accepted energy relaxation channel,[169] but our results also show that the opposite is possible, although most likely with a much smaller yield.

Estimating a detection efficiency of 5-10% for our microscope setup, we determined the quantum yields of one-photon plasmon emission for different excitation wavelengths.[202] Using calculated absorption cross sections of 1.44×10^3 nm^2 and 1.87×10^3 nm^2 at 514 and 633 nm for a 24x76 nm AuNR, and respective incident laser powers of 37.5 μw and 1.5 μw measured at the sample, luminescence quantum yields of about 8×10^{-6} and 3×10^{-4} are obtained for 514 and 633 nm excitation, respectively. Those values

agree well with previous reports of quantum yields for small AuNPs – 10^{-6};[67] and AuNRs – 10^{-4}.[68] Luminescence excited at the longitudinal surface plasmon resonance is significantly more efficient, which can be explained by the fact that the longitudinal surface plasmon energy is below the threshold for interband absorptions. Nonradiative recombination of electrons with holes in the valence band is hence no longer possible giving rise to longer lifetimes.[169] Most of the energy is, however, dissipated via nonradiative recombination of electron-hole pairs as shown by the gray line in Figure 5.12.

5.5 Conclusions

We have shown that one-photon luminescence can be used to track AuNPs and AuNRs in solution and recover correct sizes using correlation spectroscopy. To the best of our knowledge rotational dynamics of AuNRs in water was for the first time studied via scattering and luminescence at two different wavelengths – 514 and 633 nm – and proved to be a valuable tool in determining the size of the AuNRs. We observed that luminescence correlation spectroscopy is less sensitive to aggregation than scattering correlation spectroscopy and as such can be used for environments that trigger aggregation of NPs (e.g. high ionic strength). We further determined that 633 nm excitation is better suited to study diffusion of AuNRs, because the absorption and emission dipoles are collinear, which improves the amplitude of the rotational component and as such makes it more precise. Absorption and emission dipoles for luminescence excited at 514 nm are not collinear, which needs to be accounted for in the theoretical equations that model the auto- and crosscorrelation functions.

This interpretation of the luminescence correlation spectroscopy results was only possible by recording single particle luminescence spectra using polarization sensitive excitation and detection. We found that one-photon luminescence of AuNPs and AuNRs closely follows the scattering spectrum and changes in the refractive index of the medium affect the scattering and luminescence spectra in the same way. Regardless of the excitation wavelength and polarization, the major intensity of the luminescence always occurs polarized along the long axis of the AuNRs through emission of longitudinal plasmons, which can only be explained by fast interconversion between hot electron-hole pairs and surface plasmons. Especially for 514 nm excitation, transverse surface plasmons and interband absorption create hot electron-hole pairs that subsequently decay into longitudinal plasmons causing an apparent depolarization of the absorption dipole moment. For correlation spectroscopy, excitation directly into the longitudinal plasmon is therefore more effective and explains the agreement between theoretical and experimental curves for 633 nm excitation, as well as why the theory fails for 514 nm excited luminescence. The luminescence results have, however, bigger implications because they clearly show for the first time plasmon emission in AuNRs and furthermore reveal the important interplay between hot electron-hole pairs and surface plasmons, which could be exploited for plasmon assisted NP surface photochemistry.

5.5 Acknowledgements

This work was supported by the Nanoscale Science and Engineering Initiative of the National Science Foundation under NSF Award Numbers EEC-0647452 and CHE-0955286, the Robert A. Welch Foundation (Grant C-1664), the ACS Petroleum Research

Fund (50191-DNI6), and a 3M Nontenured Faculty Grant. I also thank the following individuals for their help and providing insight and productive conversation with respect to this work: Sergio Dominguez-Medina, Dr. Wei-Shun Chang, Pattanawit Swanglap, Liane S. Slaughter, Saumyakanti Khatua, Dr. Carmen Reznik and Dr. Christy Landes.

CHAPTER 6

CONCLUSIONS

Practical applications of NPs elicit many critical questions, one of which is how the NPs behave in the medium where they are proposed to be used. FCS provides a powerful tool to study the diffusion of NPs in different media and recover changes occurring to the hydrodynamic radii of NPs in real-time. This thesis described the steps taken to adapting a well known single molecule technique – FCS – to work with NP samples, which are much larger than a single molecule. Furthermore, sample heterogeneity, which is inevitable for NP samples, introduces signal heterogeneity that is significantly larger than for single molecules. It was found that acquisition parameters in FCS have a profound effect on the recovered particle size if certain criteria are not met. For example, the length of the autocorrelation transient has to be at least 5000 times longer than the characteristic diffusion time. As previously mentioned, NP samples can never be perfectly homogeneous. Moreover, even in instances when traditional bulk analysis methods like TEM or SEM confirm low size heterogeneity of NP cores, a low percentage of aggregates present in the solution can skew correlation spectroscopy measurements. A method to detect whether the results of FCS are affected by the aggregates was developed and tested on dye labeled magnetite nanocrystals.

Labeling of NPs is a very common technique for visualizing NPs, although the presence of unbound dye molecules and photophysics of the dye can complicate the analysis using FCS. Using a stable intrinsic signal of the analyte avoids those issues and a part of this work was dedicated to characterizing absorption and scattering of single

AuNPs, and relating size heterogeneity to signal heterogeneity. It was found that in addition to variation due to particle size, varying the orientation of the particle relative to the incident light results in very different signal intensity even for supposedly spherical AuNP, which can shows up as a rotational component in the autocorrelation analysis when using polarized light excitation and detection. Scattering and absorption of an AuNP is greatly enhanced at the plasmon resonance, making the AuNP stand out from the background. However, in biomedical applications, the background for absorption and scattering is likely to be very strong because of the highly crowded environment. Using the luminescence signal could help alleviate this problem, because scattered light from the background can be blocked.

One-photon luminescence from AuNPs and AuNRs was characterized and studied with single particle spectroscopy and found to be strong enough to be used for correlation spectroscopy measurements. Several sizes of AuNRs and AuNPs were analyzed for translational and rotational dynamics employing the one-photon luminescence, and the correct sizes were recovered. It was shown that correlation spectroscopy can be effectively used with "real-life" samples that were not specially prepared via purification or labeling. In the future, I envision correlation spectroscopy to be used to study changes occurring to the coating of NPs and their coagulation upon entering a biological environment, among other vital questions for practical applications of NPs.

APPENDIX A
MOST COMMONLY USED PROGRAMS THAT WERE WRITTEN AND USED IN THE COURSE OF THIS WORK

1. Intensity correlation spectroscopy

1.1. autocorrelation

compute_autocorrelation_AT_MMDDYY.m
The program calculates autocorrelation function from raw BH files. Modifications by date differ in small details that were needed for a particular analysis

Most important versions:

compute_autocorrelation_AT_021710.m	your working horse for the FCS, calculates AC, bins it up and saves an ASCI file with it. Plain, simple, trusted.
compute_autocorrelation_AT_042610.m	background, which has to be calculated prior to that, is subtracted before autocorrelation is computed

Calls

load_binary_pms_batch.m	reads in binary files from BH board
Logbindata.m	bins autocorrelated data logarithmically
ac_fitting_XXX.m	fits autocorrelated data with the desired function (name reflects the type of function)

Requires
- Filenames and paths to the files to be analyzed
- Number of files to be concatenated for autocorrelation (can take lists of variables)
- Channels to be used (can take lists of variables)

1.2. cross-correlation

compute_Xcorrelation_AT_030710.m
The program calculates cross-correlation function from raw BH files. Modifications by date differ in small details that were needed for a particular analysis

Most important versions:

compute_Xcorrelation_AT_030710.m	channel A is cross-correlated with B
compute_Xcorrelation_AT_030710_chBA.m	channel B is cross-correlated with A

Calls

load_binary_pms_batch.m	reads in binary files from BH board
Logbindata.m	bins autocorrelated data logarithmically

ac_fitting_XXX.m	fits autocorrelated data with the desired function (name reflects the type of function)

Requires
- Filenames and paths to the files to be analyzed
- Number of files to be concatenated for autocorrelation (can take lists of variables)
- Channels to be used (can take lists of variables)

1.3. binning up transients

binup_transients_AT_061208.m
Reads in the raw BH data and produces a binned up transient of specified bin time

Calls
load_binary_pms_batch – read in binary files from BH board

Requires
- Filenames and paths to the files to be analyzed
- New bin time values (can take lists of variables)
- Number of files to be concatenated for autocorrelation (can take lists of variables)
- Channels to be used (can take lists of variables)

1.4. find and analyze events in transients

should be done running the following programs
1) Bin up the transients. *binup_transients_AT_061208.*
2) Analyze transients for events that exceed a given threshold and histogram events for each transient. *blip_analysis_in_binnedup_transients.m.*
3) Analyze the histograms, following an example as here (just an example, the only thing it does is combining the specific histograms and plotting them as a figure) *compare_intensity_distributions_50_90_AuNP_FL_052310.m*

blip_analysis_in_binnedup_transients.m
Requires
- Filenames and paths
- Analysis parameters

1.5. NI board files

1.5.1. autocorrelation

compute_autocorrelation_NI_board_AT_081010.m

Calculates the autocorrelation function from NI board files and saves log binned values as an ASCI file

Calls

logbindata.m	bins autocorrelated data logarithmically

Requires
- Filenames and paths to the files to be analyzed

1.5.2. binning up

binup_transients_NI_board_AT_081010.m
Reads in raw NI board files and bins them up to the specified new bin value.

Requires
- Filenames and paths to the files to be analyzed
- New bin time values (can take lists of variables)

1.6. Simulations

simulate_diffusion_3D_2env_AT_111308.m
The program simulates diffusion of particles in a given volume, producing a signal transient that is recorded from a focal volume of adjustable dimensions. The volume can be arbitrarily split into two regions with different values of viscosity. Particles can be all of the same size or there could be two separate species. The focal volume dimensions can be adjusted. Shot noise can be added to the signal given off by the particles. Autocorrelation functions are calculated mimicking the experimental transients, which are of the predefined length, and the analysis is done the same way allowing direct comparison between simulated and experimental data. The program is written in Matlab and uses random walk for diffusion approximation.

Calls

logbindata.m	bins autocorrelated data logarithmically
ac_fitting_3D_fig.m	Fitting function
ac_fitting_3D_2env_060908.m	Fitting function
ac_fitting_with_Zz_fig.m	Fitting function

Requires
- Path where to save the output
- Parameters for the simulations: dimensions of the box and focal volume, length of the trajectory, number of particles, etc. By default all values are set up so that a sample simulation will run to completion

2. Image processing

2.1. Line_Section_GUI_v3

line_section_GUI_v3.m

This is a program with graphical interface to view and process raster-images created by microscopes up- and downstairs. It lets the user to rescale image intensities as well as measure line sections at arbitrary positions, selected with mouse clicks. It can also do particle intensity analysis in manual and automatic mode. The former requires user to click on all particles of interest, the latter automatically locates the particles on the image. The automated algorithm is quite capable of working with images that have multiple aggregates by employing cutoffs for intensity, minimum and maximum particle sizes as well as watershed algorithm for separating particles that are close to each other.

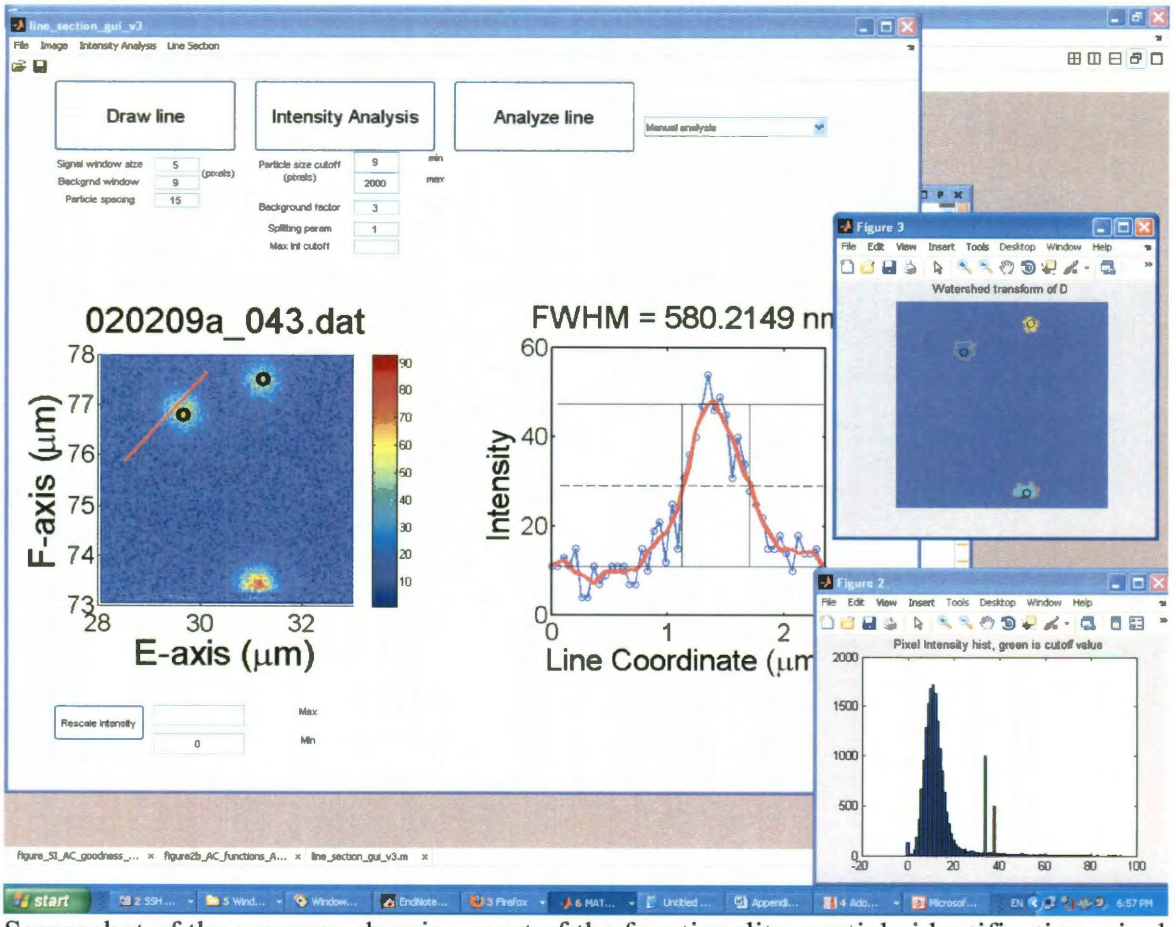

Screenshot of the program showing most of the functionality: particle identification, pixel intensity histogram and line section analysis.

Calls

All files that are necessary for the program are located in the same directory.

line_section_gui_v3.m	Main program
compute_background.m	Calculates image background
draw_rectangle_interactively.m	Tool to draw in the figure
find_particles_on_image_v3.m	Finds particles on the image
fnFindNP_AT.m	A subroutine within find_particles…
freehanddraw.m	Drawing tool
hTransposeMenuitemCallback.m	Manipulates the image
iconRead.m	Default Matlab's function to display icons
intensityShift_bk_AT.m	Part of calculating the intensity of particles
linept.m	Part of the drawing tool
makelist.m	Makes list of variables
pca_AT_v1.m	Calculates PCA on the array of points
plot_HWHM_AT_020309.m	Controls line sectioning panel
plot_image.m	Function for plotting specific file formats
plot_image_XPMPro.m	Function for plotting specific file formats
plot_image_XPMPro_ASCI.m	Function for plotting specific file formats
ReadImage_XMPro.m	Reads XMPro files (2006 format)
ReadImage_XMPro_new.m	Reads XMPro files (2008 format)

Requires
- Input file has to be either from David's labview program (downstaits lab) or XMPro (upstairs lab)

2.2. SEM image analysis

2.2.1. Manual measuring

measure_stuff_manually.m
Works with any image format. Loads and displays the image on the screen. Calculates the distance between consequent mouse clicks, plots them on the image and stores the values with coordinates in a file. If a scale bar is available, then the user has the option of measuring it and converting the values from pixels to nanometers.

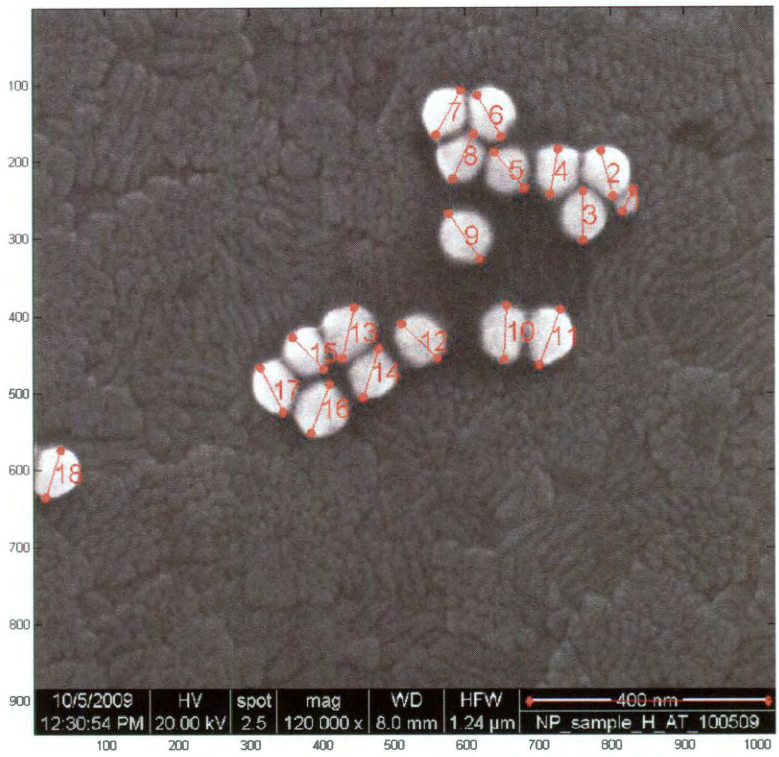

Screenshot after particle measurements. Each measurement's value is stored along with the index number shown here on the image.

Calls
Got everything it needs inside

2.2.2. Automated processing

find_particles_SEM_multi_one_day_AT.m
Measures particles in multiple SEM images from the same day. Uses watershed algorithm to locate the particles, and the user has the flexibility of setting cutoff for max and min size of a particle, splitting parameter (tendency to combine or separate spots that are close to each other) and contrast. The sizes are measured as the first two principal axes of the particle indentified via watersheding. The program has been adapted and modified by Liane and she now has the latest version of it.

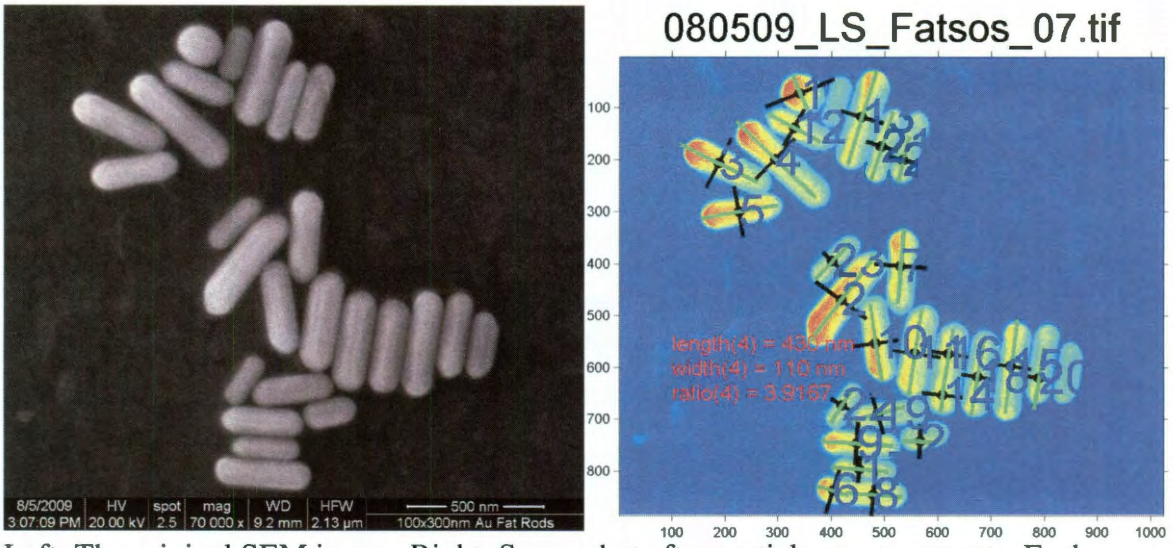

Left: The original SEM image. Right: Screenshot after particle measurements. Each measurement's value is stored along with the index number shown here on the image.

Calls

SEMmag_JOEL.m	Converts magnification to nm/pixel
fn_find_particles_on_SEM_JOEL_AT.m	Finds the particles on the image from JOEL 2010 SEM
fn_find_particles_on_SEM_image.m	Finds the particles on the image from the other SEM

Requires

- All files to be analyzed share the same mask (e.g., '051110_Sergio_25x86nm')
- Magnification for each image (can be entered as an array)

BIBLIOGRAPHY

1. Wohland, T.; Rigler, R.; Vogel, H. The Standart Deviation in Fluorescence Correlation Spectroscopy. *Biophysical Journal* **2001,** 80, 2987-2999.

2. Tcherniak, A.; Ha, J. W.; Dominguez-Medina, S.; Slaughter, L. S.; Link, S. Probing a Century Old Prediction One Plasmonic Particle at a Time. *Nano Letters* **2010,** 10, (4), 1398-1404.

3. Whitesides, G. M. The 'right' size in nanobiotechnology. *Nature Biotechnology* **2003,** 21, 1161-1165.

4. Alivisatos, A. P. Semiconductor Clusters, Nanocrystals, and Quantum Dots. *Science* **1996,** 271, (5251), 933-937.

5. Henderson, J., *The science and archaeology of materials: an investigation of inorganic materials*. Routledge: 2000.

6. Bohren, C. F.; Huffman, D. R., *Absorption and Scattering of Light by Small Particles*. Wiley: New York, 1983.

7. Averitt, R. D.; Sarkar, D.; Halas, N. J. Plasmon resonance shifts of Au-coated Au2S nanoshells: Insight into multicomponent nanoparticle growth. *Physical Review Letters* **1997,** 78, (22), 4217-4220.

8. Link, S.; El-Sayed, M. A. Spectral properties and relaxation dynamics of surface plasmon electronic oscillations in gold and silver nanodots and nanorods. *Journal of Physical Chemistry B* **1999,** 103, (40), 8410-8426.

9. Halas, N. J. Plasmonics: An Emerging Field Fostered by Nano Letters. *Nano Letters* **2010,** 10, (10), 3816-3822.

10. Yavuz, C. T.; Mayo, J. T.; Yu, W. W.; Prakash, A.; Falkner, J. C.; Yean, S.; Cong, L.; Shipley, H. J.; Kan, A.; Tomson, M.; Natelson, D.; Colvin, V. L. Low-Field Magnetic Separation of Monodisperse Fe3O4 Nanocrystals. *Science* **2006,** 314, 964-967.

11. Ekimov, A. I.; Efros, A. L.; Onushchenko, A. A. Quantum Size Effect in Semiconductor Microcrystals. *Solid State Communications* **1985,** 56, (11), 921-924.

12. Licata, N. A.; Tkachenko, A. V. Self-assembling DNA-caged particles: Nanoblocks for hierarchical self-assembly. *Physical Review E* **2009,** 79, (1).

13. Nehl, C. L.; Liao, H. W.; Hafner, J. H. Optical properties of star-shaped gold nanoparticles. *Nano Letters* **2006,** 6, (4), 683-688.

14. Colvin, V. L. The potential environmental impact of engineered nanomaterials. *Nature Biotechnology* **2003,** 21, (10), 1166-1170.

15. Yu, W. W.; Chang, E.; Falkner, J. C.; Zhang, J.; Al-Somali, A. M.; Sayes, C. M.; Johns, J.; Drezek, R.; Colvin, V. L. Forming Biocompatible and Nonaggregated Nanocrystals in Water Using Amphiphilic Polymers. *Journal of the American Chemical Society* **2007,** 129, (10), 2871-2879.

16. Palazzo, B.; Iafisco, M.; Laforgia, M.; Margiotta, N.; Natile, G.; Bianchi, C. L.; Walsh, D.; Mann, S.; Roveri, N. Biomimetic hydroxyapatite-drug nanocrystals as potential bone substitutes with antitumor drug delivery properties. *Advanced Functional Materials* **2007,** 17, 2180-2188.

17. Moghimi, S. M.; Kissel, T. Particulate nanomedicines. *Advanced Drug Delivery Reviews* **2006,** 58, (14), 1451-1455.

18. Lowery, A. R.; Gobin, A. M.; Day, E. S.; Halas, N. J.; West, J. L. Immunonanoshells for targeted photothermal ablation of tumor cells. *International Journal of Nanomedicine* **2006,** 1, (2), 149-154.

19. Hall, J. B.; Dobrovolskaia, M. A.; Patri, A. K.; McNeil, S. E. Characterization of nanoparticles for therapeutics. *Nanomedicine (London, United Kingdom)* **2007,** 2, (6), 789-803.

20. Wang, Q. B.; Xu, Y.; Zhao, X. H.; Chang, Y.; Liu, Y.; Jiang, L. J.; Sharma, J.; Seo, D. K.; Yan, H. A facile one-step in situ functionalization of quantum dots with preserved photoluminescence for bioconjugation. *Journal of the American Chemical Society* **2007,** 129, (20), 6380-+.

21. Charvet, N.; Reiss, P.; Roget, A.; Dupuis, A.; Grunwald, D.; Carayon, S.; Chandezon, F.; Livache, T. Biotinylated CdSe/ZnSe nanocrystals for specific fluorescent labeling. *Journal of Materials Chemistry* **2004,** 14, (17), 2638-2642.

22. Querner, C.; Reiss, P.; Bleuse, J.; Pron, A. Chelating Ligands for nanocrystals' surface functionalization. *Journal of the American Chemical Society* **2004,** 126, (37), 11574-11582.

23. Loo, C.; Lowery, A.; Halas, N.; West, J.; Drezek, R. Immunotargeted nanoshells for integrated cancer imaging and therapy. *Nano Letters* **2005,** 5, (4), 709-711.

24. Jain, P. K.; El-Sayed, I. H.; El-Sayed, M. A. Au nanoparticles target cancer. *Nano Today* **2007,** 2, (1), 18-29.

25. Jain, P. K.; Huang, X.; El-Sayed, I. H.; El-Sayed, M. A. Noble metals on the nanoscale: optical and photothermal properties and some applications in imaging, sensing, biology, and medicine. *Accounts of Chemical Research* **2008,** 41, (12), 1578-86.

26. Chen, S.; Li, Y.; Guo, C.; Wang, J.; Ma, J.; Liang, X.; Yang, L.-R.; Liu, H.-Z. Temperature-Responsive Magnetite/PEO-PPO-PEO Block Copolymer Nanoparticles for Controlled Drug Targeting Delivery. *Langmuir* **2007,** 23, (25), 12669-12676.

27. Tcherniak, A.; Prakash, A.; Mayo, J. T.; Colvin, V. L.; Link, S. Fluorescence Correlation Spectroscopy of Magnetite Nanocrystal Diffusion. *The Journal of Physical Chemistry C* **2009,** 113, (3), 844-848.

28. Klokkenburg, M.; Erne, B. H.; Wiedenmann, A.; Petukhov, A. V.; Philipse, A. P. Dipolar structures in magnetite ferrofluids studied with small-angle neutron scattering with and without applied magnetic field. *Physical Review E: Statistical, Nonlinear, and Soft Matter Physics* **2007,** 75, (5-1), 051408/1-051408/9.

29. McFarland, A. D.; Van Duyne, R. P. Single Silver Nanoparticles as Real-Time Optical Sensors with Zeptomole Sensitivity. *Nano Letters* **2003,** 3, 1057-1062.

30. Raschke, G.; Kowarik, S.; Franzl, T.; Sonnichsen, C.; Klar, T. A.; Feldmann, J.; Nichtl, A.; Kurzinger, K. Biomolecular recognition based on single gold nanoparticle light scattering. *Nano Letters* **2003,** 3, (7), 935-938.

31. Bianco, A.; Kostarelos, K.; Prato, M. Applications of carbon nanotubes in drug delivery. *Current Opinion in Chemical Biology* **2005,** 9, (6), 674-679.

32. Nahar, M.; Dutta, T.; Murugesan, S.; Asthana, A.; Mishra, D.; Rajkumar, V.; Tare, M.; Saraf, S.; Jain, N. K. Functional polymeric nanoparticles: An efficient and promising tool for active delivery of bioactives. *Critical Reviews in Therapeutic Drug Carrier Systems* **2006,** 23, (4), 259-318.

33. Hung, W. H.; Aykol, M.; Valley, D.; Hou, W.; Cronin, S. B. Plasmon Resonant Enhancement of Carbon Monoxide Catalysis. *Nano Letters* **2010,** 10, (4), 1314-1318.

34. Valden, M.; Lai, X.; Goodman, D. W. Onset of catalytic activity of gold clusters on titania with the appearance of nonmetallic properties *Science* **1998,** 281, 1647.

35. Mayer, K. M.; Hao, F.; Lee, S.; Nordlander, P.; Hafner, J. H. A single molecule immunoassay by localized surface plasmon resonance. *Nanotechnology* **2010,** 21, (25), 255503.

36. Lynch, I.; Salvati, A.; Dawson, K. A. Protein-Nanoparticle Interactions: What does the cell see? *Nature Nanotechnology* **2009,** 4, (9), 546-547.

37. Knight, M. W.; Wu, Y. P.; Lassiter, J. B.; Nordlander, P.; Halas, N. J. Substrates Matter: Influence of an Adjacent Dielectric on an Individual Plasmonic Nanoparticle. *Nano Letters* **2009,** 9, (5), 2188-2192.

38. Nehl, C. L.; Grady, N. K.; Goodrich, G. P.; Tam, F.; Halas, N. J.; Hafner, J. H. Scattering spectra of single gold nanoshells. *Nano Letters* **2004,** 4, (12), 2355-2359.

39. Slaughter, L. S.; Chang, W.-S.; Swanglap, P.; Tcherniak, A.; Khanal, B. P.; Zubarev, E. R.; Link, S. Single-Particle Spectroscopy of Gold Nanorods beyond the Quasi-Static Limit: Varying the Width at Constant Aspect Ratio. *The Journal of Physical Chemistry C* **2010,** 114, (11), 4934-4938.

40. Cang, H.; Montiel, D.; Xu, C. S.; Yang, H. Observation of spectral anisotropy of gold nanoparticles. *The Journal of Chemical Physics* **2008,** 129, (4), 044503-5.

41. Abate, Y.; Schwartzberg, A.; Strasser, D.; Leone, S. R. Nanometer-scale size dependent imaging of cetyl trimethyl ammonium bromide (CTAB) capped and uncapped gold nanoparticles by apertureless near-field optical microscopy. *Chemical Physics Letters* **2009,** 474, (1-3), 146-152.

42. Kim, D.-S.; Heo, J.; Ahn, S.-H.; Han, S. W.; Yun, W. S.; Kim, Z. H. Real-Space Mapping of the Strongly Coupled Plasmons of Nanoparticle Dimers. *Nano Letters* **2009,** 9, (10), 3619-3625.

43. Slaughter, L. S.; Wu, Y.; Willingham, B. A.; Nordlander, P.; Link, S. Effects of Symmetry Breaking and Conductive Contact on the Plasmon Coupling in Gold Nanorod Dimers. *ACS Nano* **2010,** 4, (8), 4657-4666.

44. Biesheuvel, P. M. Ionizable polyelectrolyte brushes: brush height and electrosteric interaction. *Journal of Colloid and Interface Science* **2004,** 275, (1), 97-106.

45. Limpoco, F. T.; Advincula, R. C.; Perry, S. S. Solvent dependent friction force response of polystyrene brushes prepared by surface initiated polymerization. *Langmuir* **2007,** 23, (24), 12196-12201.

46. Reznik, C.; Estillore, N.; Advincula, R. C.; Landes, C. F. Single Molecule Spectroscopy Reveals Heterogeneous Transport Mechanisms for Molecular Ions in a Polyelectrolyte Polymer Brush. *Journal of Physical Chemistry B* **2009,** 113, (44), 14611-14618.

47. Cang, H.; Wong, C. M.; Xu, C. S.; Rizvi, A. H.; Yang, H. Confocal three dimensional tracking of a single nanoparticle with concurrent spectroscopic readouts. *Applied Physics Letters* **2006,** 88, (22), 3.

48. Tsyboulski, D. A.; Bachilo, S. M.; Kolomeisky, A. B.; Weisman, R. B. Translational and Rotational Dynamics of Individual Single-Walled Carbon Nanotubes in Aqueous Suspension. *ACS Nano* **2008,** 2, (9), 1770-1776.

49. Rigler, R.; Mets, U.; Widengren, J.; Kask, P. Fluorescence correlation spectroscopy with high count rate and low background: Analysis of translational diffusion. *Eur. Biophys. J.* **1993,** 22, (3), 169-75.

50. Quarta, A.; Di Corato, R.; Manna, L.; Argentiere, S.; Cingolani, R.; Barbarella, G.; Pellegrino, T. Multifunctional Nanostructures Based on Inorganic Nanoparticles and Oligothiophenes and Their Exploitation for Cellular Studies. *Journal of the American Chemical Society* **2008,** 130, (32), 10545-10555.

51. Lee, H.; Yu, M. K.; Park, S.; Moon, S.; Min, J. J.; Jeong, Y. Y.; Kang, H. W.; Jon, S. Thermally cross-linked superparamagnetic iron oxide nanoparticles: Synthesis and application as a dual Imaging probe for cancer in vivo. *Journal of the American Chemical Society* **2007,** 129, (42), 12739-12745.

52. Nguyen, T. T.; Swift, J. L.; Burger, M. C.; Cramb, D. T. Effects of Various Small-Molecule Anesthetics on Vesicle Fusion: A Study Using Two-Photon Fluorescence Cross-Correlation Spectroscopy. *Journal of Physical Chemistry B* **2009,** 113, (30), 10357-10366.

53. Seydack, M. Nanoparticle labels in immunosensing using optical detection methods. *Biosensors & Bioelectronics* **2005,** 20, (12), 2454-2469.

54. Chen, Y.; Lu, Z. Dye sensitized luminescent europium nanoparticles and its time-resolved fluorometric assay for DNA. *Analytica Chimica Acta* **2007,** 587, (2), 180-186.

55. Cho, E.-B.; Volkov, D. O.; Sokolov, I. Ultrabright Fluorescent Mesoporous Silica Nanoparticles. *Small* **2010,** 6, (20), 2314-2319.

56. Bohmer, M.; Enderlein, J. Fluorescence spectroscopy of single molecules under ambient conditions: methodology and technology. *ChemPhysChem* **2003,** 4, (8), 793-808.

57. Enderlein, J.; Gregor, I.; Patra, D.; Fitter, J. Art and artefacts of fluorescence correlation spectroscopy. *Curr. Pharm. Biotechnol.* **2004,** 5, (2), 155-61.

58. Davis, L. M.; Shen, G. Q. Accounting for triplet and saturation effects in FCS measurements. *Current Pharmaceutical Biotechnology* **2006,** 7, (4), 287-301.

59. Boyer, D.; Tamarat, P.; Maali, A.; Lounis, B.; Orrit, M. Photothermal imaging of nanometer-sized metal particles among scatterers. *Science* **2002,** 297, (5584), 1160-1163.

60. Kuyper, C. L.; Budzinski, K. L.; Lorenz, R. M.; Chiu, D. T. Real-Time Sizing of Nanoparticles in Microfluidic Channels Using Confocal Correlation Spectroscopy. *Journal of the American Chemical Society* **2006,** 128, (3), 730-731.

61. Tsay, J. M.; Doose, S.; Weiss, S. Rotational and translational diffusion of peptide-coated CdSe/CdS/ZnS nanorods studied by fluorescence correlation spectroscopy. *Journal of the American Chemical Society* **2006,** 128, (5), 1639-1647.

62. Wang, H. F.; Huff, T. B.; Zweifel, D. A.; He, W.; Low, P. S.; Wei, A.; Cheng, J. X. In vitro and in vivo two-photon luminescence imaging of single gold nanorods. *Proceedings of the National Academy of Sciences of the United States of America* **2005,** 102, (44), 15752-15756.

63. Loumaigne, M.; Richard, A.; Laverdant, J.; Nutarelli, D.; Debarre, A. Ligand-Induced Anisotropy of the Two-Photon Luminescence of Spherical Gold Particles in Solution Unraveled at the Single Particle Level. *Nano Letters* **2010,** 10, (8), 2817-2824.

64. Bouhelier, A.; Bachelot, R.; Lerondel, G.; Kostcheev, S.; Royer, P.; Wiederrecht, G. P. Surface Plasmon Characteristics of Tunable Photoluminescence in Single Gold Nanorods. *Physical Review Letters* **2005,** 95, (26), 267405.

65. Wilcoxon, J. P.; Martin, J. E.; Parsapour, F.; Wiedenman, B.; Kelley, D. F. Photoluminescence from nanosize gold clusters. *Journal of Chemical Physics* **1998,** 108, (21), 9137-9143.

66. Boyd, G. T.; Yu, Z. H.; Shen, Y. R. Photoinduced luminescence from the noble metals and its enhancement on roughened surfaces. *Physical Review B* **1986,** 33, (12), 7923-7936.

67. Dulkeith, E.; Niedereichholz, T.; Klar, T. A.; Feldmann, J.; von Plessen, G.; Gittins, D. I.; Mayya, K. S.; Caruso, F. Plasmon emission in photoexcited gold nanoparticles. *Physical Review B* **2004,** 70, (20), 205424.

68. Mohamed, M. B.; Volkov, V.; Link, S.; El-Sayed, M. A. The 'lightning' gold nanorods: fluorescence enhancement of over a million compared to the gold metal. *Chemical Physics Letters* **2000,** 317, (6), 517-523.

69. Chen, J. J.; Irudayaraj, J. Quantitative Investigation of Compartmentalized Dynamics of ErbB2 Targeting Gold Nanorods in Live Cells by Single Molecule Spectroscopy. *Acs Nano* **2009,** 3, (12), 4071-4079.

70. He, H.; Xie, C.; Ren, J. Nonbleaching fluorescence of gold nanoparticles and its applications in cancer cell imaging. *Analytical Chemistry* **2008,** 80, (15), 5951-5957.

71. Wu, X.; Ming, T.; Wang, X.; Wang, P.; Wang, J.; Chen, J. High-Photoluminescence-Yield Gold Nanocubes: For Cell Imaging and Photothermal Therapy. *ACS Nano* **2009,** 4, (1), 113-120.

72. Schwille, P. Fluorescence correlation spectroscopy and its potential for intracellular applications. *Cell Biochem. Biophys.* **2001,** 34, (3), 383-408.

73. Anderson, L. J. E.; Mayer, K. M.; Fraleigh, R. D.; Yang, Y.; Lee, S.; Hafner, J. H. Quantitative Measurements of Individual Gold Nanoparticle Scattering Cross Sections. *Journal of Physical Chemistry C* **2010,** 114, (25), 11127-11132.

74. Sabanayagam, C. R.; Lakowicz, J. R. Fluctuation correlation spectroscopy and photon histogram analysis of light scattered by gold nanospheres. *Nanotechnology* **2007,** 18, (35), 7.

75. Paulo, P. M. R.; Gaiduk, A.; Kulzer, F.; Krens, S. F. G.; Spaink, H. P.; Schmidt, T.; Orrit, M. Photothermal Correlation Spectroscopy of Gold Nanoparticles in Solutions *The Journal of Physical Chemistry C* **2009,** 113, (27), 11451-11457.

76. Octeau, V.; Cognet, L.; Duchesne, L.; Lasne, D.; Schaeffer, N.; Fernig, D. G.; Lounis, B. Photothermal Absorption Correlation Spectroscopy. *ACS Nano* **2009,** 3, (2), 345-350.

77. Magde, D.; Webb, W. W.; Elson, E. Thermodynamic Fluctuations in a Reacting System - Measurement by Fluorescent Correlation Spectroscopy. *Physical Review Letters* **1972,** 29, (11), 705.

78. Magde, D.; Elson, E. L.; Webb, W. W. Fluorescence Correlation Spectroscopy. II. An Experimental Realization. *Biopolymers* **1974,** 13, 29-61.

79. Elson, E. L.; Madge, D. Fluorescence correlation spectroscopy I. Conceptual basis and theory. *Biopolymers* **1974,** 13, 1-27.

80. Aragon, S.; Pecora, R. Fluorescence correlation spectroscopy as a probe of molecular dynamics. *J. Chem. Phys.* **1976,** 64, (4), 1791.

81. Brinkmeier, M.; Dorre, K.; Stephan, J.; Eigen, M. Two beam cross correlation: A method to characterize transport phenomena in micrometer-sized structures. *Analytical Chemistry* **1999,** 71, (3), 609-616.

82. Schwille, P.; Bieschke, J.; Oehlenschlager, F. Kinetic investigations by fluorescence correlation spectroscopy: The analytical and diagnostic potential of diffusion studies. *Biophysical Chemistry* **1997,** 66, (2-3), 211-228.

83. Tcherniak, A.; Reznik, C.; Link, S.; Landes, C. F. Fluorescence Correlation Spectroscopy: Criteria for Analysis in Complex Systems. *Analytical Chemistry* **2009,** 81, (2), 746-754.

84. Dauty, E.; Verkman, A. S. Molecular crowding reduces to a similar extent the diffusion of small solutes and macromolecules: measurement by fluorescence correlation spectroscopy. *J. Mol. Recognit.* **2004,** 17, 441-447.

85. Adkins, E. M.; Samuvel, D. J.; Fog, J. U.; Eriksen, J.; Jayanthi, L. D.; Bjerggaard Vaegter, C.; Ramamoorthy, S.; Gether, U. Membrane Mobility and Microdomain Association of the Dopamine Transporter Studied with Fluorescence Correlation Spectroscopy and Fluorescence Recovery after Photobleaching. *Biochemistry* **2007,** 46, (37), 10484-10497.

86. Benda, A.; Benes, M.; Marecek, V.; Lhotsky, A.; Hermens, W. T.; Hof, M. How to determine diffusion coefficients in planar phospholipid systems by confocal fluorescence correlation spectroscopy. *Langmuir* **2003,** 19, (10), 4120-4126.

87. Posokhov, Y. O.; Rodnin, M. V.; Lu, L.; Ladokhin, A. S. Membrane Insertion Pathway of Annexin B12: Thermodynamic and Kinetic Characterization by Fluorescence Correlation Spectroscopy and Fluorescence Quenching. *Biochemistry* **2008,** 47, (18), 5078-5087.

88. Braenden, M.; Sanden, T.; Brzezinski, P.; Widengren, J. Localized proton microcircuits at the biological membrane-water interface. *Proc. Natl. Acad. Sci. U.S.A.* **2006,** 103, (52), 19766-19770.

89. Gennerich, A.; Schild, D. Aniosotropic diffusion in mitral cell dendrites revealed by fluorescence correlation spectroscopy. *Biophys. J.* **2002,** 83, 510-522.

90. Gosch, M.; Blom, H.; Holm, J.; Heino, T.; Rigler, R. Hydrodynamic flow profiling in microchannel structures by single molecule fluorescence correlation spectroscopy. *Anal. Chem.* **2000,** 72, 3260-3265.

91. Foquet, M.; Korlach, J.; Zipfel, W. R.; Webb, W. W.; Craighead, H. G. Focal volume confinement by submicrometer-sized fluidic channels. *Anal. Chem.* **2004,** 76, 1618-1626.

92. Grabowski, C. A.; Mukhopadhyay, A. Comparing the activation energy of diffusion in bulk and ultrathin fluid films. *J. Chem. Phys.* **2007,** 127, (17), 171101/1-171101/4.

93. Schuster, J.; Cichos, F.; Wrachtrup, J.; Von Borczyskowski, C. Diffusion of single molecules close to interfaces. *Single Mol.* **2000,** 1, (4), 299-305.

94. Reznik, C.; Darugar, Q.; Wheat, A.; Fulghum, T.; Advincula, R. C.; Landes, C. Single ion diffusive transport within a poly(styrene sulfonate) polymer brush matrix probed by fluorescence correlation spectroscopy. *J. Phys. Chem. B* **2008,** 112, (35), 10890-10897.

95. Wang, W.; Zhang, C.; Wang, S.; Zhao, J. Diffusion of single polyelectrolytes on the surface of poly(N-isopropylacrylamide) brushes. *Macromolecules* **2007,** 40, 9564-9569.

96. Hosokawa, C.; Yoshikawa, H.; Masuhara, H. Cluster formation of nanoparticles in an optical trap studied by fluorescence correlation spectroscopy. *Phys. Rev. E.* **2005,** 72, (2-1), 021408/1-021408/7.

97. Liedl, T.; Keller, S.; Simmel, F. C.; Raedler, J. O.; Parak, W. J. Fluorescent nanocrystals as colloidal probes in complex fluids measured by fluorescence correlation spectroscopy. *Small* **2005,** 1, (10), 997-1003.

98. Rochira, J. A.; Gudheti, M. V.; Gould, T. J.; Laughlin, R. R.; Nadeau, J. L.; Hess, S. T. Fluorescence intermittency limits brightness in CdSe/ZnS nanoparticles quantified by fluorescence correlation spectroscopy. *J. Phys. Chem. C.* **2007,** 111, (4), 1695-1708.

99. Enderlein, J.; Gregor, I.; Patra, D.; Dertinger, T.; Kaupp, U. B. Performance of fluorescence correlation spectroscopy for measuring diffusion and concentration. *ChemPhysChem* **2005,** 6, (11), 2324-36.

100. Hess, S. T.; Webb, W. W. Focal volume optics and experimental artifacts in confocal fluorescence correlation spectroscopy. *Biophysical Journal* **2002,** 83, (4), 2300-2317.

101. Haustein, E.; Schwille, P. Ultrasensitive investigations of biological systems by fluorescence correlation spectroscopy. *Methods* **2003,** 29, (2), 153-166.

102. Haustein, E.; Schwille, P. Fluorescence correlation spectroscopy: novel variations of an established technique. *Annu. Rev. Biophys. Biomol.* **2007,** 36, 151-169.

103. Wohland, T.; Rigler, R.; Vogel, H. The standard deviation in fluorescence correlation spectroscopy. *Biophys. J.* **2001,** 80, (6), 2987-99.

104. Meseth, U.; Wohland, T.; Rigler, R.; Vogel, H. Resolution of fluorescence correlation measurements. *Biophys. J.* **1999,** 76, 1619-1631.

105. Gell, C.; Brockwell, D. J.; Beddard, G. S.; Radford, S. E.; Kalverda, A. P.; Smith, D. A. Accurate use of single molecule fluorescence correlation spectroscopy to determine molecular diffusion times. *Single Mol.* **2001,** 2, (3), 177-181.

106. Wei, C.-Y. J.; Lu, C.-Y.; Kim Yeon, H.; Vanden Bout David, A. Determining if a system is heterogeneous: The analysis of single molecule rotational correlation functions and their limitations. *J. Fluoresc.* **2007,** 17, (6), 797-804.

107. Lu, C.-Y.; Vanden Bout, D. Effect of finite trajectory length on the correlation function analysis of single molecule data. *J. Chem. Phys.* **2006,** 125, 124701.

108. Nie, S.; Chiu, D. T.; Zare, R. N. Real-time detection of single molecules in solution by confocal fluorescence microscopy. *Anal. Chem.* **1995,** 67, (17), 2849-57.

109. Culbertson, M. J.; Williams, J. T. B.; Cheng, W. W. L.; Stults, D. A.; Wiebracht, E. R.; Kasianowicz, J. J.; Burden, D. L. Numerical fluorescence correlation spectroscopy for the analysis of molecular dynamics under nonstandard conditions. *Anal. Chem.* **2007,** 79, (11), 4031-4039.

110. Magatti, D.; Ferri, F. Fast multi-tau real-time software correlator for dynamic light scattering. *Appl. Opt.* **2001,** 40, (24), 4011-4021.

111. Wahl, M.; Gregor, I.; Patting, M.; Enderlein, J. Fast calculation of fluroescence correlation data with asynchronous time-correlated single-photon counting. *Opt. Express* **2003,** 11, (26), 3583-3591.

112. Eigen, M.; Rigler, R. Sorting single molecules: application to diagnostics and evolutionary biotechnology. *Proc. Natl. Acad. Sci. U.S.A.* **1994,** 91, (13), 5740-7.

113. Funke, S. A.; Birkmann, E.; Henke, F.; Goertz, P.; Lange-Asschenfeldt, C.; Riesner, D.; Willbold, D. Single particle detection of Ab aggregates associated with Alzheimer's disease. *Biochem. Biophys. Res. Commun.* **2007,** 364, (4), 902-907.

114. Wirth, M.; Ludes, M.; Swinton, D. Analytic solution to the autocorrelation function for lateral diffusion and rare strong adsorption. *Appl. Spectrosc.* **2001,** 55, (6), 663-669.

115. Ries, J.; Schwille, P. Studying slow membrane dynamics with continuous wave scanning fluorescence correlation spectroscopy. *Biophys. J.* **2006,** 91, 1915-1924.

116. Hac, A. E.; Seeger, H.; Fidorra, M.; Heimburg, T. Diffusion in two-component lipd membranes - a fluorescence correlation spectroscopy and monte carlo simulation study. *Biophys. J.* **2005,** 88, 317-333.

117. Malengo, G.; Andolfo, A.; Sidenius, N.; Gratton, E.; Zamai, M.; Caiolfa, V. R. Fluorescence correlation spectroscopy and photon counting histogram on membrane proteins: functional dynamics of the glycosylphosphatidylinositol-anchored urokinase plasminogen activator receptor. *J. Biomed. Opt.* **2008,** 13, (3), 031215-1 - 031215-14.

118. Gilliland, J. W.; Yokoyama, K.; Yip, W. T. Effect of coulombic interactions on rotational mobility of guests in sol-gel silicate thin films. *Chem. Mater.* **2004,** 16, (20), 3949-3954.

119. Zondervan, R.; Kulzer, F.; Berkhout, G. C. G.; Orrit, M. Local viscosity of supercooled glycerol near Tg probed by rotational diffusion of ensembles and single dye molecules. *Proc. Natl. Acad. Sci. U.S.A.* **2007,** 104, (31), 12628-12633.

120. Forkey, J. N.; Quinlan, M. E.; Goldman, Y. E. Protein structural dynamics by single-molecule fluorescence polarization. *Prog. Biophys. Mol. Biol.* **2000,** 74, (1-2), 1-35.

121. Nam, J.-M.; Thaxton, C. S.; Mirkin, C. A. Nanoparticle-based bio-bar codes for the ultrasensitive detection of proteins. *Science* **2003,** 301, 1884.

122. Franzreb, M.; Siemann-Herzberg, M.; Hobley, T. J.; Thomas, O. R. T. Protein purification using magnetic adsorbent particles. *Applied Microbiology and Biotechnology* **2006,** 70, (5), 505-516.

123. Lewin, M.; Carlesso, N.; Tung, C.-H.; Tang, X.-W.; Cory, D.; Scadden, D. T.; Weissleder, R. Tat peptide-derivatized magnetic nanoparticles allow in vivo tracking and recovery of progenitor cells *Nature Biotechnology* **2000,** 18, 410.

124. Pankhurst, Q. A.; Connolly, J.; Jones, S. K.; Dobson, J. Applications of magnetic nanoparticles in biomedicine. *Journal of Physics D: Applied Physics* **2003,** 36, (13), R167-R181.

125. Wang, L.; Yang, Z.; Gao, J.; Xu, K.; Gu, H.; Zhang, B.; Zhang, X.; Xu, B. A Biocompatible Method of Decorporation: Bisphosphonate-Modified Magnetite Nanoparticles to Remove Uranyl Ions from Blood. *Journal of the American Chemical Society* **2006,** 128, (41), 13358-13359.

126. Gerber, R.; Takayasu, M.; Friedlaender, F. J. Generalization of HGMS theory: the capture of ultra-fine particles. *IEEE Transactions on Magnetics* **1983,** MAG-19, (5), 2115-17.

127. Cotten, G. B.; Eldredge, H. B. Nanolevel magnetic separation model considering flow limitations. *Separation Science and Technology* **2002,** 37, (16), 3755-3779.

128. Takayasu, M.; Gerber, R.; Friedlaender, F. J. Magnetic separation of submicron particles. *IEEE Transactions on Magnetics* **1983,** MAG-19, (5), 2112-14.

129. Moeser, G. D.; Roach, K. A.; Green, W. H.; Hatton, T. A.; Laibinis, P. E. High-gradient magnetic separation of coated magnetic nanoparticles. *AIChE Journal* **2004,** 50, (11), 2835-2848.

130. Klokkenburg, M.; Erne, B. H.; Meeldijk, J. D.; Wiedenmann, A.; Petukhov, A. V.; Dullens, R. P. A.; Philipse, A. P. In Situ Imaging of Field-Induced Hexagonal Columns in Magnetite Ferrofluids. *Physical Review Letters* **2006,** 97, (18), 185702/1-185702/4.

131. Klokkenburg, M.; Vonk, C.; Claesson, E. M.; Meeldijk, J. D.; Erne, B. H.; Philipse, A. P. Direct Imaging of Zero-Field Dipolar Structures in Colloidal Dispersions of Synthetic Magnetite. *Journal of the American Chemical Society* **2004,** 126, (51), 16706-16707.

132. Enderlein, J.; Gregor, I.; Patra, D.; Fitter, J. Statistical analysis of diffusion coefficient determination by fluorescence correlation spectroscopy. *Journal of Fluorescence* **2005,** 15, (3), 415-422.

133. Schwille, P.; Haupts, U.; Maiti, S.; Webb, W. W. Molecular dynamics in living cells observed by fluorescence correlation spectroscopy with one- and two-photon excitation. *Biophysical Journal* **1999,** 77, (4), 2251-2265.

134. Wu, B.; Muller, J. D. Time-integrated fluorescence cumulant analysis in fluorescence fluctuation spectroscopy. *Biophysical Journal* **2005,** 89, (4), 2721-2735.

135. Chen, Y.; Muller, J. D.; So, P. T. C.; Gratton, E. The photon counting histogram in fluorescence fluctuation spectroscopy. *Biophysical Journal* **1999,** 77, (1), 553-567.

136. Kask, P.; Palo, K.; Ullmann, D.; Gall, K. Fluorescence-intensity distribution analysis and its application in biomolecular detection technology. *Proceedings of the National Academy of Sciences of the United States of America* **1999,** 96, (24), 13756-13761.

137. Meng, F.; Ma, H. A Comparison between Photon Counting Histogram and Fluorescence Intensity Distribution Analysis. *Journal of Physical Chemistry B* **2006,** 110, (51), 25716-25720.

138. Palo, K.; Mets, U.; Jager, S.; Kask, P.; Gall, K. Fluorescence intensity multiple distributions analysis: concurrent determination of diffusion times and molecular brightness. *Biophysical Journal* **2000,** 79, (6), 2858-2866.

139. Muller Joachim, D. Cumulant analysis in fluorescence fluctuation spectroscopy. *Biophysical Journal* **2004,** 86, (6), 3981-92.

140. Yu, W. W.; Falkner, J. C.; Yavuz, C. T.; Colvin, V. L. Synthesis of monodisperse iron oxide nanocrystals by thermal decomposition of iron carboxylate salts. *Chemical Communications (Cambridge, United Kingdom)* **2004**, (20), 2306-2307.

141. Widengren, J.; Kudryavtsev, V.; Antonik, M.; Berger, S.; Gerken, M.; Seidel, C. A. M. Single-Molecule Detection and Identification of Multiple Species by Multiparameter Fluorescence Detection. *Analytical Chemistry* **2006,** 78, (6), 2039-2050.

142. Boehmer, M.; Enderlein, J. Fluorescence spectroscopy of single molecules under ambient conditions: Methodology and technology. *ChemPhysChem* **2003,** 4, (8), 792-808.

143. Peleg, G.; Ghanouni, P.; Kobilka, B. K.; Zare, R. N. Single-molecule spectroscopy of the β2 adrenergic receptor: Observations of conformational substates in a membrane protein. *Proceedings of the National Academy of Sciences* **2001,** 98, (15), 8469-8474.

144. Engheta, N. Circuits with Light at Nanoscales: Optical Nanocircuits Inspired by Metamaterials. *Science* **2007,** 317, (5845), 1698-1702.

145. Ozbay, E. Plasmonics: Merging Photonics and Electronics at Nanoscale Dimensions. *Science* **2006,** 311, (5758), 189-193.

146. Dionne, J. A.; Diest, K.; Sweatlock, L. A.; Atwater, H. A. PlasMOStor: A metal-oxide-Si field effect plasmonic modulator. *Nano Letters* **2009,** 9, 897-902.

147. Rosi, N. L.; Mirkin, C. A. Nanostructures in biodiagnostics. *Chemical Reviews* **2005,** 105, (4), 1547-1562.

148. Soennichsen, C.; Reinhard, B. M.; Liphardt, J.; Alivisatos, A. P. A molecular ruler based on plasmon coupling of single gold and silver nanoparticles. *Nature Biotechnology* **2005,** 23, (6), 741-745.

149. Schultz, S.; Smith, D. R.; Mock, J. J.; Schultz, D. A. Single-target molecule detection with nonbleaching multicolor optical immunolabels *Proceedings of the National Academy of Sciences of the United States of America* **2000,** 97, 996.

150. Yguerabide, J.; Yguerabide, E. E. Light-scattering submicroscopic particles as highly fluorescent analogs and their use as tracer labels in clinical and biological applications - I. Theory. *Analytical Biochemistry* **1998,** 262, (2), 137-156.

151. Lasne, D.; Blab, G. A.; Berciaud, S.; Heine, M.; Groc, L.; Choquet, D.; Cognet, L.; Lounis, B. Single nanoparticle photothermal tracking (SNaPT) of 5-nm gold beads in live cells. *Biophysical Journal* **2006,** 91, (12), 4598-4604.

152. Murphy, C. J.; Gole, A. M.; Stone, J. W.; Sisco, P. N.; Alkilany, A. M.; Goldsmith, E. C.; Baxter, S. C. Gold Nanoparticles in Biology: Beyond Toxicity to Cellular Imaging. *Accounts of Chemical Research* **2008,** 41, (12), 1721-1730.

153. O'Neal, D. P.; Hirsch, L. R.; Halas, N. J.; Payne, J. D.; West, J. L. Photo-thermal tumor ablation in mice using near infrared-absorbing nanoparticles. *Cancer Letters* **2004,** 209, (2), 171-176.

154. Huang, X. H.; El-Sayed, I. H.; Qian, W.; El-Sayed, M. A. Cancer cell imaging and photothermal therapy in the near-infrared region by using gold nanorods. *Journal of the American Chemical Society* **2006,** 128, (6), 2115-2120.

155. Kreibig, U.; Vollmer, M., *Optical Properties of Metal Clusters*. Springer: Berlin, 1995.

156. Barhoumi, A.; Huschka, R.; Bardhan, R.; Knight, M. W.; Halas, N. J. Light-induced release of DNA from plasmon-resonant nanoparticles: Towards light-controlled gene therapy. *Chemical Physics Letters* **2009,** 482, (4-6), 171-179.

157. Reismann, M.; Bretschneider, J., C. ; Plessen, G. v.; Simon, U. Reversible Photothermal Melting of DNA in DNA-Gold-Nanoparticle Networks. *Small* **2008,** 4, (5), 607-610.

158. Taton, T. A.; Lu, G.; Mirkin, C. A. Two-color labeling of oligonucleotide arrays via size-selective scattering of nanoparticle probes. *Journal of the American Chemical Society* **2001,** 123, (21), 5164-5165.

159. Khlebtsov, B.; Zharov, V.; Melnikov, A.; Tuchin, V.; Khlebtsov, N. Optical amplification of photothermal therapy with gold nanoparticles and nanoclusters. *Nanotechnology* **2006,** 17, (20), 5167-5179.

160. Jain, P. K.; Lee, K. S.; El-Sayed, I. H.; El-Sayed, M. A. Calculated absorption and scattering properties of gold nanoparticles of different size, shape, and composition: Applications in biological imaging and biomedicine. *Journal of Physical Chemistry B* **2006,** 110, (14), 7238-7248.

161. Mie, G. Articles on the optical characteristics of turbid media, especially colloidal metal solutions. *Annalen Der Physik* **1908,** 25, (3), 377-445.

162. van Dijk, M. A.; Tchebotareva, A. L.; Orrit, M.; Lippitz, M.; Berciaud, S.; Lasne, D.; Cognet, L.; Lounis, B. Absorption and scattering microscopy of single metal nanoparticles. *Physical Chemistry Chemical Physics* **2006,** 8, (30), 3486-3495.

163. Khlebtsov, N. G. Optics and biophotonics of nanoparticles with a plasmon resonance. *Quantum Electronics* **2008,** 38, (6), 504-529.

164. Bogatyrev, V. A.; Dykman, L. A.; Khlebtsov, B. N.; Khlebtsov, N. G. Measurement of mean size and evaluation of polydispersity of gold nanoparticles from spectra of optical absorption and scattering. *Optics and Spectroscopy (Translation of Optika i Spektroskopiya)* **2004,** 96, (1), 128-135.

165. Kreibig, U.; Schmitz, B.; Breuer, H. D. Separation of plasmon-polariton modes of small metal particles. *Physical Review B* **1987,** 36, (9), 5027.

166. Arbouet, A.; Christofilos, D.; Del Fatti, N.; Vallee, F.; Huntzinger, J. R.; Arnaud, L.; Billaud, P.; Broyer, M. Direct measurement of the single-metal-cluster optical absorption. *Physical Review Letters* **2004,** 93, (12).

167. Ignatovich, F. V.; Novotny, L. Real-time and background-free detection of nanoscale particles. *Physical Review Letters* **2006,** 96, (1), 4.

168. Berciaud, S.; Cognet, L.; Blab, G. A.; Lounis, B. Photothermal heterodyne imaging of individual nonfluorescent nanoclusters and nanocrystals. *Physical Review Letters* **2004,** 93, (25), 257402.

169. Sonnichsen, C.; Franzl, T.; Wilk, T.; von Plessen, G.; Feldmann, J.; Wilson, O.; Mulvaney, P. Drastic reduction of plasmon damping in gold nanorods. *Physical Review Letters* **2002,** 88, (7), 077402.

170. Mock, J. J.; Barbic, M.; Smith, D. R.; Schultz, D. A.; Schultz, S. Shape effects in plasmon resonance of individual colloidal silver nanoparticles. *Journal of Chemical Physics* **2002,** 116, 6755.

171. Lindfors, K.; Kalkbrenner, T.; Stoller, P.; Sandoghdar, V. Detection and Spectroscopy of Gold Nanoparticles Using Supercontinuum White Light Confocal Microscopy. *Physical Review Letters* **2004,** 93, (3), 037401.

172. Chang, W. S.; Ha, J. W.; Slaughter, L. S.; Link, S. Plasmonic nanorod absorbers as orientation sensors. *Proceedings of the National Academy of Sciences of the United States of America* **2010,** 107, (7), 2781-2786.

173. Berciaud, S.; Cognet, L.; Tamarat, P.; Lounis, B. Observation of intrinsic size effects in the optical response of individual gold nanoparticles. *Nano Letters* **2005,** 5, (3), 515-518.

174. Sherry, L. J.; Jin, R.; Mirkin, C. A.; Schatz, G. C.; VanDuyne, R. P. Localized Surface Plasmon Resonance Spectroscopy of Single Silver Triangular Nanoprisms. *Nano Letters* **2006,** 6, (9), 2060-2065.

175. Novo, C.; Gomez, D.; Perez-Juste, J.; Zhang, Z. Y.; Petrova, H.; Reismann, M.; Mulvaney, P.; Hartland, G. V. Contributions from radiation damping and surface scattering to the linewidth of the longitudinal plasmon band of gold nanorods: a single particle study. *Physical Chemistry Chemical Physics* **2006,** 8, (30), 3540-3546.

176. Munechika, K.; Smith, J. M.; Chen, Y.; Ginger, D. S. Plasmon Line Width of Single Silver Nanoprisms as a function of Particle Size and Plasmon Peak Position *Journal of Physical Chemistry C* **2007,** 111, 18906-18911.

177. Hu, M.; Chen, J.; Marquez, M.; Xia, Y.; Hartland, G. V. Correlated Rayleigh Scattering Spectroscopy and Scanning Electron Microscopy Studies of Au-Ag Bimetallic Nanoboxes and Nanocages. *Journal of Physical Chemistry C* **2007,** 111, (34), 12558-12565.

178. Sonnichsen, C.; Franzl, T.; Wilk, T.; von Plessen, G.; Feldmann, J. Plasmon resonances in large noble-metal clusters. *New Journal of Physics* **2002,** 4, 93.1-93.8.

179. Tchebotareva, A. L.; van Dijk, M. A.; Ruijgrok, P. V.; Fokkema, V.; Hesselberth, M. H. S.; Lippitz, M.; Orrit, M. Acoustic and optical modes of single dumbbells of gold nanoparticles. *ChemPhysChem* **2009,** 10, (1), 111-114.

180. Novo, C.; Funston, A. M.; Pastoriza-Santos, I.; Liz-Marzan, L. M.; Mulvaney, P. Influence of the medium refractive index on the optical properties of single gold triangular prisms on a substrate *Journal of Physical Chemistry C* **2008,** 112, 3-7.

181. Mock, J. J.; Hill, R. T.; Degiron, A.; Zauscher, S.; Chilkoti, A.; Smith, D. R. Distance-Dependent Plasmon Resonant Coupling between a Gold Nanoparticle and Gold Film. *Nano Letters* **2008,** 8, 2245.

182. Rodriguez-Fernandez, J.; Novo, C.; Myroshnychenko, V.; Funston, A. M.; Sanchez-Iglesias, A.; Pastoriza-Santos, I.; Perez-Juste, J.; de Abajo, F. J. G.; Liz-Marzan, L. M.; Mulvaney, P. Spectroscopy, Imaging, and Modeling of Individual Gold Decahedra. *Journal of Physical Chemistry C* **2009,** 113, (43), 18623-18631.

183. McMahon, J. M.; Wang, Y.; Sherry, L. J.; Van Duyne, R. P.; Marks, L. D.; Gray, S. K.; Schatz, G. C. Correlating the Structure, Optical Spectra, and Electrodynamics of Single Silver Nanocubes. *Journal of Physical Chemistry C* **2009,** 113, 2731–2735.

184. Jin, R.; Jureller, J. E.; Kim, H. Y.; Scherer, N. F. Correlating second harmonic optical responses of single Ag nanoparticles with morphology. *Journal of the American Chemical Society* **2005,** 127, 12482-12483.

185. Johnson, P. B.; Christy, R. W. Optical Constants of the Noble Metals. *Physical Review B* **1972,** 6, (12), 4370.

186. Draine, B. T.; Flatau, P. J. Discrete-dipole approximation for periodic targets: theory and tests. *Journal of the Optical Society of America A: Optics and Image Science* **2008,** 25, (11), 2693-2703.

187. Beversluis, M. R.; Bouhelier, A.; Novotny, L. Continuum generation from single gold nanostructures through near-field mediated intraband transitions. *Physical Review B* **2003,** 68, (11), 10.

188. Kudo, S.; Magariyama, Y.; Aizawa, S. I. Abrupt Changes in Flagellar Rotation Observed by Laser Dark-Field Microscopy. *Nature* **1990,** 346, (6285), 677-680.

189. Nishiyama, M.; Muto, E.; Inoue, Y.; Yanagida, T.; Higuchi, H. Substeps within the 8-nm step of the ATPase cycle of single kinesin molecules. *Nature Cell Biology* **2001,** 3, (4), 425-428.

190. Noda, N.; Kamimura, S. A new microscope optics for laser dark-field illumination applied to high precision two dimensional measurement of specimen displacement. *Review of Scientific Instruments* **2008,** 79, (2), 7.

191. Nan, X. L.; Sims, P. A.; Xie, X. S. Organelle tracking in a living cell with microsecond time resolution and nanometer spatial precision. *ChemPhysChem* **2008,** 9, (5), 707-712.

192. Link, S.; El-Sayed, M. A. Spectroscopic determination of the melting energy of a gold nanorod. *Journal of Chemical Physics* **2001,** 114, (5), 2362-2368.

193. Sherry, L. J.; Chang, S. H.; Schatz, G. C.; Van Duyne, R. P.; Wiley, B. J.; Xia, Y. N. Localized surface plasmon resonance spectroscopy of single silver nanocubes. *Nano Letters* **2005,** 5, (10), 2034-2038.

194. Hoevel, H.; Fritz, S.; Hilger, A.; Kreibig, U.; Vollmer, M. Width of cluster plasmon resonance: Bulk dielectric functions and chemical interface damping. *Physical Review B* **1993,** 48, 18178-18188.

195. Hasan, W.; Lee, J.; Henzie, J.; Odom, T. W. Selective functionalization and spectral identification of gold nanopyramids *Journal of Physical Chemistry C* **2007,** 111, 17176.

196. Hirsch, L. R.; Stafford, R. J.; Bankson, J. A.; Sershen, S. R.; Rivera, B.; Price, R. E.; Hazle, J. D.; Halas, N. J.; West, J. L. Nanoshell-mediated near-infrared thermal therapy of tumors under magnetic resonance guidance. *Proceedings of the National Academy of Sciences of the United States of America* **2003,** 100, (23), 13549-13554.

197. Kang, B.; Mackey, M. A.; El-Sayed, M. A. Nuclear Targeting of Gold Nanoparticles in Cancer Cells Induces DNA Damage, Causing Cytokinesis Arrest and Apoptosis. *Journal of the American Chemical Society* **2010,** 132, (5), 1517-+.

198. Pinaud, F.; King, D.; Moore, H. P.; Weiss, S. Bioactivation and cell targeting of semiconductor CdSe/ZnS nanocrystals with phytochelatin-related peptides. *Journal of the American Chemical Society* **2004,** 126, (19), 6115-6123.

199. Deutsch, B.; Beams, R.; Novotny, L. Nanoparticle detection using dual-phase interferometry. *Applied Optics* **2010,** 49, (26), 4921-4925.

200. Eck, W.; Craig, G.; Sigdel, A.; Ritter, G.; Old, L. J.; Tang, L.; Brennan, M. F.; Allen, P. J.; Mason, M. D. PEGylated Gold Nanoparticles Conjugated to Monoclonal F19 Antibodies as Targeted Labeling Agents for Human Pancreatic Carcinoma Tissue. *Acs Nano* **2008,** 2, (11), 2263-2272.

201. Clancy, A. A.; Gregoriou, Y.; Yaehne, K.; Cramb, D. T. Measuring properties of nanoparticles in embryonic blood vessels: Towards a physicochemical basis for nanotoxicity. *Chemical Physics Letters* **2010,** 488, (4-6), 99-111.

202. Gaiduk, A.; Ruijgrok, P. V.; Yorulmaz, M.; Orrit, M. Making gold nanoparticles fluorescent for simultaneous absorption and fluorescence detection on the single particle level. *Physical Chemistry Chemical Physics* **2011,** 13, (1), 149-153.

203. Bingham, J. M.; Willets, K. A.; Shah, N. C.; Andrews, D. Q.; Van Duyne, R. P. Localized Surface Plasmon Resonance Imaging: Simultaneous Single Nanoparticle Spectroscopy and Diffusional Dynamics. *Journal of Physical Chemistry C* **2009,** 113, (39), 16839-16842.

204. Wang, G. F.; Sun, W.; Luo, Y.; Fang, N. Resolving Rotational Motions of Nano-objects in Engineered Environments and Live Cells with Gold Nanorods and Differential Interference Contrast Microscopy. *Journal of the American Chemical Society* **2010,** 132, (46), 16417-16422.

205. Aragon, S. R.; Pecora, R. Fluorescence correlation spectroscopy as a probe of molecular dymanics. *Journal of Chemical Physics* **1976,** 64, (4), 1791-1803.

206. Haustein, E.; Schwille, P. Single-molecule spectroscopic methods. *Current Opinion in Structural Biology* **2004,** 14, (5), 531-540.

207. Kim, S. A.; Heinze, K. G.; Schwille, P. Fluorescence correlation spectroscopy in living cells. *Nature Methods* **2007,** 4, (11), 963-973.

208. Tirado, M. M.; Martinez, C. L.; de la Torre, J. G. Comparison of theories for the translational and rotational diffusion coefficients of rod-like macromolecules. Application to short DNA fragments. *The Journal of Chemical Physics* **1984,** 81, (4), 2047-2052.

209. Sonnichsen, C.; Alivisatos, A. P. Gold Nanorods as Novel Nonbleaching Plasmon-Based Orientation Sensors for Polarized Single-Particle Microscopy. *Nano Letters* **2005,** 5, (2), 301-304.

210. Spetzler, D.; York, J.; Daniel, D.; Fromme, R.; Lowry, D.; Frasch, W. Microsecond Time Scale Rotation Measurements of Single F1-ATPase Moleculesâ€ *Biochemistry* **2006,** 45, (10), 3117-3124.

211. Pierrat, S.; Hartinger, E.; Faiss, S.; Janshoff, A.; Soì^nnichsen, C. Rotational Dynamics of Laterally Frozen Nanoparticles Specifically Attached to Biomembranes. *The Journal of Physical Chemistry C* **2009,** 113, (26), 11179-11183.

212. Varnavski, O. P.; Goodson, T.; Mohamed, M. B.; El-Sayed, M. A. Femtosecond excitation dynamics in gold nanospheres and nanorods. *Physical Review B* **2005,** 72, (23), 9.

213. Berland, K. M.; So, P. T. C.; Gratton, E. Two-photon fluorescence correlation spectroscopy: method and application to the intracellular environment *Biophysical Journal* **1995,** 68, (2), 694-701.

214. Daniels, C. R.; Reznik, C.; Landes, C. F. Dye Diffusion at Surfaces: Charge Matters. *Langmuir* **2010,** 26, (7), 4807-4812.

215. Einstein, A. The motion of elements suspended in static liquids as claimed in the molecular kinetic theory of heat. *Annalen Der Physik* **1905,** 17, (8), 549-560.

216. Kask, P.; Piksarv, P.; Pooga, M.; Mets, U.; Lippmaa, E. Separation of the rotational contribution in fluorescence correlation experiments. *Biophysical Journal* **1989,** 55, (2), 213-220.

217. Wei, C.-Y. J.; Kim, Y. H.; Darst, R. K.; Rossky, P. J.; Vanden Bout, D. A. Origins of Nonexponential Decay in Single Molecule Measurements of Rotational Dynamics. *Physical Review Letters* **2005,** 95, (17), 173001.

218. Yang, H. Single-Particle Light Scattering: Imaging and Dynamical Fluctuations in the Polarization and Spectral Response. *The Journal of Physical Chemistry A* **2007,** 111, (23), 4987-4997.

219. Miller, M. M.; Lazarides, A. A. Sensitivity of metal nanoparticle surface plasmon resonance to the dielectric environment. *Journal of Physical Chemistry B* **2005,** 109, (46), 21556-21565.

220. Haustein, E.; Schwille, P. Trends in fluorescence imaging and related techniques to unravel biological information. *HFSP Journal* **2007,** 1, (3), 169-180.

221. Wang, K. L.; Qiu, X.; Dong, C. Q.; Ren, J. C. Single-molecule technology for rapid detection of DNA hybridization based on resonance light scattering of gold nanoparticles. *Chembiochem* **2007,** 8, (10), 1126-1129.

222. Gans, R. Uber die Form ultramikroskopischer Goldteilchen. *Ann. Phys.* **1912,** 342, 881–900.

223. Del Fatti, N.; Christofilos, D.; Vallee, F. Optical response of a single gold nanoparticle. *Gold Bulletin* **2008,** 41, (2), 147-158.

224. Muskens, O. L.; Bachelier, G.; Del Fatti, N.; Vallee, F.; Brioude, A.; Jiang, X. C.; Pileni, M. P. Quantitative absorption spectroscopy of a single gold nanorod. *Journal of Physical Chemistry C* **2008,** 112, (24), 8917-8921.

225. Lakowicz, J. R., *Principles of Fluorescence Spectroscopy.* 3rd ed.; Springer: New York, 2006.

226. Imura, K.; Nagahara, T.; Okamoto, H. Near-Field Two-Photon-Induced Photoluminescence from Single Gold Nanorods and Imaging of Plasmon Modes. *The Journal of Physical Chemistry B* **2005,** 109, (27), 13214-13220.